Experimental investigation of potential topological and *p*-wave superconductors

Trần Văn Bảy

Experimental investigation of potential topological and *p*-wave superconductors

ACADEMISCH PROEFSCHRIFT

ter verkrijging van de graad van doctor
aan de Universiteit van Amsterdam
op gezag van de Rector Magnificus
prof. dr. D. C. van den Boom
ten overstaan van een door het college voor promoties
ingestelde commissie, in het openbaar te verdedigen
in de Agnietenkapel
op dinsdag 09 september 2014, te 14:00 uur.

door

Tran Van Bay

geboren te Binh Dinh, Vietnam

Promotiecommissie

Promotor:	Prof. dr. M. S. Golden
Co-promotor:	Dr. A. de Visser
Overige Leden:	Prof. dr. J. T. M. Walraven
	Prof. dr. C. J. M. Schoutens
	Prof. dr. C. Felser
	Dr. A. McCollam

Faculteit der Natuurwetenschappen, Wiskunde en Informatica

The research reported in this PhD dissertation was carried out at the Van der Waals-Zeeman Institute for Experimental Physics, University of Amsterdam. The work was partly financed by the Ministry of Education and Training (MOET), Vietnam. It was also part of the research program of the Stichting voor Fundamenteel Onderzoek der Materie (FOM), which is financially supported by the Nederlandse Organisatie voor Wetenschappelijk Onderzoek (NWO).

ISBN: 978-94-6259-285-8

Printed in the Netherlands by Ipskamp Drukkers B.V.

Cover: The TiNiSi structure of UCoGe (main object, chapter 6), the reduced upper critical field $B_{c2}(T)$ (front face, chapters 4 and 5), the *T*-*r* phase diagram (top face, chapter 3) and the magnetoresistance $\rho(B)$ (right face, chapter 6).

An electronic version of this dissertation can be downloaded from
`http://www.science.uva.nl/research/cmp/devisser/index.html`

"Seek and ye shall find. Unsought goes undetected."

(Sophocles)

"Use your smile to change the world; don't let the world change your smile."

(Anonymous)

To my parents,

My sisters and brothers,

My nieces and nephews.

Contents

Abbreviations

SCs	superconductors
BCS	Bardeen-Cooper-Schrieffer
FMSCs	ferromagnetic superconductors
FM QCP	ferromagnetic quantum critical point
QHE	quantum Hall effect
TIs	topological insulators
TSCs	topological superconductors
μSR	muon spin relaxation/rotation
QPTs	quantum phase transitions
IQHE	integer quantum Hall effect
SOC	spin orbit coupling
TRS	time reversal symmetry
TRI	time reversal invariant
TRB	time reversal breaking
WHH	Werthamer-Helfand-Hohenberg
ESP	equal spin pairing
ZBCPs	zero bias conduction peaks
ZF	zero field

Chapter 1 Introduction

1.1 General introduction

Superconductivity discovered by the Dutch physicist Heike Kamerlingh Onnes in Leiden in 1911 has provided one of the most fascinating research fields [1]. Not only is it a very special state of matter compared to the well-known states, conducting, semiconducting and insulating, but also the understanding of this novel ground state in some materials systems appears to be a great theoretical challenge. As regards its understanding, the microscopic theory which explains superconductivity in most materials was proposed by Bardeen, Cooper and Schrieffer (BCS) in 1957, and is based on the attractive rather than repulsive effective interaction between two electrons with anti-parallel spins of a Cooper pair via lattice vibrations [2]. However, more and more materials have been discovered which cannot be explained by BCS theory, the so-called unconventional superconductors (SCs). Unconventional superconductivity has been found in numerous systems over the last forty years, *e.g.* the prime example ^{3}He [3,4], later on heavy fermion compounds (see for instance [5–13]), cuprates [14,15] and iron pnictides [16,17].

Frequently, superconductivity emerges in the paramagnetic phase of a metal as a consequence of phonon-mediated pairing. Therefore, the coexistence of ferromagnetism and superconductivity in the same material, which is a so-called ferromagnetic superconductor (FMSC), has become a mesmerizing research field. The first example discovered in 2000 is UGe_2 [10]. Later, three other uranium-based FMSCs were found: URhGe [11], UIr [18] and UCoGe [19]. The emergence of this robust class of superconducting compounds requires novel theoretical insights rather than the standard BCS formalism. Theoretical predictions of *p*-wave SC in itinerant ferromagnets [20] were made long before the first FMSC was experimentally realized. In these first models, the exchange of longitudinal spin fluctuations near the ferromagnetic quantum critical point (FM QCP) was proposed as the pairing mechanism for triplet Cooper pairs. However, this simple model lacks an explanation for the non-zero superconducting transition temperature T_c at the QCP in UCoGe. Later on, more sophisticated theoretical models based on spin fluctuation approaches have appeared [21–24]. In these models, superconductivity and ferromagnetism coexist on the microscopic scale. Superconductivity is closely related to a magnetic instability near the FM QCP, and the same electrons are responsible for band ferromagnetism and superconductivity [25].

In addition, theoretical predictions followed by the experimental realization have very recently led to a completely new research field: topological insulators (TIs) [26,27]. These novel materials have a close connection to the quantum Hall effect (QHE), one of the central discoveries in the field of condensed matter physics in the 1980s. In the QHE, electrons that

are confined to two dimensions and are subjected to a strong magnetic field, exhibit a special, topological, type of order. A few years ago, it was realized that topological order can emerge quite generally in specific two and three dimensional materials. These materials are now called TIs [26,27]. Not only do TIs possess intriguing properties, which require novel insights and physics, but also these new materials have sparked wide research interest, because they offer new playgrounds for the realization of novel states of quantum matter [28,29]. In 3D TIs the bulk is insulating, but the 2D surface states - protected by a nontrivial Z_2 topology - are conducting. Most interestingly, the concept of TIs can also be applied to superconductors (SCs), due to the direct analogy between topological band theory and superconductivity: the Bogoliubov-de Gennes Hamiltonian for the quasiparticles of a SC has a close similarity to the Hamiltonian of a band insulator, where the SC gap corresponds to the gap of the band insulator [30,31]. Consequently, this analogy leads to another novel concept in condensed matter physics which is the so-called topological superconductor (TSC). Topological superconductivity can be adopted as a state that consists of a full superconducting gap in the bulk, but is topological and protected by symmetries at the boundaries of the system. The remarkable point is that the topological surface states can presumably harbor Majorana states. A Majorana zero mode is a particle that is identical to its own antiparticle. Majorana zero mode states are expected to be a key element for future topological quantum computation schemes. Experimentally, the most well known candidate for TSC is superfluid ^{3}He (phase B) [32–34] described by the topological invariant $\mathbb{Z}$. Yet another promising test case for 2D chiral superconductivity is the triplet superconductor Sr_2RuO_4 [35], but experimental evidence remains under debate, for instance, as regards the existence of the gapless surface states [29]. Other promising candidate topological superconductors can be found among the doped 3D TI $Cu_xBi_2Se_3$ (chapter 4) [36,37], the half-Heusler platinum bismuthide families with 111 stoichiometry LaPtBi, YPtBi (Chapter 5) and LuPtBi [38–43], the doped semiconductor $Sn_{1-x}In_xTe$ [44] and the recent new comer ErPdBi [45].

In this dissertation, we present the results of an extensive experimental study on some of these exemplary (candidate) unconventional superconductors: $Cu_xBi_2Se_3$, YPtBi and UCoGe. We employ magnetic and transport measurements as well as the muon spin relaxation (μSR) technique to further unravel the superconducting nature of these novel materials.

1.2 Outline of the thesis

This dissertation consists of six chapters. The content of Chapters 2-6 is laid out as follows.

Chapter 2

This chapter summarizes a number of experimental techniques that have been used throughout this work in the Van der Waals-Zeeman Institute (WZI). Transport measurements were performed using several cryogenic aparatuses: a Maglab Exa, a ^{3}He refrigerator referred to as the Heliox and a dilution refrigerator referred to as the Kelvinox in the following. All three instruments are made by Oxfords Instruments. High pressure measurements at pressures up to 2.5 GPa have carried out using a hybrid piston-cylinder pressure cell. Additionally, the μSR technique used for experiments carried out at the Paul Scherrer Institute (PSI) is briefly discussed in this chapter.

Chapter 3

The theoretical aspects of the research topics presented in this thesis are given in this chapter. The aim is to provide a general picture and links to the experimental work presented later on. We introduce a brief overview of superconductivity, quantum criticality and quantum phase transitions. The recent discovery of FMSC as a novel class of unconventional SCs is discussed; in particular, we focus on the intriguing properties of the latest member of the family, UCoGe. Furthermore, a concise discussion is presented of the recent discovery as well as of the intriguing properties of topological insulators and possible topological superconductors. Subsequently, we discuss superconductivity in a magnetic field. Particularly, we consider the temperature variation of the upper critical field for both conventional BCS *s*-wave and unconventional superconductors. The analysis of the upper critical field is further investigated in details in Chapters 4 and 5 to unravel the superconducting nature of the studied materials.

Chapter 4

Transport measurements were made at both ambient and high pressure on the doped second generation 3D TI $Cu_xBi_2Se_3$. It is demonstrated that the temperature variation of the upper critical field $B_{c2}(T)$ strongly deviates from the spin-singlet Cooper pair state in the conventional BCS formalism. The data rather point to an unconventional polar *p*-wave superconducting phase. Our study strongly supports theoretical proposals that this material is a prime candidate for TSC.

Chapter 5

One of the 111 compounds in the Half Heusler family, YPtBi, is studied by means of transport, magnetic measurements and μSR. AC-susceptibility and DC-magnetization data show unambiguous proof for bulk superconductivity. The zero-field Kubo-Toyabe relaxation

rate extracted from μSR data allows the determination of an upper bound for the spontaneous field associated with odd-parity superconducting pairing. Transport measurements under pressure are used to establish the temperature dependence of the upper critical field, $B_{c2}(T)$, which tells us the superconducting state is at variance with the expectation of simple *s*-wave spin-singlet pairing. The $B_{c2}(T)$ data are consistent with the presence of an odd-parity Cooper pairing component in the superconducting order parameter, in agreement with theoretical predictions for noncentrosymmetric and topological superconductors.

Chapter 6

We present a magnetotransport study on the ferromagnetic superconductor UCoGe. The data, taken on high quality single crystalline samples, identify a significant structure near $B^* = 8.5$ T when the applied magnetic field is parallel to the spontaneous moment. We show that this feature has a uniaxial anisotropy. Moreover, it is very pronounced for transverse measurement geometry and rather weak for longitudinal geometry. The uniaxial nature of the B^* feature and its large enhancement under pressure provide strong indications that it is closely related to an unusual polarizability of the U and Co moments. Transport measurements around the superconducting transition in fixed magnetic fields with $B \parallel b$ corroborate that our samples exhibit an extraordinary S-shaped B_{c2}-curve when properly oriented in the magnetic field. This field reinforced SC appears to be connected to critical spin fluctuations associated with a field-induced quantum critical point.

References

[1] H. K. Onnes, Leiden comm. **120b, 122b**, **124c** (1911).

[2] J. Bardeen, L. N. Cooper, and J. R. Schrieffer, Phys. Rev. **108**, 1175 (1957).

[3] D. D. Osheroff, R. C. Richardson, and D. M. Lee, Phys. Rev. Lett. **28**, 885 (1972).

[4] A. J. Leggett, Rev. Mod. Phys. **47**, 331 (1975).

[5] F. Steglich, J. Aarts, C. D. Bredl, W. Lieke, D. Meschede, W. Franz, and H. Schafer, Phys. Rev. Lett. **43**, 1892 (1979).

[6] A. de Visser, J. J. M. Franse, A. Menovsky, and T. T. M. Palstra, J. Phys. F: Met. Phys. **14**, L191 (1984).

[7] W. Schlabitz, J. Baumann, B. Pollit, U. Rauchschwalbe, H. M. Mayer, U. Ahlheim, and C. D. Bredl, Z. Phys. B **62**, 171 (1986).

[8] R. Movshovich, T. Graf, D. Mandrus, J. D. Thompson, J. Smith, and Z. Fisk, Phys. Rev. B. Condens. Matter **53**, 8241 (1996).

[9] N. D. Mathur, F. M. Grosche, S. R. Julian, I. R. Walker, D. M. Freye, R. K. W. Haselwimmer, and G. G. Lonzarich, Nature **394**, 39 (1998).

[10] S. Saxena, P. Agarwal, K. Ahilan, F. Grosche, R. Haselwimmer, M. Steiner, E. Pugh, I. Walker, S. Julian, P. Monthoux, G. Lonzarich, A. Huxley, I. Sheikin, D. Braithwaite, and J. Flouquet, Nature **406**, 587 (2000).

[11] D. Aoki, A. Huxley, E. Essouche, D. Braithwaite, J. Flouquet, J. P. Brison, E. Lhotel, and C. Paulsen, Nature **413**, 613 (2001).

[12] J. D. Thompson, R. Movshovich, Z. Fisk, F. Bouquet, N. J. Curro, R. A. Fisher, P. C. Hammel, H. Hegger, M. F. Hundley, M. Jaime, P. G. Pagliuso, C. Petrovic, N. E. Phillips, and J. L. Sarrao, J. Magn. Magn. Mater. **226-230**, 5 (2001).

[13] E. Bauer, G. Hilscher, H. Michor, C. Paul, E. Scheidt, A. Gribanov, Y. Seropegin, H. Noël, M. Sigrist, and P. Rogl, Phys. Rev. Lett. **92**, 027003 (2004).

[14] H. Kamimura, H. Ushio, S. Matsuno, and T. Hamada, *Theory of Copper Oxide Superconductors* (Springer-Verlag, Berlin, 2005).

[15] J. G. Bednorz and K. A. Müller, Z. Phys. B **193**, 189 (1986).

[16] H. Hosono, J. Phys. Soc. Jap. **77**, 1 (2008).

[17] J. A. Wilson, J. Phys. Condens. Matter **22**, 203201 (2010).

[18] T. Akazawa, H. Hidaka, T. Fujiwara, T. C. Kobayashi, E. Yamamoto, Y. Haga, R. Settai, and Y. Nuki, J. Phys. Condens. Matter **16**, L29 (2004).

[19] N. T. Huy, A. Gasparini, D. E. de Nijs, Y. Huang, J. Klaasse, T. Gortenmulder, A. de Visser, A. Hamann, T. Görlach, and H. Löhneysen, Phys. Rev. Lett. **99**, 067006 (2007).

[20] D. Fay and J. Appel, Phys. Rev. B **22**, 3173 (1980).

[21] V. P. Mineev and T. Champel, Phys. Rev. B **69**, 144521 (2004).

[22] D. Belitz and T. Kirkpatrick, Phys. Rev. B **69**, 184502 (2004).

[23] T. Kirkpatrick and D. Belitz, Phys. Rev. B **67**, 024515 (2003).

[24] R. Roussev and A. Millis, Phys. Rev. B **63**, 140504 (R) (2001).

[25] A. de Visser, in *Encyclopedia of Materials: Science and Technology (pp 1-6)*, edited by Eds. K. H. J. Buschow *et al*. (Elsevier, Oxford, 2010).

[26] J. E. Moore, Nature **464**, 194 (2010).

[27] J. Burton, Nature **466**, 310 (2010).

[28] M. Z. Hasan and C. L. Kane, Rev. Mod. Phys. **82**, 3045 (2010).

[29] X.-L. Qi and S.-C. Zhang, Rev. Mod. Phys. **83**, 1057 (2011).

[30] A. Kitaev, AIP Conf. Proc. **1134**, 22 (2009).

[31] A. P. Schnyder, S. Ryu, A. Furusaki, and A. W. W. Ludwig, AIP Conf. Proc. **1134**, 22 (2009).

[32] S.-Q. Shen, *Topological Insulators-Dirac Equation in Condensed Matters* (Springer, Berlin, 2012).

[33] P. W. Anderson and P. Morel, Phys. Rev. **123**, 1911 (1961).

[34] R. Balian and N. R. Werthamer, Phys. Rev. **131**, 1553 (1963).

[35] A. P. Mackenzie and Y. Maeno, Rev. Mod. Phys. **75**, 657 (2003).

[36] Y. S. Hor, A. J. Williams, J. G. Checkelsky, P. Roushan, J. Seo, Q. Xu, H. W. Zandbergen, A. Yazdani, N. P. Ong, and R. J. Cava, Phys. Rev. Lett. **104**, 057001 (2010).

[37] T. V. Bay, T. Naka, Y. K. Huang, H. Luigjes, M. S. Golden, and A. de Visser, Phys. Rev. Lett. **108**, 057001 (2012).

[38] G. Goll, M. Marz, A. Hamann, T. Tomanic, K. Grube, T. Yoshino, and T. Takabatake, Phys. B Condens. Matter **403**, 1065 (2008).

[39] A. P. Schnyder, P. M. R. Brydon, and C. Timm, Phys. Rev. B **85**, 024522 (2012).

[40] N. P. Butch, P. Syers, K. Kirshenbaum, A. P. Hope, and J. Paglione, Phys. Rev. B **84**, 220504 (R) (2011).

[41] T. V. Bay, T. Naka, Y. K. Huang, and A. de Visser, Phys. Rev. B **86**, 064515 (2012).

[42] T. V. Bay, M. Jackson, C. Paulsen, C. Baines, A. Amato, T. Orvis, M. C. Aronson, Y. K. Huang, and A. de Visser, Solid State Commun. **183**, 13 (2014).

[43] F. F. Tafti, T. Fujii, A. Juneau-Fecteau, S. René de Cotret, N. Doiron-Leyraud, A. Asamitsu, and L. Taillefer, Phys. Rev. B **87**, 184504 (2013).

[44] S. Sasaki, Z. Ren, A. A. Taskin, K. Segawa, L. Fu, and Y. Ando, Phys. Rev. Lett. **109**, 217004 (2012).

[45] Y. Pan, A. M. Nikitin, T. V. Bay, Y. K. Huang, C. Paulsen, B. H. Yan, and A. de Visser, Europhys. Lett. **104**, 27001 (2013).

Chapter 2 Experimental background and techniques

In this chapter, we present a concise description of the experimental techniques used throughout this thesis: sample preparation and characterization, cryogenic techniques and measurement equipment. In addition, we report the calibration of the RuO_2 thermometer in high magnetic field, as well as of the hybrid piston cylinder pressure cell.

2.1 Sample preparation

All samples used in this thesis were fabricated at the WZI by Dr. Y. K. Huang, except some of the YPtBi batches that were synthesized by Dr. T. Orvis at Stony Brook University. Single crystalline $Cu_xBi_2Se_3$ samples were prepared by a melting method. A flux technique was applied to synthesize YPtBi single crystals. For UCoGe, polycrystals were synthesized first in a home-built mono-arc furnace. Next, single crystals were grown using the Czochralski method in a tri-arc furnace. The details of the sample preparation processes are given in each experimental chapter.

2.2 Sample characterization

Sample characterization is essential prior to making further investigations. This can be accomplished by using various facilities at the WZI. In this work, for instance, X-ray powder diffraction, X-ray back-scattering Laue diffraction and Electron Probe Micro Analysis (EPMA) have been used to investigate in particular sample homogeneity, stoichiometry as well as to identify crystal structures and crystal orientation. In addition, depending on the experimental needs the samples were cut into the desired shapes and dimensions using a spark erosion machine.

2.3 Cryogenic techniques

A majority of this PhD work has been done using several low temperature facilities at the WZI. Each system is briefly described in the following paragraphs:

A home-made ^{4}He bath cryostat using liquid helium and liquid nitrogen can be operated in the temperature range 1.5-300 K. The base temperature can be reached rapidly by directly reducing the vapour pressure of liquid ^{4}He using a rotary pump. This equipment is suitable for initial transport and magnetic measurements such as fast checking of superconductivity and magnetic transitions.

A Maglab Exa cryostat (Oxford Instruments) is used in the temperature range 1.2-400 K. It is equipped with a 9 T superconducting magnet. This cryostat can be used for electrical and ac- and dc-magnetization measurements.

A ^{3}He refrigerator, Heliox VL (Oxford Instruments) [1], is operated in the temperature range 0.23-20 K and is equipped with a 14 T superconducting magnet. Its basic principle of operation is based on the property of ^{3}He as follows. Liquid ^{3}He can be collected in the ^{3}He pot by condensing the ^{3}He gas with help of the 1 K plate which is cooled by the 1 K pot. The

vapour of the ^{3}He is reduced by a sorb pump operated at 4.2 K. Consequently the base temperature (230 mK) is achieved at the ^{3}He pot. A multipurpose sample holder is located 20 cm below the ^{3}He pot in the center of the magnetic field, and is in good thermal contact with the ^{3}He pot. The thermal link is provided by a low eddy current sample holder made of a stainless steel rod that contains sintered copper. The Heliox has a cooling power of 40 μW at 300 mK. The temperature is controlled by a RuO_2 thermometer and a heater made of two 100 Ω resistors in series. Both the thermometer and the heater are connected to a temperature controller (ITC 503, Oxford Instruments). An additional calibrated thermometer was mounted on the sample platform and read out by an ORPX resistance bridge (Barras Provence). The Heliox is a multi-purpose cryostat for measurements of resistivity, magnetoresistivity, ac-susceptibility, thermal expansion and magnetostriction.

A ^{3}He/^{4}He dilution refrigerator, Kelvinox MX100 (Oxford Instruments) [2], is operated in the temperature range 0.02-1.2 K and magnetic field range up to 18 T. The cooling mechanism of the Kelvinox basically relies on the temperature-concentration phase diagram of a ^{3}He/^{4}He mixture. When the mixture is cooled to below 900 mK, it separates into two phases. The lighter 'concentrated phase' with almost pure liquid ^{3}He is floating on top of the heavier 'dilute phase' of superfluid ^{4}He with about 6% ^{3}He. By pumping on the ^{3}He in the dilute phase, ^{3}He atoms 'evaporate' from the pure phase into the dilute phase, as a result of the osmotic pressure. A base temperature as low as 20 mK is achievable in the mixing chamber. For continuous cooling, over a period of even months, the ^{3}He gas is circulated and condensed again at ~ 1.2 K in the 1 K pot. The SC magnet is equipped with a field compensation coil which results in a field smaller than 100 Gauss at the level of the mixing chamber. This prevents eddy current heating of the mixing chamber during field sweeps, and in addition allows for calibration of thermometers in field (see below). The sample holder configuration is like in the Heliox. Moreover, the Kelvinox is equipped with a plastic Swedish rotator with angles tunable from -150° to 150° with a resolution of 0.2°, controlled by an Oxford Instruments Stepper Motor Control Unit model (SMC4). The Kelvinox's cooling power is 100 μW at 100 mK. This is a multi-purpose cryostat like the Heliox, but angular dependence measurements can be performed as well.

In addition, low temperature facilities, including a SQUID at the Néel Institute in Grenoble, France, and a dilution refrigerator at the Paul Scherrer Institute (PSI) in Villigen, Switzerland, have been used. More details about these experimental set-ups can be found in Refs. 3,4,5.

2.4 Calibration of RuO_2 thermometers in high magnetic field

Normally the calibration of commercial RuO_2 thermometers is made in zero magnetic field. However, many experiments are carried out in high magnetic fields. Therefore, it is essential to take into account the effect of the magnetic field on the thermometers, and their calibration in field is desirable. This is especially required for the experiments in the Kelvinox. We have done the calibration as follows. We record a resistance value R of an uncalibrated RuO_2 at the field position and temperature T of a reference thermometer which is kept in the zero field region at a given set point of temperature and magnetic field when their thermal equilibrium is established. Repeating the same measurement for different temperatures in a magnetic field B one gets a data set of R, T and hence a function $T = f(R)$. If we redo the sequence for different magnetic fields, we obtain $T = f(R,B)$. The functions best fitted to the data are listed in the table below. Finally, we establish an average function $T = f(R,B)$ for the calibration

$$T[K]\big|_{B=4(m-1)+n} = f_{4(m-1)} + n\frac{\left|f_{4m} - f_{4(m-1)}\right|}{4};\ m = 1,2,3,4;\ n = 0,1,2,3, \qquad (2.1)$$

where B is magnetic field, and f is a function taken from the table at a corresponding field. Thus, the equation (2.1) allows us to calculate the temperature of the thermometer in a magnetic field.

Magnetic field (T)	T_{RuO2} (K); $x = R_{RuO2}$ (kΩ)
B = 0	$f_0 = y_0 + a_1 e^{(-(x-x_0)/t_1)} + a_2 e^{(-(x-x_0)/t_2)} + a_3 e^{(-(x-x_0)/t_3)}$ $y_0 = 0.006822972$; $x_0 = 6.086899996$ $a_1 = 0.205591216$; $a_2 = 0.590778143$; $a_3 = 0.373789468$ $t_1 = 4.904928233$; $t_2 = 1.44400122$; $t_3 = 0.588363298$
B = 4	$f_4 = y_0 + a_1 e^{(-(x-x_0)/t_1)} + a_2 e^{(-(x-x_0)/t_2)} + a_3 e^{(-(x-x_0)/t_3)}$ $y_0 = -0.027410552$; $x_0 = 6.294999999$ $a_1 = 0.2086686$; $a_2 = 0.532550464$; $a_3 = 0.237164031$ $t_1 = 7.125517874$; $t_2 = 1.401282508$; $t_3 = 0.589069151$
B = 8	$f_8 = y_0 + a_1 e^{(-(x-x_0)/t_1)} + a_2 e^{(-(x-x_0)/t_2)} + a_3 e^{(-(x-x_0)/t_3)}$ $y_0 = -0.005391654$; $x_0 = 6.26$ $a_1 = 0.194515895$; $a_2 = 0.538869589$; $a_3 = 0.223472407$ $t_1 = 0.532865485$; $t_2 = 1.271982504$; $t_3 = 5.146749917$

B = 12	$f_{12} = y_0 + a_1 e^{(-(x-x_0)/t_1)} + a_2 e^{(-(x-x_0)/t_2)} + a_3 e^{(-(x-x_0)/t_3)}$ $y_0 = -0.013366598$; $x_0 = 6.231$ $a_1 = 0.54399839$; $a_2 = 0.223164865$; $a_3 = 0.196428683$ $t_1 = 1.270137$; $t_2 = 5.568462962$; $t_3 = 0.525599692$
B = 16	$f_{16} = y_0 + a_1 e^{(-(x-x_0)/t_1)} + a_2 e^{(-(x-x_0)/t_2)} + a_3 e^{(-(x-x_0)/t_3)}$ $y_0 = 0.011451097$; $x_0 = 6.206$ $a_1 = 0.236606137$; $a_2 = 0.235842934$; $a_3 = 0.466734021$ $t_1 = 2.856972464$; $t_2 = 2.388818387$; $t_3 = 0.702493174$

2.5 Experimental techniques

2.5.1 Electrical resistivity experiment

All resistivity measurements presented in this thesis were performed at the WZI using a standard four point contact method (Fig 2.1). The current (outer) and voltage (inner) leads are thin copper wires (diameter ~ 30 μm), which are soldered to insulated copper heatsinks on the copper sample holder on one end and are mounted to the sample by conductive silver paste on the other end. The value of the contact resistance (a few Ω) is normally small enough to prevent Joule heating at the lowest temperature.

For the ac resistivity measurements, the typical value of the frequency and excitation current used in the Maglab Exa cryostat is f ~16 Hz and I_{exc} ~ 1-5 mA, respectively. For the measurements in the Heliox and Kelvinox we used a Linear Research AC Resistance Bridge model LR 700 with f ~ 13 Hz and I_{exc} ~ 30-300 μA or an EG&G 7265 DSP lock-in amplifier with f ~ 13-13000 Hz and I_{exc} ~ 20-300 μA.

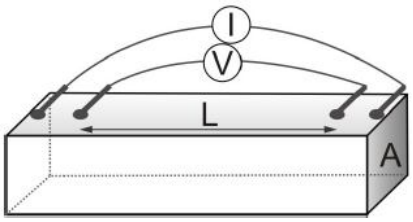

Figure 2.1 A schematic drawing of four point contact resistivity method. In general, the distance L of the voltage contacts is ~ 1-6 mm and the cross section A varies around 1 mm^2.

2.5.2 AC-susceptibility experiment

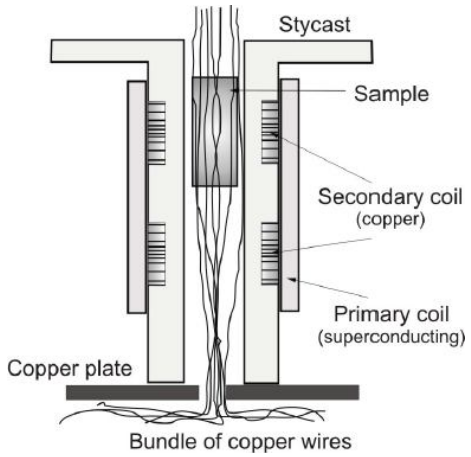

Figure 2.2 A schematic diagram of the mutual-inductance transformer used for ac-susceptibility measurements (picture taken from Ref. 6)

Fig 2.2 shows the schematics of the mutual-inductance transformer used for ac-susceptibility measurements. The bundle of copper wires ensures a good thermal contact between the thermometer at the copper plate (not drawn) and the sample. The basic principle of operation is the following: An ac current is applied to the primary coil, which generates a small magnetic field, the driving field. The induced voltage is measured by two secondary (pick-up) coils. With an empty transformer, the signal is in principle zero since the two secondary coils are wound in opposite direction. When a sample is present in one of the coils, the magnetic field induces a magnetization, and therefore the pick-up coil signal is proportional to the ac-susceptibility. The ac-susceptibility measurements have been done using the Linear Research bridge LR700 with an excitation frequency of 16 Hz and a driving field ~ 10^{-5} T.

2.5.3 High pressure experiment

The hybrid piston cylinder pressure cell used for transport and ac-susceptibility experiments up to 2.5 GPa is illustrated in Fig 2.3. It is made of NiCrAl and CuBe alloys which are strong enough and nonmagnetic [7]. The inner and outer diameters are 6 mm and 25 mm, respectively. The total length of the cell varies slightly with pressure, but at the maximum pressure it is ~ 70 mm. The sample space is 4.7 mm in diameter and is 8 mm long.

A hand press LCP 20 was used to pressurize the cell via a piston, which in turn pressurizes the sample via the pressure transmitting medium. A hydrostatic pressure is ascertained by using Daphne oil 7373 inside a Teflon cylinder.

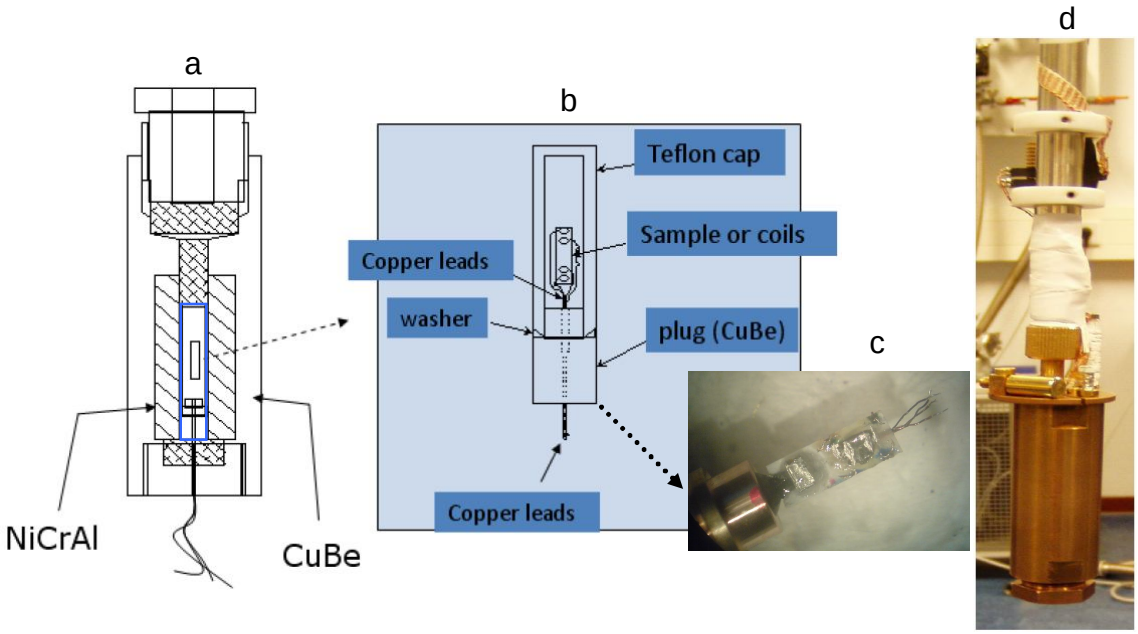

Figure 2.3 A schematic drawing of the pressure cell and a zoom-in of the heart of the cell (a and b, taken from ref. 7). A sample and a Sn manometer supported by a paper construction on a plug (c). A complete cell at the final stage mounted in the insert of the Heliox VL (d).

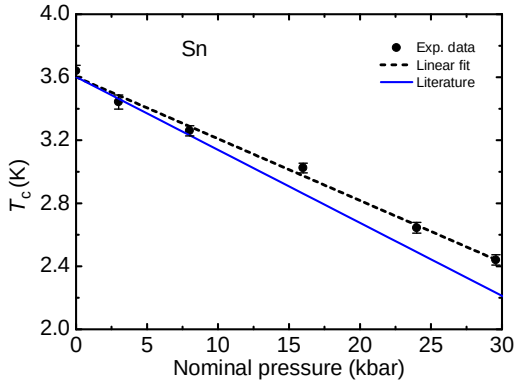

Figure 2.4 Superconducting transition temperature of Sn extracted from ac-susceptibility measurements as a function of pressure (dots) and a linear fit to the data (dashed line). The solid line presents literature data from Ref. 8.

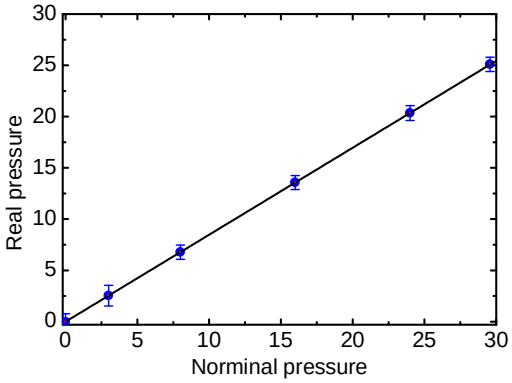

Figure 2.5 Real pressure as a function of nominal pressure. The linear fit to the data (solid line) determines the pressure cell efficiency.

Pressure calibration of the cell is done in situ by measuring the superconducting transition of a Sn sample by AC-susceptibility. Fig 2.4 presents the experimental data and a comparison to the literature to extract the actual pressure. In Fig 2.5 we show the resulting

calibration curve. Consequently, the cell efficiency is 85%, which is slightly larger than in a previous calibration (82%) [9].

2.5.4 MuonSR experiment

μSR stands for Muon Spin Rotation, Relaxation or Resonance. This technique was first developed in the late 1950s as a microscopic probe using the positive muon μ+. By implanting a spin-polarized muon, one at a time, into the bulk of a sample, the information obtained by detecting the resulting decay positron contains various spin-related physical properties of the investigated sample. To date it has become a powerful tool for research in condensed matter physics, such as the study of the magnetic and superconducting properties of heavy-fermion compounds [10, 11].

The μSR experiments have been performed using the μ+SR-dedicated beam line on the PSI-600MeV proton accelerator at the Swiss Muon Source of the PSI in Villigen, Switzerland. We carried out measurements at the General Purpose Spectrometer (GPS) in the temperature range above 1.5 K [4]. To attain lower temperatures (0.02-1.5 K), experiments have been performed using an Oxford Instruments top-loading ^{3}He/^{4}He dilution refrigerator at the Low Temperature Facility (LTF) [5]. Samples used in these μSR experiments were glued to a silver holder using General Electric (GE) varnish.

2.6 Data acquisition and analysis

In the different cryogenic apparatuses described above, the data obtained by various lock-in amplifiers (for example EG&G 7265 DSP), the Linear Research bridge LR700 and other devices were read by the data acquisition computers via an IEEE interface. The ORPX resistance bridge (Barras Provence) was connected to the serial port of the computers via the RS-232 protocol. To control the Heliox and Kelvinox inserts, Oxford Instruments provided standard Labview programs. In order to perform more tailor-made measurements we have improved the software, and other Labview programs have been written for data acquisition. Data files obtained from μSR experiments were produced by the PSI Bulk-μSR time-differential data acquisition programme with extension ".bin" and 512 bytes/records and IEEE real-data format.

Several software packages have been used for data analysis in this work such as: Origin Pro, Mathematica (Wolfram Research), NovelLook and Wimda.

References

[1] Oxford Instruments, Heliox VL, http://www.oxford-instruments.com/.

[2] Oxford Instruments, Kelvinox MX100, http://www.oxfordinstruments.com/.

[3] http://neel.cnrs.fr/.

[4] http://lmu.web.psi.ch/facilities/gps/gps.html.

[5] http://lmu.web.psi.ch/facilities/ltf/ltf.html.

[6] Z. Koziol, Ph.D Thesis (University of Amsterdam, 1994) unpublished.

[7] T. Naka, private communication.

[8] L. D. Jennings et al., Phys. Rev. **112**, 31 (1958).

[9] E. Slooten, Master Thesis (University of Amsterdam, 2009) unpublished.

[10] A. Amato, Rev. Mod. Phys. **69**, 1119 (1997).

[11] S.J. Blundell, Contemporary Physics **40**, 175, (1999).

Chapter 3 Theoretical aspects

This chapter summaries theoretical aspects of the research themes presented throughout the PhD work. We start with a general description of quantum criticality and quantum phase transitions. Then the focus is directed towards superconductivity, especially to the novel class of ferromagnetic superconductors with the case study UCoGe. Next, a brief overview is presented of a new research field in condensed matter physics: topological insulators and topological superconductors. Subsequently, we discuss superconductivity in a magnetic field. In particular, we consider the upper critical field for both conventional BCS s-wave and unconventional superconductors. These theoretical aspects will be applied in the case studies of the doped topological insulator $Cu_xBi_2Se_3$ and the noncentrosymmetric superconductor YPtBi.

3.1 Ferromagnetic superconductors

3.1.1 Quantum criticality

Phase transitions are not only simply ubiquitous in nature but also play a crucial role in shaping the world. Macroscopically, phase transitions in the universe form galaxies, stars and planets. Phase transitions in our daily life are the transformation of for instance water between ice, liquid and vapor. These phase transitions are called thermal or classical and are controlled by thermal fluctuations. Therefore, in the classical world, matter in equilibrium freezes at absolute zero temperature in order to minimize the potential energy.

Quantum mechanics, however, allows fluctuations even at zero temperature. Once such quantum fluctuations are sufficiently strong, the system undergoes a quantum phase transition as illustrated in Fig. 3.1 [1]. Quantum phase transitions (QPTs) are driven by a non-thermal parameter *r*, such as pressure, magnetic field, chemical doping or electron density. By changing the control parameters one is able to tune the system to a transition point, the quantum critical point (QCP).

A continuous phase transition can usually be described by an order parameter, a concept first introduced by Landau. This parameter is a thermodynamic quantity that depends on the state of the system. Its thermodynamic average is equal to zero in the disordered phase

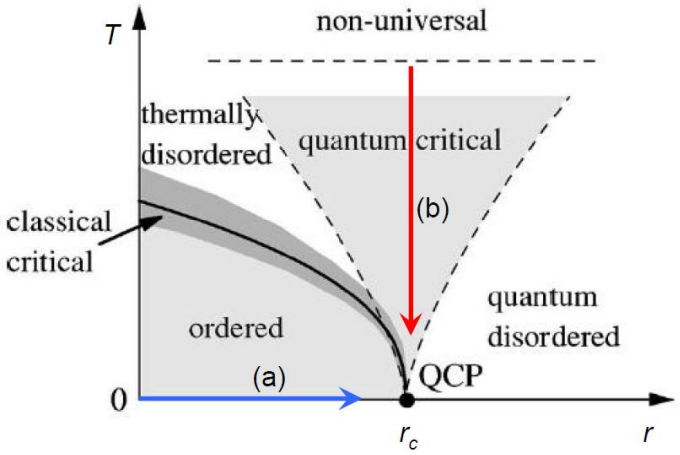

Figure 3.1 Global phase diagram of continuous phase transitions. *r* depicts the non-thermal control parameter, and *T* is the temperature. The solid line separates ordered and disordered regions, and ends at the QCP. The shadowed region close to this boundary implies the critical state is classical. The area bounded by the dashed lines given by $k_B T \propto |r - r_c|^{\nu z}$ indicates the quantum critical region. On the right of this region is the quantum disordered phase. The system can be tuned to the QCP by means of either changing $r \rightarrow r_c$ at $T = 0$ (a) or driving $T \rightarrow 0$ at $r = r_c$ (b) (picture taken from [1]).

and to non-zero in the ordered phase, *e.g.* the ordered moment M for ferromagnetism or the energy gap of a superconductor. Furthermore, the correlation length ξ of the system, that expresses the spatial range of correlation of the order parameter, turns out to be long-ranged when approaching the phase transition or the critical point. Notably, close to the QCP, the correlation length diverges, as a power law

$$\xi \propto t^{-\nu}, \tag{3.1}$$

where ν is the correlation length critical exponent, and t represents some dimensionless distance from the critical point. It can be defined by $t = |T\text{-}T_c|/T_c$ for the classical phase transitions at non-zero temperature T_c or by $t = |r\text{-}r_c|/r_c$ for QPTs.

Analogous to the length scale, the correlations of the order parameter fluctuations in time can be defined as τ_c, which is the typical time scale for the decay of the fluctuations due to a perturbation

$$\tau_c \propto \xi^z \propto t^{-\nu z}, \tag{3.2}$$

where z is the dynamical critical exponent. In addition, a critical frequency ω_c is defined by $1/\tau_c$. At the classical critical point, $\omega_c \rightarrow 0$ or the typical energy scale becomes zero, and this is called critical slowing down

$$\omega_c(t \rightarrow 0) \propto 1/\tau_c \rightarrow 0. \tag{3.3}$$

It is worth to notice that for the classical case, the kinetic and potential energy operators do not commute. This implies the dynamics and statistics are decoupled while, in contrast, for the quantum phase transition they are coupled [1].

In order to clarify the importance of quantum fluctuations at very small but non-zero T, one should take into account two typical energy scales: $\hbar\omega$ and k_BT. The quantum fluctuations remain dominant down to very low T as long as $\hbar\omega \gg k_BT$. As depicted by arrows in Fig. 3.1, quantum criticality can be studied both theoretically and experimentally by not only varying the control parameter r at $T = 0$ but also by lowering the temperature T at r_c.

Heavy fermion systems are model systems in which to investigate QPTs. In these systems, the Kondo effect, that quenches the local moment of the *f*-electrons by conduction electron screening, competes with the Ruderman-Kittel-Kasuya-Yosida (RKKY) interaction, which favours long-range magnetic order. This competition results in an unmatched tunability of magnetic phase transitions [2–5]. Changing the non-thermal control parameter r, such as the magnetic field [6–10], pressure [11–14] or chemical doping [15–20], suppresses the magnetic ordering and concurrently tunes the system to the QPT at the QCP $r = r_c$.

3.1.2 Ferromagnetic superconductors

Superconductivity was discovered in a remarkable experiment carried out in 1911 by Heike Kamerlingh Onnes in Leiden [21]. More than 40 years later, the microscopic theory by Bardeen, Cooper and Schrieffer (BCS) successfully explained the origin of this fascinating phenomenon in most superconducting materials [22]. The fingerprint of this theory is the existence of Cooper pairs. A Cooper pair is a bound state of two electrons which is formed near the Fermi level by an attractive interaction mediated by lattice vibrations. The symmetry of the Cooper pairs can be classified by the total spin S and the total angular momentum L. In general, a two-electron system can have spin S = 0 or 1, and L = 0, 1, 2, 3,… Since the electrons are fermions, the total wave function of the Cooper pair state, which consists of a product of spatial and spin components, must be anti-symmetric under the exchange of particles due to the Pauli exclusion principle. This results in even spatial and odd spin functions or vice versa. Therefore, one can distinguish superconductors with the spin-singlet state (S = 0)

$$\phi_{ss} = \frac{1}{\sqrt{2}}\left(\left|\uparrow\downarrow\right\rangle - \left|\downarrow\uparrow\right\rangle\right) \tag{3.4}$$

e.g. s-wave (S = 0, L = 0) and *d*-wave (S = 0, L = 2), and with the spin-triplet state (S = 1)

$$\phi_{st} = \begin{cases} \left|\uparrow\uparrow\right\rangle \\ \frac{1}{\sqrt{2}}\left(\left|\uparrow\downarrow\right\rangle + \left|\downarrow\uparrow\right\rangle\right) \\ \left|\downarrow\downarrow\right\rangle \end{cases} \tag{3.5}$$

e.g. p-wave (S = 1, L = 1) and *f*-wave (S = 1, L = 3). Here $\left|\uparrow\uparrow\right\rangle$ and $\left|\downarrow\downarrow\right\rangle$ are called the equal-spin pairing (ESP) states.

The superconducting state with S = 0, L = 0 (*s*-wave) is fully explained by the standard BCS theory, and therefore called conventional. However, with the experimental discovery of certain classes of superconductors which go beyond the understanding of the standard BCS scenario, the field of unconventional superconductivity begun. These materials with condensates made up of lower symmetry Cooper pairs (*d*-wave, *p*-wave,…) are non *s*-wave superconductors. Unconventional superconductivity has been found in numerous materials over the last forty years. The prime example is ^{3}He [23,24], and later on heavy fermion SCs (see for instance [25–33]) and high temperature superconductors (cuprates [34,35] and iron pnictides [36,37]) were discovered.

According to the BCS theory, SC is incompatible with ferromagnetic order, while under special conditions it may coexist with antiferromagnetism. However, around 1980, it

was theoretically predicted that SC with ESP states could exist in itinerant ferromagnets (*p*-wave SC) [38] close to a FM QCP. Here the exchange of longitudinal spin fluctuations is proposed to mediate superconductivity. Twenty years later, the first ferromagnetic superconductor UGe_2 was discovered [30,39]. Subsequently, three more FMSCs URhGe [31,40], UIr [41–43] and UCoGe [44–46] were found. To date, a comprehensive, quantitative theory to fully resolve the superconducting pairing issue in FMSCs is not at hand.

In order to offer a qualitative interpretation for the coexistence of FM and SC near a FM QCP, spin fluctuation models have been used [38]. Within these models, the magnetic state can be understood in terms of an exchange interaction $\bar{I}$ and a Stoner enhancement factor $S = (1-\bar{I})^{-1}$. For the critical value $\bar{I} = 1$, a second-order quantum phase transition emerges, and the system transforms from the paramagnetic phase ($\bar{I} < 1$) to the ferromagnetic ($\bar{I} > 1$) phase (Fig. 3.2a). Notably, in the ferromagnetic regime, *p*-wave SC with ESP states is possible with different T_c's for the spin up ($|\uparrow\uparrow\rangle$) and spin down ($|\downarrow\downarrow\rangle$) states. This implies two superconducting phases can be present [38,47,48]. However, the emergence of these two superconducting phases depends sensitively on the details of the band structure. A pictorial of the coexistence of SC and magnetism in the spin-fluctuation model is given in Fig. 3.2b [49]. In contrast to the model prediction, SC was not observed in the PM phase in the cases of UGe_2 and UIr. A possible explanation is that ferromagnetic spin waves (magnons) couple to the longitudinal magnetic susceptibility which results in an enhancement of T_c in the FM phase [49,50]. A comprehensive treatment has been made by Roussev and Millis [50] where SC coexists with FM, leading to a superconducting dome and nonzero T_c at the QCP, as illustrated in Fig. 3.2c.

In UCoGe, muon spin rotation/relaxation (μSR) [51], nuclear magnetic resonance (NMR) and nuclear quadrupole resonance (NQR) [52,53] measurements provide unambiguous evidence that SC is driven by ferromagnetic spin fluctuations and that SC and FM coexist microscopically. The pairing mechanism for *p*-wave SC understood in terms of spin fluctuations is qualitatively illustrated in Fig. 3.3 (left) [54], where it is energetically favorable for two electrons to share the same polarization cloud. Approaching the QCP, however, the experimental phase diagram [46] of UCoGe deviates from the theory by Fay and Appel [38]. Upon increasing the external pressure, FM is depressed and disappears at p_c, while, most surprisingly, SC is enhanced, and even exists in the PM phase, unlike in other FMSCs. At $p > p_c$ SC is depressed. In fact, the unconventional superconducting state in the ferromagnetic phase of UCoGe can be considered as an analogue of the superfluid non-unitary phase A_2 of ^{3}He in a magnetic field [55]. A symmetry group analysis for triplet

superconducting order parameters using two band SC [56,57] explains the experimental temperature (T)- pressure (p) phase diagram of UCoGe, Fig. 3.3-right.

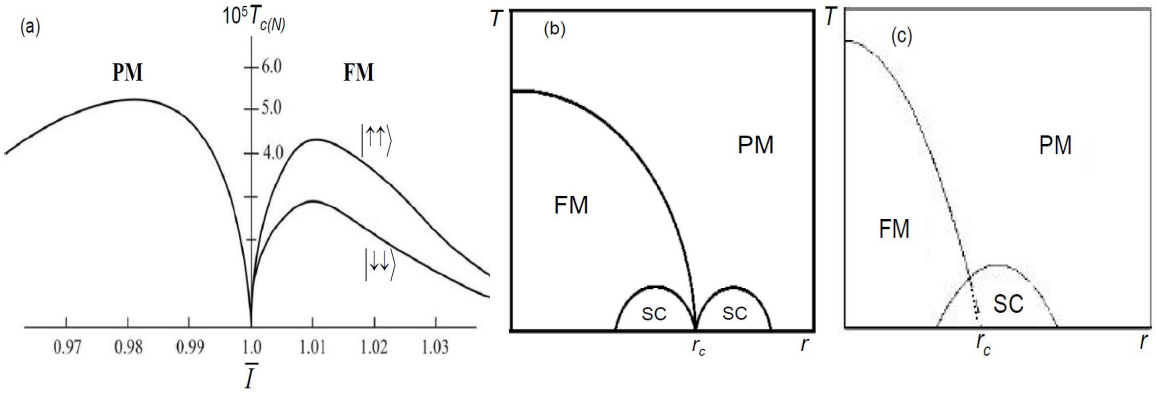

Figure 3.2 (a): Generic phase diagram of a p-wave SC. The superconducting transition temperature $T_{c(N)}$ as a function of the Stoner parameter $\bar{I}$ in the paramagnetic (PM) phase and the ferromagnetic (FM) phase. $T_{c(N)}$ is normalized by the Fermi temperature T_F. $|\uparrow\uparrow\rangle$ and $|\downarrow\downarrow\rangle$ in the FM phase indicate the ESP components (adapted from [38]). (b): Temperature (T) - control parameter (r) phase diagram of a FMSC according to the model given in [38]. SC emerges in both FM and PM phases centered around the QCP at r_c. To date, the SC dome in the PM phase has not been experimentally observed (adapted from [49]). (c): Temperature (T) - control parameter (r) phase diagram of a FMSC, where superconducting transition temperature T_c is finite at the QCP at r_c, and superconductivity coexists with ferromagnetism (adapted from [50]).

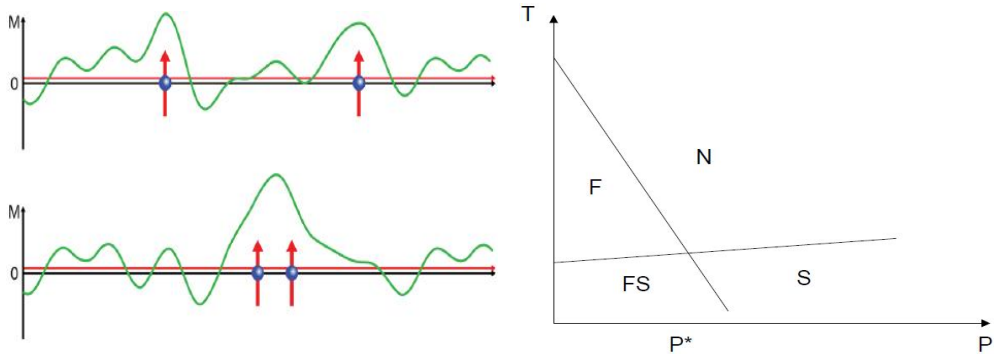

Figure 3.3 Left: Cartoon of electron pairing due to magnetic fluctuations. Non-zero average of the magnetization (upper, red horizontal lines in both frames) with a large fluctuating part. A local polarization cloud is created surrounding the electrons. For paired electrons (lower frame), the energy is lower than separate electrons (upper frame) (taken from [54]). Right: Generic temperature (T) - pressure (p) phase diagram of the FMSC UCoGe. SC is present in both the ferromagnetic (FS) and normal paramagnetic (S) phase. N and F depict the normal and ferromagnetic phase, respectively. Ferromagnetic order is not observed for pressure $p > p^*$ (adapted from [56]).

3.2 Topological insulators and superconductors

3.2.1 Topological insulators

TIs have emerged in condensed matter physics over the last few years as a completely new paradigm for research into novel phases of matter. This research field was theoretically predicted in 2005 [58] and the first TI was confirmed by experiment two years later [59]. Intriguing about TIs in contrast to ordinary bulk insulators is the existence of topologically non-trivial conducting surface states which are protected by time reversal symmetry (TRS). This means these surface states are in-sensitive to scattering from non-magnetic impurities.

In order to explain what a TI exactly is, it is first useful to consider one of the basic phenomena in condensed matter physics, the integer quantum Hall effect (IQHE). Consider a two dimensional system of classical electrons with charge *e* and mass *m* subjected to a perpendicular magnetic field *B*. In this case the charge carriers follow cyclotron orbits with the energy quantized in Landau levels

$$E_n = \hbar\omega_c(n+1/2), \tag{3.6}$$

where $\omega_c = eB/m$ is the cyclotron frequency, and $\hbar$ is Planck's constant. For a sufficiently large magnetic field, each Landau level is highly degenerate and the free electrons of the system occupy a few Landau levels only. This is the IQHE. In this regime the current flows along the edges of the sample, and the Hall conductivity is quantized

$$\sigma_{xy} = ne^2/h. \tag{3.7}$$

Here the filling factor *n* is a positive integer, and *n* turns out to be what is known as a Chern number: a topological invariant. Therefore, an IQH system possesses gapless edge states crossing the Fermi level while the bulk is insulating.

The main difference between an IQH system and an ordinary insulator is a matter of topology. According to the band structure point of view, the Bloch Hamiltonians of two given systems are topologically equivalent as long as they can be deformed continuously into each other, *i.e.* without closing the energy gap [60]. The Hamiltonian of an IQH insulator and that of a classical insulator belong to different topology classes. A topology class is generally defined by a topological invariant. For an IQH state, the topological invariant is the Chern number *n*, that remains unchanged as the Hamiltonian varies smoothly. The Chern number is related to an important quantity, the Berry phase, or geometric phase. The Berry phase is a phase difference in k-space of the wave function of a system when it is subjected to a cyclic adiabatic process [61,62]. The Berry phase is zero for ordinary insulators and an integer times π for TIs [60].

Quantum spin Hall effect (QSHE) is another example of a topological phase. In contrast to IQHE, in the quantum spin Hall effect, no magnetic field is required. The spin-orbit coupling of the band structure in the QSHE takes over the role of the magnetic field in the charge Hall effect. Again, the system possesses robust edge states that have a quantized spin-Hall conductance $\sigma_s = 2(e/4\pi)$. Here the charge conductance vanishes due to two equal currents flowing in opposite directions. Each conductivity channel contains its own independent Chern number $n_\uparrow$ or $n_\downarrow$, therefore the total Chern invariant for the Hall conductivity $n = n_\uparrow + n_\downarrow = 0$. In this case the Chern invariant cannot be used to classify the QSH state. Instead, a different topological invariant of the $\mathbb{Z}_2$ type ν, which is 0 or 1 [58], takes a value of 1 for the QSHE indicative of the topological character. Because of spin-orbit coupling the surface or edge states provide a net spin transport. The surface states have a Dirac-like dispersion and are topologically protected. This system is an example of a real 2D TI [59,60], see Fig. 3.4 for an illustration.

Furthermore, identification whether a system is topologically trivial or non-trivial is based on Kramer's theorem. As consequence of TRS for all spin 1/2 systems Kramer's theorem states that the eigenstates of a TR invariant Hamiltonian are at least twofold degenerate at time invariant points in *k*-space. In case of a 1D Brillouin zone ($k \geq 0$), these points are $k_x = \Gamma_a \equiv 0$ and $k_x = \Gamma_b \equiv \pi / a$. The way the time invariant points are connected depends on the topology of the system [60]. When the connection is pairwise (Fig. 3.5 - left), one can tune the system in such a way that none of these edge states crosses the Fermi level. However, this is not the case for an odd number of states passing E_F (Fig 3.5 - right). As a result, the former system is topologically trivial, with $\nu = 0$, whereas the latter is topologically nontrivial, with $\nu = 1$.

Another consequence of Kramer's theorem in the context of the fully spin polarized edge states of a TI or QSHE system is the absence of backscattering, even for strong disorder. Fig 3.6 shows schematically how an electron with spin 1/2 in a QSH edge state scatters from a non-magnetic impurity [63]. Due to the presence of the impurity its spin must reverse by moving either clockwise (Fig. 3.6 - upper frame) or anticlockwise (Fig. 3.6 - lower frame) around the impurity. As a result, the phase difference of the spin wave function is 2π. Also, quantum mechanics tells us for spin 1/2 systems the wave function satisfies $\Phi(\theta + 2\pi) = -\Phi(\theta)$. Thus, these two backscattering paths interfere destructively, which allows perfect transmission, with respect to such scattering from non-magnetic impurities. If the edge states possess an even number of left-moving channels and an even number of right-

moving channels, an electron can be scattered from the left-movers to the right-movers without reversing its spin. In this manner, the interference is non-destructive and thus there exists dissipation. TRS will be broken and consequently the interference is no longer destructive if the impurity carries a magnetic moment. Therefore, in QSH systems and in 2D TIs the elastic backscattering is forbidden, and the surface states are thus described as being robust and topologically protected by TRS.

Hitherto, we have been discussing topological states protected by TRS, next we discuss why a system could possesses such special surface states. TIs originate from the effect of strong SOC, which can lead to what is known as band inversion. Fig. 3.7 shows an example of band inversion in the 3D TI Bi_2Se_3 [64]. Consider the atomic energy levels at the Gamma point near the Fermi level E_F. These are mainly dominated by the p orbitals of Bi ($6s^26p^3$) and Se ($4s^24p^4$). Three effects eventually take place. Firstly, the chemical bonding between the Bi and Se atoms hybridizes their energy states. This process lowers the Se energy levels and, in contrast, raises the states of Bi. Next, the crystal-field splitting is added. The p_z levels of the Bi and Se are split off from the corresponding p_x and p_y orbitals, and are close to E_F, while the $p_{x,y}$ levels remain degenerate. In the last step, the effect of SOC is taken into account. The SOC Hamiltonian describing the system is given by $H_{SOC} = \lambda \mathbf{L}.\mathbf{S}$, where **L** and **S** are the orbital and spin angular momentum operators, respectively, and λ is a SOC parameter. Only when λ is sufficiently strong, the two states nearest to E_F turn out to be inverted which thus alters the parity of the occupied valence levels (below E_F) as a whole. For TIs with an inversion center [60] this is sufficient to make the bulk band structure topologically non-trivial.

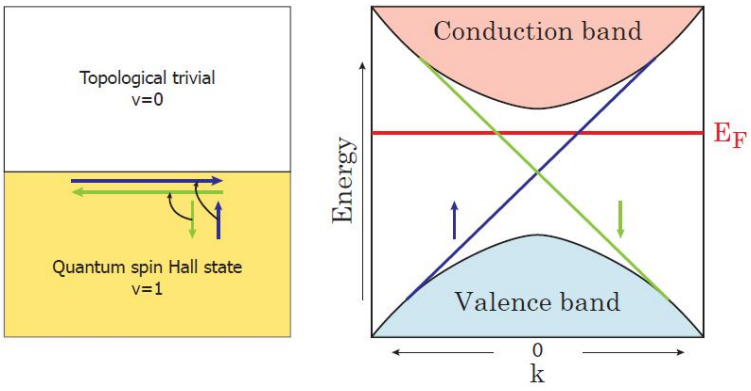

Figure 3.4 Left panel: A comparison between an ordinary insulator ($\nu = 0$) and the QSHE where the edge states are topologically nontrivial ($\nu = 1$). Right panel: the energy dispersion of the topologically nontrivial surface states (in the left panel) with up and down spins crossing the Fermi energy [60].

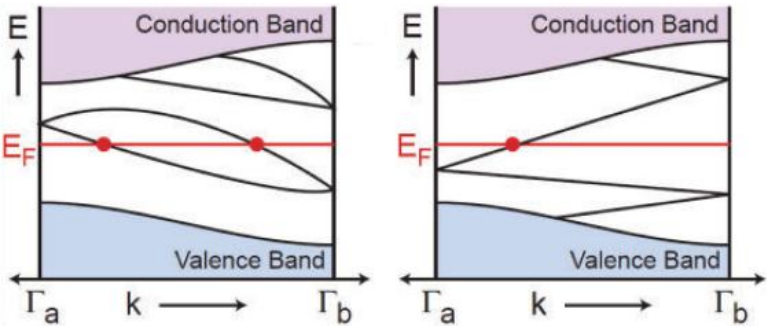

Figure 3.5 The electronic dispersions at two Kramers points Γ_a and Γ_b [60]. Left frame: Even number of states crossing the Fermi level results in topologically trivial states. Right frame: Topologically nontrivial states due to an odd number of states crossing the Fermi level.

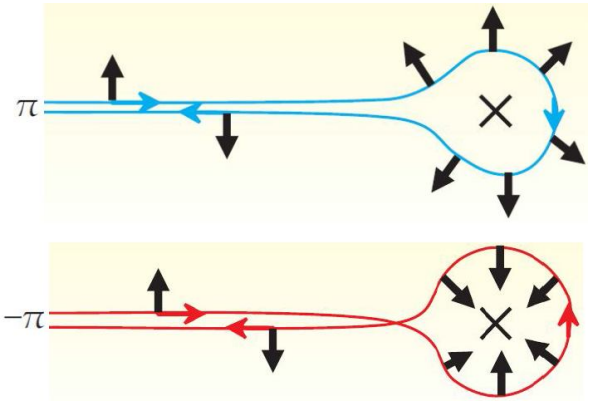

Figure 3.6 A scheme of a backscattering process taking place when an electron with spin 1/2 is subjected to a nonmagnetic impurity. Upper frame: spin rotates by π. Lower frame: spin rotates by $-\pi$. Adapted from [63].

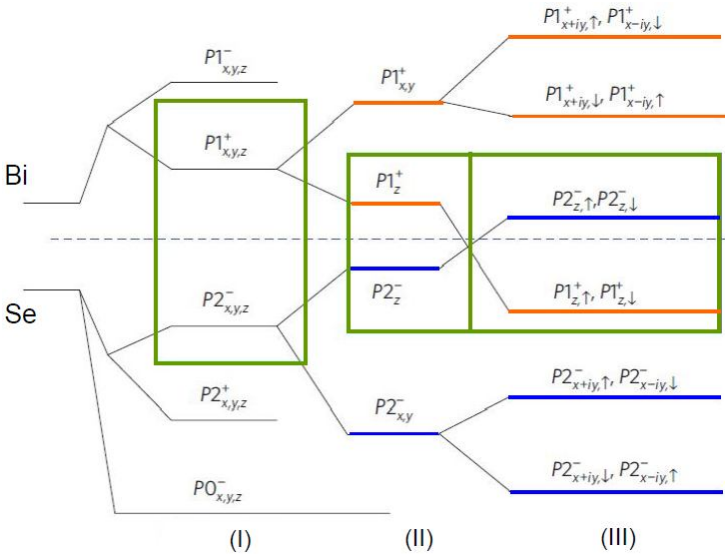

Figure 3.7 Energy levels of the 3D TI Bi_2Se_3 close to the E_F under the effects of chemical bonding (I), crystal field splitting (II) and SOC (III). The rightmost rectangle indicates the SOC, which leads to the band inversion. Picture taken from [64].

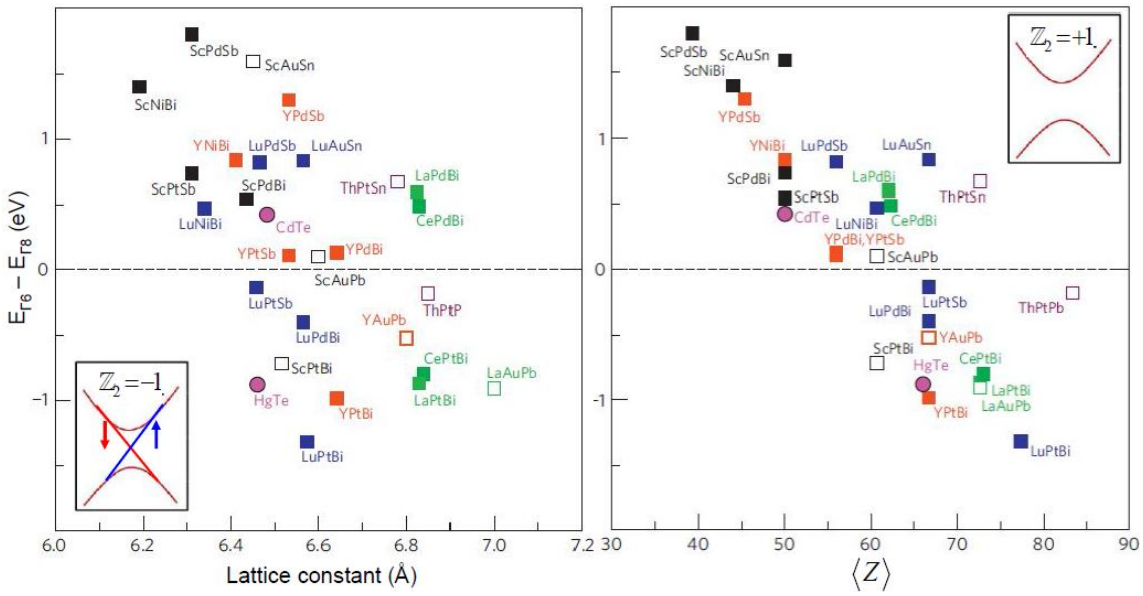

Figure 3.8 Band inversion of a number of Half-Heusler compounds as a function of the lattice constant and average nucleus charge $\langle Z \rangle$. There is a bulk bandgap between trivial states when the band inversion is absent (upper-right inset), and topologically nontrivial phases exist, providing protected edge states due to band inversion (lower-left inset) for the Half-Heusler systems. Adapted from [65].

Electronic structure calculations taking into account SOC and TRS show that several Half-Heusler compounds with a 111 stoichiometry also exhibit topological band inversion [65,66]. Fig. 3.8 shows that many systems are predicted to have a 'negative gap'- *i.e.* band inversion straddling around E_F, and thus be topological materials. The great diversity of the systems that can form Half-Heusler compounds yields a rich hunting ground for new topological non-trivial phases. In the case of the 111 system the band inversion takes place between the twofold-degenerate *s*-like Γ_6 and fourfold-degenerate *p*-type Γ_8 energy states in these materials and depends strongly on both the lattice constant and the SOC strength represented by an average charge $\langle Z \rangle$ of the nuclei. Consequently, the systems can be either topologically non-trivial (with $\Gamma_6 - \Gamma_8 < 0$; negative energy gap) or topologically trivial (with $\Gamma_6 - \Gamma_8 > 0$; positive energy gap). Amongst these Half Heusler compounds, four bismuth-based materials are also found to exhibit SC: YPtBi [67,68] (chapter 5), LaPtBi [69,70], LuPtBi [71] and ErPdBi [72].

Having briefly discussed 2D (QSHE) and 3D TIs, we continue by introducing a general picture of how to classify TIs and TSCs by their symmetries. Upon the presence or

absence of time-reversal symmetry (Θ), particle-hole symmetry (Ξ) and sublattice or chiral symmetry ($\Pi = \Theta\Xi$), the topological classifications for TIs and TSCs whose dimensionalities, *d*, are up to 8 are summarized in Fig. 3.9 [60,73]. Together these three symmetries form ten symmetry classes depicted by the Altland-Zirnbauer (AZ) notation. The symmetries can take a value of 0 or ±1, which denotes the absence or presence of the symmetries in the system, respectively. The ±1 indicates the value of Θ^2 and Ξ^2. The topological classifications are denoted by 0, $\mathbb{Z}$ and $\mathbb{Z}_2$, where 0 indicates topological phases are absent. $\mathbb{Z}$ presents a corresponding topological invariant that can take any positive integer value like the Chern number in the IQHE, and $\mathbb{Z}_2$ indicates a corresponding topological invariant that can take a value of 0 or ±1 as in the topological insulators. In this figure, one can locate the systems discussed so far. For example, the 2D IQHE denoted by $\mathbb{Z}$ is given by the entry in the first row and column 2 without any symmetry. The first TI experimentally realized is the HgTe/CdTe quantum well [59], d = 2 and row 7. Systems presented in this PhD work are $Cu_xBi_2Se_3$ (d = 3, row 6) and YPtBi (d = 3, row 8) which will be extensively discussed in the following chapters.

Notation	Symmetry			Dimension							
AZ	Θ	Ξ	Π	1	2	3	4	5	6	7	8
A	0	0	0	0	Z	0	Z	0	Z	0	Z
AIII	0	0	1	Z	0	Z	0	Z	0	Z	0
AI	1	0	0	0	0	0	Z	0	Z_2	Z_2	Z
BDI	1	1	1	Z	0	0	0	Z	0	Z_2	Z_2
D	0	1	0	Z_2	Z	0	0	0	Z	0	Z_2
DIII	−1	1	1	Z_2	Z_2	Z	0	0	0	Z	0
AII	−1	0	0	0	Z_2	Z_2	Z	0	0	0	Z
CII	−1	−1	1	Z	0	Z_2	Z_2	Z	0	0	0
C	0	−1	0	0	Z	0	Z_2	Z_2	Z	0	0
CI	1	−1	1	0	0	Z	0	Z_2	Z_2	Z	0

Figure 3.9 Classifications of TIs and TSCs. The notation of Altland and Zirnbauer (AZ) is used to denote ten different symmetry classes. Depending on the presence or absence of the symmetries Θ, Ξ and Π (see text), TIs and TSCs are classified with regards to their dimension, AZ symmetry, whereby the entries 0, $\mathbb{Z}$, and $\mathbb{Z}_2$ label the topological classes. The entries with circles are explained in the text as being relevant to particular material realizations. Table adapted from [60].

3.2.2 Topological superconductors

3.2.2.1 Odd and even-parity superconductors

In general, the symmetry group G^{sym} of the normal phase of a crystalline SC is given by

$$G^{sym} = G_0 \times G_s \times T \times U(1), \tag{3.8}$$

where G_0, G_s, T, and $U(1)$ presents orbital rotation, spin rotation, time-reversal symmetry and gauge symmetry, respectively [74]. Generally speaking, in conventional SC, only $U(1)$ is broken when the system undergoes SC, while in case of unconventional SC, at least one of the other symmetries is broken as well. For instance, time reversal symmetry T is broken in the SC phase of the FMSC UCoGe [47] and the correlated metal Sr_2RuO_4 [75,76].

The superconducting pair wave function, which yields the energy gap function or order parameter, is comprised of a spatial part (in momentum space k) and a spin part, S. For even parity (total spin $S = 0$), the wave function is invariant under inversion symmetry, while, in contrast, the wave function changes sign for odd parity ($S = 1$). Based on the gap symmetry one can distinguish different SCs. For conventional *s*-wave SCs, the superconducting gap has the highest symmetry and is nearly isotropic (although in practice there may be some anisotropy in the k-dependence of the gap magnitude). For unconventional SCs, the gap function has a lower symmetry. In Fig 3.10 sketches are given of examples of various unconventional superconducting states whose wave functions are classified by the combinations of S_z (the z-spin component) and m (the angular orbital momentum) in the superfluid phase of ^{3}He [77–79]. They include the A_1 phase with $|S_z = 1, m = 1\rangle$, the ABM (Anderson-Brinkman-Morel) phase with $|S_z = 1, m = 1\rangle$ and $|S_z = -1, m = 1\rangle$ and the BW (Balian-Werthamer) phase with $|S_z = -1, m = 1\rangle$, $|S_z = 0, m = 0\rangle$ and $|S_z = 1, m = -1\rangle$. Consequently, the corresponding gap symmetries of these states can be realized as shown in Fig. 3.11. In addition, there are polar and planar states, which are equally weighted superpositions of the two states with $|S_z = -1, m = 1\rangle$ and $|S_z = 1, m = -1\rangle$, and the Scharnberg-Klemm (SK) state [80], which possesses a similar gap symmetry as in the ABM state.

In the following chapters, we investigate superconducting phases of several materials according to these classifications.

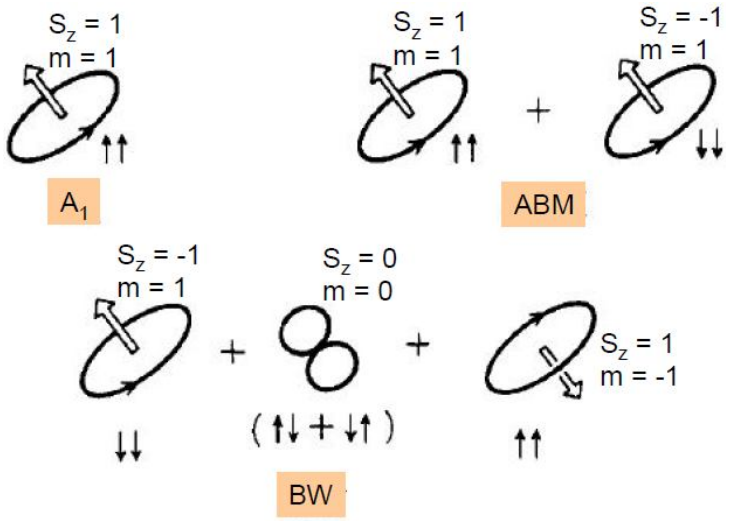

Figure 3.10 General scheme for the orbital and spin states in the superfluid phases A_1, ABM and BW of ^{3}He. Picture adapted from [79].

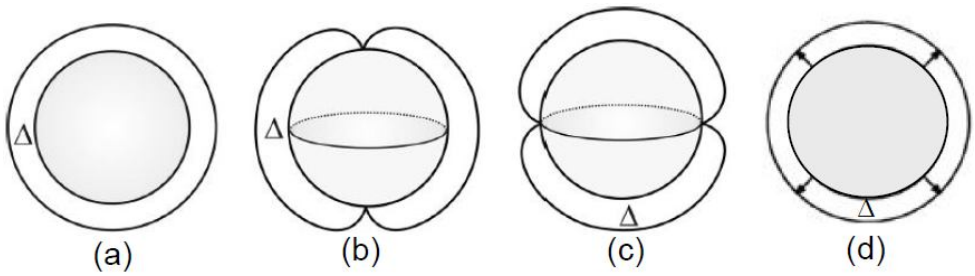

Figure 3.11 Superconducting energy gap at the Fermi surface for different states. (a) The isotropic gap of an *s*-wave superconductor. (b) The axial or point node gap as in the ABM state (the superfluid A phase of ^{3}He) where the gap terminates at two points (poles). (c) The polar (as in the planar-B phase of ^{3}He) state where the gap vanishes along a line on the Fermi surface. (d) Full gap (BW or as in the B phase) state of a *p*-wave superconductor.

3.2.2.2 Topological superconductors

Topological phases in superconductors have attracted ample attention even long before the birth of TIs. Topological superconductivity can be understood as a state that possesses a full superconducting gap in the bulk, but possesses topological edge states. The most well known candidate for TSC is superfluid ^{3}He (phase B) [77,78,81] described by the topological invariant $\mathbb{Z}$. Yet another promising test case for 2D chiral superconductivity is the triplet superconductor Sr_2RuO_4 [76], but experimental evidence remains under debate, for instance, as regards the existence of the gapless surface states [82]. Other candidate topological superconductors can be found among the doped TI $Cu_xBi_2Se_3$ [83,84], the half-Heusler 111

platinum bismuthides LaPtBi, YPtBi, LuPtBi [67–71,85] and the doped semiconductor $Sn_{1-x}In_xTe$ [86].

There is a close analogy between TIs and SCs in view of the Hamiltonian describing the systems. In particular, the Bogoliubov-de Gennes (BdG) Hamiltonian for the quasiparticles of a SC is similar to the Bloch Hamiltonian for a band insulator, where the superconducting gap corresponds to the band gap of the insulator. However, the Hamiltonian for TSC obeys the particle-hole symmetry which is not the case for TIs.

A time reversal invariant TSC possesses a full superconducting energy gap in the bulk but gapless surface states consisting of a single Majorana cone, which emerges for instance in the case of the ^{3}He-B phase. This class of SC is denoted by the $\mathbb{Z}_2$ invariant in 1D and 2D [75,87–89] and by the integer $\mathbb{Z}$ in 3D [75,88]. Based on the analogy between the Hamiltonians of a TRI superconductor and the QSHE, it has been argued that spin-up and spin-down electrons in the spin-triplet pairing channel form $p_x + ip_y$ and $p_x - ip_y$ Cooper pairs for a 2D TRI superconductor; *i.e.* the edge states of the system consist of spin-up and spin-down states with opposite chiralities [82]. As in the QSHE, these edge states are protected by TRS, and thus should be gapless and without any backscattering (see 3.2.2.1). In a 3D TRI superconductor, where both spin polarization and orbital angular momentum are vectors, the system is analogous to the case of the ^{3}He-B phase with a full pairing gap in the bulk. In contrast to 3D TIs, the surface states of the TSC may possibly host Majorana zero modes.

Along with time reversal invariant (TRI) TSCs, time reversal breaking (TRB) TSCs also attract tremendous interest as they give rise to non-Abelian statistics [90,91] and topological quantum computation, an active field of research [92]. Theoretically, a criterion for identification of topological phases in TRI and TRB superconductors has been proposed in details in Refs. [93–95].

3.3 Upper critical field B_{c2}

In a magnetic field superconductivity is suppressed. For a standard BCS SC this is predominantly due to two interactions of the magnetic field with the Cooper pairs (Werthamer, Helfand, Hohenberg-WHH model [96]):

(i) Interaction of the field with the orbital motion of the Cooper pairs (Lorentz force), which results in the orbital limit B_{c2}^{orb}.

(ii) Interaction of the field with the spins of the Cooper pairs (Zeeman effect), which results in the spin-pair breaking, or so-called paramagnetic limit B^P.

Overall, close to T_c the orbital depairing mechanism prevails, while the spin-pair breaking becomes dominant at low temperatures and in large fields.

According to the WHH approach, the orbital limiting upper critical field at 0 K depends simply on both T_c and the slope of $B_{c2}(T)$ at T_c

$$B_{c2}^{orb}(0) = \zeta T_c \left(dB_{c2} / dT\right)\Big|_{Tc}, \tag{3.9}$$

where the pre-factor ζ takes a value of 0.69 and 0.72 for the dirty (*i.e.* the mean free path $l \ll$ coherence length ξ) and clean limit (*i.e.* $l \gg \xi$), respectively [96].

The spin-pair breaking or Pauli limiting upper critical field is determined by a simple equation [97]

$$B^{P}(0) = 1.86 \times T_c . \tag{3.10}$$

In the presence of a magnetic field, the free energy of a SC changes. In particular, upon increasing the magnetic field, the free energy of the superconducting state increases, while in contrast the free energy of the normal state decreases. When these free energies become equal, the resulting upper-critical field can be defined

$$B_{c2}(0) = \frac{B_{c2}^{orb}(0)}{\sqrt{1+\alpha}}, \tag{3.11}$$

here α is a parameter that measure the relative strength of the orbital and spin-pair breaking effect. It is called the Maki parameter [98]

$$\alpha = \sqrt{2} B_{c2}^{orb}(0) / B^{P}(0). \tag{3.12}$$

Therefore, within the WHH formalism, the resulting $B_{c2}(0)$ depends sensitively on the magnitude of α, namely an increase of α would suppress $B_{c2}(0)$.

3.3.1 Slope of the upper critical field $B_{c2}(T)$

In the section above we have discussed the suppression of a SC in a magnetic field and showed a simple method to calculate the upper critical field B_{c2} for $T \to 0$. Furthermore, by studying the temperature dependence of the upper critical field $B_{c2}(T)$, which can be obtained by measuring the temperature dependence of the resistivity around the superconducting transition in fixed magnetic fields, we are able to obtain important information about the superconducting nature. In particular, the microscopic parameters of the superconducting state (*i.e.* the coherence length ξ) and the normal state (*i.e.* the mean free path ℓ) can be retrieved by employing the initial slope of the upper-critical field dB_{c2}/dT at T_c. This method is based on the Ginzburg-Landau theory for type-II superconductors under the assumption of a spherical

Fermi surface. This analysis has been applied to A15 compounds [99] and heavy fermion systems [100]. The slope of $B_{c2}(T)$ can be expressed by

$$B'_{c2} = -\left.\frac{\partial B_{c2}}{\partial T}\right|_{T_c} = R(l)\left(1.18\times10^{35}\frac{\gamma^2 T_c}{S_s^2} + 4480\gamma\rho_0\right) \qquad (3.13)$$

where S_s is the part of the Fermi surface where Cooper pairs are formed; the parameter R(ℓ) varies between R = 1 and R = 1.17 in the dirty and in the clean limit, respectively; γ is the Sommerfeld term in the electronic specific heat (per unit volume). Note that all parameters are in SI units. In the clean limit (ρ_0 small, $l \gg \xi$) the first term dominates B'_{c2}, whereas in the dirty limit (ρ_0 large, $l \ll \xi$) B'_{c2} is mainly determined by the second term. Subsequently, the microscopic parameters (*i.e.* ℓ, ξ) can be extracted

$$l = a\frac{1}{\rho_0 S_s},\ \xi = b\frac{S_s}{\gamma T_c}, \qquad (3.14)$$

where the quantities a and b are given by $1.533 \times 10^6\ \Omega$ and 6.61×10^{-26} J/K, respectively.

3.3.2 Temperature variation of the upper critical field $B_{c2}(T)$

Strictly speaking, the classification of unconventional superconductivity based on the total spin S and orbital angular momentum L is not applicable in case of a material which has strong spin-orbit coupling such as a heavy fermion system [101]. Instead of a classification in singlet (S = 0) and triplet (S = 1) states, the total angular momentum J should be considered. However, it is not expected that the superconducting properties of such strong orbit-coupling systems are significantly different from the ones studied by using rather simple models ignoring spin-orbit coupling. To this purpose, two theoretical models have been chosen: the WHH [96] and polar state models [80], which can be considered representative for all possible pairing states.

The WHH model describes *s*-wave pairing in the clean and dirty limit of superconductors and is expressed by the following equation [96,102]

$$\ln\frac{1}{t} = \sum_{n=-\infty}^{n=+\infty}\left\{\frac{1}{|2n+1|} - \frac{\left(\frac{t}{\sqrt{h}}\right)J(\alpha_\omega)}{1-\left(\frac{\lambda}{\sqrt{h}}\right)J(\alpha_\omega)}\right\}, \qquad (3.15)$$

where $$J(\alpha_\omega) = 2\int_0^\infty d\omega \exp(-\omega^2)\tan^{-1}(\alpha_\omega\omega) \qquad (3.16)$$

and $\alpha_\omega = \dfrac{\sqrt{h}}{\left(|2n+1|t+\lambda\right)}$; $t = \dfrac{T}{T_c}$; $h = 2eB_{c2}\left(\dfrac{v_F}{2\pi T_c}\right)^2$; $\lambda = \dfrac{1}{2\pi T_c \tau} = 0.882\xi / l$; (3.17)

here, t is a reduced temperature with T_c the zero-field SC transition temperature and h is a reduced magnetic field. The reduced mean collision frequency λ is related to the coherence length ξ and the mean free path l and takes the value zero in the clean limit ($\xi \ll l$) and infinity in the dirty limit ($\xi \gg l$). Note that the $h(t)$ curve for the clean limit is above the one for the dirty limit case. In order to get an equal slope at t = 1 for all $h(t)$ curves the normalization frequently used is

$$h^*(t) \equiv \frac{B_{c2}}{\left(-dB_{c2}/dT\right)\big|_{T=T_c}} = \frac{h}{\left(-dh/dt\right)\big|_{t=1}}. \qquad (3.18)$$

The slope dh/dt varies as a function of λ [103,104]

$$\left(-dh/dt\right)\big|_{t=1} = 3\lambda^2\left[\left(\pi^2\lambda/4\right) - \psi\left(1/2 + 1/2\lambda\right) + \psi\left(1/2\right)\right]^{-1}, \qquad (3.19)$$

where ψ is the digamma function, which takes values from 1.426 for $\lambda = 0$ to 1.216λ for large λ [102].

In the second model, *p*-wave SC, using the normal state Green's function for a SC in a magnetic field and taking into account merely the polar state, *i.e.* the equal spin pairing state (ESP: $\left|\uparrow\uparrow\right\rangle$ and $\left|\downarrow\downarrow\right\rangle$), the temperature dependence of the upper-critical field is given by [80]

$$\ln t = \sum_{n=-\infty}^{n=+\infty}\left[s(\omega_n) - \frac{1}{|2n+1|}\right], \qquad (3.20)$$

with $$s(\omega_n) = 2\frac{t}{\sqrt{h}}\int_0^\infty du\, e^{-u^2}\left(\tfrac{3}{2}\{[1+(\alpha_\omega u)^{-2}]\tan^{-1}\alpha_\omega u - (\alpha_\omega u)^{-1}\}\right), \qquad (3.21)$$

$\alpha_w = \dfrac{\sqrt{h}}{t|2n+1|}$, the reduced temperature $t = \dfrac{T}{T_c}$ with T_c a zero-field SC transition temperature and a reduced magnetic field $h = 2eB_{c2}\left(\dfrac{v_F}{2\pi T_c}\right)^2$.

The solutions of equations (3.15) and (3.20) have been applied to the two candidates for TSCs $Cu_xBi_2Se_3$ [84] and YPtBi [67] presented in detail in the chapters 4 and 5, respectively.

References

[1] H. V. Löhneysen, A. Rosch, M. Vojta, and P. Wölfle, Rev. Mod. Phys. **79**, 1015 (2007).

[2] W. Young, Phys. B **91B**, 213 (1977).

[3] M. A. Continentino, G. M. Japiassu, and A. Troper, Phys. Rev. B. Condens. Matt. **39**, 9734 (1989).

[4] M. A. Ruderman and C. Kittel, Phys. Rev. **96**, 99 (1954).

[5] J. Kondo, Prog. Theor. Phys. **32**, 37 (1964).

[6] H. Löhneysen, T. Pietrus, G. Portisch, H. Schlager, A. Schröder, M. Sieck, and T. Trappmann, Phys. Rev. Lett. **72**, 3262 (1994).

[7] P. Gegenwart, F. Kromer, M. Lang, G. Sparn, C. Geibel, and F. Steglich, Phys. Rev. Lett. **82**, 1293 (1999).

[8] O. Trovarelli, C. Geibel, S. Mederle, C. Langhammer, F. M. Grosche, P. Gegenwart, M. Lang, G. Sparn, and F. Steglich, Phys. Rev. Lett. **85**, 626 (2000).

[9] J. Custers, P. Gegenwart, H. Wilhelm, K. Neumaier, Y. Tokiwa, O. Trovarelli, C. Geibel, F. Steglich, C. Pépin, and P. Coleman, Nature **424**, 524 (2003).

[10] S. A. Grigera, R. S. Perry, A. J. Schofield, M. Chiao, S. R. Julian, G. G. Lonzarich, S. I. Ikeda, Y. Maeno, A. J. Millis, and A. P. Mackenzie, Science **294**, 329 (2001).

[11] C. Pfleiderer, G. J. McMullan, S. R. Julian, and G. G. Lonzarich, Phys. Rev. B **55**, 8330 (1997).

[12] M. Uhlarz, C. Pfleiderer, and S. Hayden, Phys. Rev. Lett. **93**, 256404 (2004).

[13] P. Niklowitz, F. Beckers, G. Lonzarich, G. Knebel, B. Salce, J. Thomasson, N. Bernhoeft, D. Braithwaite, and J. Flouquet, Phys. Rev. B **72**, 024424 (2005).

[14] S. Drotziger, C. Pfleiderer, M. Uhlarz, H. Löhneysen, D. Souptel, W. Löser, and G. Behr, Phys. Rev. B **73**, 214413 (2006).

[15] H. V. Löhneysen, A. Schroder, T. Trappmann, and M. Welsch, J. Magn. Magn. Mater. **108**, 45 (1992).

[16] M. Nicklas, M. Brando, G. Knebel, F. Mayr, W. Trinkl, and A. Loidl, Phys. Rev. Lett. **82**, 4268 (1999).

[17] A. de Visser, M. J. Graf, P. Estrela, A. Amato, C. Baines, D. Andreica, F. N. Gygax, and A. Schenck, Phys. Rev. Lett. **85**, 3005 (2000).

[18] D. Sokolov, M. Aronson, W. Gannon, and Z. Fisk, Phys. Rev. Lett. **96**, 116404 (2006).

[19] R. Küchler, P. Gegenwart, J. Custers, O. Stockert, N. Caroca-Canales, C. Geibel, J. G. Sereni, and F. Steglich, Phys. Rev. Lett. **96**, 256403 (2006).

[20] J. Sereni, T. Westerkamp, R. Küchler, N. Caroca-Canales, P. Gegenwart, and C. Geibel, Phys. Rev. B **75**, 024432 (2007).

[21] H. K. Onnes, Leiden Comm. **120b, 122b**, **124c** (1911).

[22] J. Bardeen, L. N. Cooper, and J. R. Schrieffer, Phys. Rev. **108**, 1175 (1957).

[23] D. D. Osheroff, R. C. Richardson, and D. M. Lee, Phys. Rev. Lett. **28**, 885 (1972).

[24] A. J. Leggett, Rev. Mod. Phys. **47**, 331 (1975).

[25] F. Steglich, J. Aarts, C. D. Bredl, W. Lieke, D. Meschede, W. Franz, and H. Schafer, Phys. Rev. Lett. **43**, 1892 (1979).

[26] A. de Visser, J. J. M. Franse, A. Menovsky, and T. T. M. Palstra, J. Phys. F: Met. Phys. **14**, L191 (1984).

[27] W. Schlabitz, J. Baumann, B. Pollit, U. Rauchschwalbe, H. M. Mayer, U. Ahlheim, and C. D. Bredl, Z. Phys. B **62**, 171 (1986).

[28] R. Movshovich, T. Graf, D. Mandrus, J. D. Thompson, J. L. Smith, and Z. Fisk, Phys. Rev. B. Condens. Matt. **53**, 8241 (1996).

[29] N. D. Mathur, F. M. Grosche, S. R. Julian, I. R. Walker, D. M. Freye, R. K. W. Haselwimmer, and G. G. Lonzarich, Nature **394**, 39 (1998).

[30] S. S. Saxena, P. Agarwal, K. Ahilan, F. M. Grosche, R. K. W. Haselwimmer, M. J. Steiner, E. Pugh, I. R. Walker, S. R. Julian, P. Monthoux, G. G. Lonzarich, A. Huxley, I. Sheikin, D. Braithwaite, and J. Flouquet, Nature **406**, 587 (2000).

[31] D. Aoki, A. Huxley, E. Ressouche, D. Braithwaite, J. Flouquet, J. P. Brison, E. Lhotel, and C. Paulsen, Nature **413**, 613 (2001).

[32] J. D. Thompson, R. Movshovich, Z. Fisk, F. Bouquet, N. J. Curro, R. A. Fisher, P. C. Hammel, H. Hegger, M. F. Hundley, M. Jaime, P. G. Pagliuso, C. Petrovic, N. E. Phillips, and J. L. Sarrao, J. Magn. Magn. Mater. **226-230**, 5 (2001).

[33] E. Bauer, G. Hilscher, H. Michor, C. Paul, E. Scheidt, A. Gribanov, Y. Seropegin, H. Noël, M. Sigrist, and P. Rogl, Phys. Rev. Lett. **92**, 027003 (2004).

[34] H. Kamimura, H. Ushio, S. Matsuno, and T. Hamada, *Theory of Copper Oxide Superconductors* (Springer-Verlag, Berlin, 2005).

[35] J. G. Bednorz and K. A. Müller, Z. Phys. B **193**, 189 (1986).

[36] H. Hosono, J. Phys. Soc. Jpn. **77**, 1 (2008).

[37] J. A. Wilson, J. Phys. Condens. Matt. **22**, 203201 (2010).

[38] D. Fay and J. Appel, Phys. Rev. B **22**, 3173 (1980).

[39] A. Huxley, I. Sheikin, E. Ressouche, N. Kernavanois, D. Braithwaite, R. Calemczuk, and J. Flouquet, Phys. Rev. B **63**, 144519 (2001).

[40] F. Hardy, A. Huxley, J. Flouquet, B. Salce, G. Knebel, D. Braithwaite, D. Aoki, M. Uhlarz, and C. Pfleiderer, Phys. B Condens. Matt. **359-361**, 1111 (2005).

[41] T. Akazawa, H. Hidaka, T. Fujiwara, T. C. Kobayashi, E. Yamamoto, Y. Haga, R. Settai, and Y. Onuki, J. Phys. Condens. Matt. **16**, L29 (2004).

[42] A. Dommann, F. Hulliger, T. Siegrist, and P. Fischer, J. Magn. Magn. Mater. **67**, 323 (1987).

[43] S. Sakarya, W. Knafo, N. H. van Dijk, Y. Huang, K. Prokes, C.Meingast, and H. v. Löhneysen, J. Phys. Soc. Jpn. **79**, 014702 (2010).

[44] N. T. Huy, A. Gasparini, D. E. de Nijs, Y. Huang, J. C. P. Klaasse, T. Gortenmulder, A. de Visser, A. Hamann, T. Görlach, and H. v. Löhneysen, Phys. Rev. Lett. **99**, 067006 (2007).

[45] N. T. Huy, D. E. de Nijs, Y. Huang, and A. de Visser, Phys. Rev. Lett. **100**, 077002 (2008).

[46] E. Slooten, T. Naka, A. Gasparini, Y. Huang, and A. de Visser, Phys. Rev. Lett. **103**, 097003 (2009).

[47] V. P. Mineev and T. Champel, Phys. Rev. B **69**, 144521 (2004).

[48] D. Belitz and T. Kirkpatrick, Phys. Rev. B **69**, 184502 (2004).

[49] T. Kirkpatrick and D. Belitz, Phys. Rev. B **67**, 024515 (2003).

[50] R. Roussev and A. Millis, Phys. Rev. B **63**, 140504 (R) (2001).

[51] A. de Visser, N. T. Huy, A. Gasparini, D. E. de Nijs, D. Andreica, C. Baines, and A. Amato, Phys. Rev. Lett. **102**, 167003 (2009).

[52] T. Ohta, Y. Nakai, Y. Ihara, K. Ishida, K. Deguchi, N. K. Sato, and I. Satoh, J. Phys. Soc. Jpn. **77**, 023707 (2008).

[53] T. Ohta, T. Hattori, K. Ishida, Y. Nakai, E. Osaki, K. Deguchi, N. K. Sato, and I. Satoh, J. Phys. Soc. Jpn. **79**, 023707 (2010).

[54] S. Julian, Physics **5**, 17 (2012).

[55] V. P. Mineev and K. V. Samokhin, *Introduction to Unconventional Superconductivity* (Gordon and Breach Science Publishers, Amsterdam, 1999).

[56] V. P. Mineev, in *Adv. Theor. Phys. Landau Meml. Conf.* (2009), p. 68.

[57] V. P. Mineev, Phys. Rev. B **66**, 134504 (2002).

[58] C. L. Kane and E. J. Mele, Phys. Rev. Lett. **95**, 226801 (2005).

[59] M. König, S. Wiedmann, C. Brüne, A. Roth, H. Buhmann, L. W. Molenkamp, X.-L. Qi, and S.-C. Zhang, Science **318**, 766 (2007).

[60] M. Z. Hasan and C. L. Kane, Rev. Mod. Phys. **82**, 3045 (2010).

[61] D. V. Griffiths, *Introduction to Quantum Mechanics* (Prentice Hall, Inc., 1995), p. 333.

[62] D. Hsieh, Y. Xia, L. Wray, D. Qian, A. Pal, J. . H. Dil, J. Osterwalder, F. Meier, G. Bihlmayer, C. . L. Kane, Y. S. Hor, R. J. Cava, and M. Z. Hasan, Science **323**, 919 (2009).

[63] X.-L. Qi and S.-C. Zhang, Phys. Today **63**, 33 (2010).

[64] H. Zhang, C.-X. Liu, X.-L. Qi, X. Dai, Z. Fang, and S.-C. Zhang, Nat. Phys. **5**, 438 (2009).

[65] S. Chadov, X. Qi, J. Kübler, G. H. Fecher, C. Felser, and S. C. Zhang, Nat. Mater. **9**, 541 (2010).

[66] H. Lin, L. A. Wray, Y. Xia, S. Xu, S. Jia, R. J. Cava, A. Bansil, and M. Z. Hasan, Nat. Mater. **9**, 546 (2010).

[67] T. V. Bay, T. Naka, Y. K. Huang, and A. de Visser, Phys. Rev. B **86**, 064515 (2012).

[68] T. V. Bay, M. Jackson, C. Paulsen, C. Baines, A. Amato, T. Orvis, M. C. Aronson, Y. K. Huang, and A. de Visser, Solid State Commun. **183**, 13 (2014).

[69] G. Goll, M. Marz, A. Hamann, T. Tomanic, K. Grube, T. Yoshino, and T. Takabatake, Phys. B Condens. Matt. **403**, 1065 (2008).

[70] A. P. Schnyder, P. M. R. Brydon, and C. Timm, Phys. Rev. B **85**, 024522 (2012).

[71] F. F. Tafti, T. Fujii, A. Juneau-Fecteau, S. René de Cotret, N. Doiron-Leyraud, A. Asamitsu, and L. Taillefer, Phys. Rev. B **87**, 184504 (2013).

[72] Y. Pan, A. M. Nikitin, T. V. Bay, Y. K. Huang, C. Paulsen, B. H. Yan, and A. de Visser, Europhys. Lett. **104**, 27001 (2013).

[73] A. Altland and M. R. Zirnbauer, Phys. Rev. B **55**, 1142 (1997).

[74] M. Sigrist and K. Ueda, Rev. Sci. Instrum. **63**, 239 (1991).

[75] A. Kitaev, AIP Conf. Proc. **1134**, 22 (2009).

[76] A. P. Mackenzie and Y. Maeno, Rev. Mod. Phys. **75**, 657 (2003).

[77] P. W. Anderson and P. Morel, Phys. Rev. **123**, 1911 (1961).

[78] R. Balian and N. R. Werthamer, Phys. Rev. **131**, 1553 (1963).

[79] T. Tsuneto, *Superconductivity and Superfluidity* (Cambridge University Press, New York, 2005).

[80] K. Scharnberg and R. Klemm, Phys. Rev. B **22**, 5233 (1980).

[81] S.-Q. Shen, *Topological Insulators-Dirac Equation in Condensed Matters* (Springer, Berlin, 2012).

[82] X.-L. Qi and S.-C. Zhang, Rev. Mod. Phys. **83**, 1057 (2011).

[83] Y. S. Hor, A. J. Williams, J. G. Checkelsky, P. Roushan, J. Seo, Q. Xu, H. W. Zandbergen, A. Yazdani, N. P. Ong, and R. J. Cava, Phys. Rev. Lett. **104**, 057001 (2010).

[84] T. V. Bay, T. Naka, Y. K. Huang, H. Luigjes, M. S. Golden, and A. de Visser, Phys. Rev. Lett. **108**, 057001 (2012).

[85] N. P. Butch, P. Syers, K. Kirshenbaum, A. P. Hope, and J. Paglione, Phys. Rev. B **84**, 220504 (R) (2011).

[86] S. Sasaki, Z. Ren, A. A. Taskin, K. Segawa, L. Fu, and Y. Ando, Phys. Rev. Lett. **109**, 217004 (2012).

[87] R. Roy, ArXiv:0803.2868v1 (2008).

[88] A. Schnyder, S. Ryu, A. Furusaki, and A. Ludwig, Phys. Rev. B **78**, 195125 (2008).

[89] X.-L. Qi, T. Hughes, S. Raghu, and S.-C. Zhang, Phys. Rev. Lett. **102**, 187001 (2009).

[90] N. Read and D. Green, Phys. Rev. B **61**, 10267 (2000).

[91] D. A. Ivanov, Phys. Rev. Lett. **86**, 268 (2001).

[92] C. Nayak, A. Stern, M. Freedman, and S. Das Sarma, Rev. Mod. Phys. **80**, 1083 (2008).

[93] M. Sato, Phys. Rev. B **81**, 220504(R) (2010).

[94] M. Sato, Phys. Rev. B **79**, 214526 (2009).

[95] L. Fu and E. Berg, Phys. Rev. Lett. **105**, 097001 (2010).

[96] N. R. Werthamer, E. Helfand, and P. C. Hohenberg, Phys. Rev. **147**, 295 (1966).

[97] A. M. Clogston, Phys. Rev. Lett. **9**, 266 (1962).

[98] K. Maki, Phys. Rev. **148**, 362 (1966).

[99] T. P. Orlando, E. J. J. McNiff, S. Foner, and M. R. Beasley, Phys. Rev. B **19**, 4545 (1979).

[100] A. de Visser, PhD Thesis, University of Amsterdam, 1986.

[101] U. Rauchschwalbe, Phys. **147B** 1 (1987).

[102] E. Helfand and N. R. Werthamer, Phys. Rev. **147**, 288 (1966).

[103] L. P. Gor'kov and Z. Eksperim, Sov. Phys. JETP **9**, 1364 (1959).

[104] L. P. Gor'kov and Z. Eksperim, Sov. Phys. JETP **10**, 998 (1960).

Chapter 4 Possible *p*-wave superconductivity in the doped topological insulator $Cu_xBi_2Se_3$

In this chapter, we report magnetic and transport measurements carried out on the candidate topological superconductor (TSC) $Cu_xBi_2Se_3$. The study mainly focuses on the response of superconductivity to a magnetic field and high pressures up to 2.3 GPa. Upon increasing the pressure, superconductivity is smoothly depressed and vanishes at $p_c \sim 6.3$ GPa. At the same time, the metallic behaviour is gradually lost. These features are explained by a simple model for a low electron carrier density superconductor. The analysis of the upper critical field shows that the $B_{c2}(T)$ data collapse onto a universal curve, which clearly differs from the standard curve for a weak coupling, orbital limited, spin-singlet SC. Although an anisotropic spin-singlet state cannot be discarded completely, the absence of Pauli limiting and the similarity of $B_{c2}(T)$ to a polar-state function point to spin-triplet SC. This observation is in accordance with theoretical predictions for TSCs.

(Part of this chapter has been published as T. V. Bay *et al.*, Phys. Rev. Lett. **108**, 057001 (2012))

4.1 Introduction

Topological insulators (TIs) have sparked wide research interest because they offer a new playground for the realization of novel states of quantum matter [1,2]. In 3D TIs the bulk is insulating, but the 2D surface states - protected by a nontrivial Z_2 topology - are conducting due to their topological nature. More interestingly, the concept of TIs can also be applied to superconductors (SCs), due to the direct analogy between topological band theory and superconductivity [3,4]. Topological SCs in 1D, 2D and 3D are predicted to be nontrivial SCs with mixed even and odd-parity Cooper pair states [5,6]. Of major interest in the field of topological SCs is the realization of Majorana zero modes [1,2], that are predicted to exist as protected bound states on the edge of the 1D, 2D or 3D superconductor. Majorana zero modes are of great potential interest for topological quantum computation [1,2]. Recently, signatures of Majorana states have been observed for the first time experimentally in a semiconducting nanowire coupled to an ordinary *s*-wave superconductor [7]. This opens up the possibility to explore and fabricate a new type of quantum computation devices. Topological SCs are rather scarce. The B phase of ^{3}He has recently been identified as an odd-parity time-reversal invariant topological superfluid [8], whereas the correlated metal Sr_2RuO_4 is a time-reversal symmetry breaking chiral 2D *p*-wave SC [3]. Other candidate topological superconductors can be found among the half-Heusler equiatomic platinum bismuthides LaPtBi, YPtBi, LuPtBi [9–12] and the doped semiconductor $Sn_{1-x}In_xTe$ [13].

In 2010, Hor and co-workers initiated a new route to fabricate topological superconductors, namely, by reacting the 3D TIs Bi_2Se_3 and Bi_2Te_3 with Cu or Pd [14,15]. By intercalating Cu^{1+} into the van der Waals gaps between the Bi_2Se_3 quintuple layers, SC occurs with a transition temperature T_c = 3.8 K in $Cu_xBi_2Se_3$ for $0.12 \leq x \leq 0.15$. However, the reported SC shielding fractions were rather small and the resistance never attained a zero value below T_c, which casted some doubt on the bulk nature of SC. As regards $Cu_xBi_2Se_3$, this concern was taken away by Kriener et al. [16,17], who showed that Bi_2Se_3 single crystals electrochemically intercalated by Cu have a SC volume fraction of about 60% (for x = 0.29) as evidenced by the significant jump in the electronic specific heat at T_c. SC was found to be robust and present for $0.1 \leq x \leq 0.6$. Photoemission experiments conducted to study the bulk and surface electron dynamics reveal that the topological character is preserved in $Cu_xBi_2Se_3$ [18] as demonstrated in Fig. 4.1. Based on the topological invariants of the Fermi surface, $Cu_xBi_2Se_3$ is expected to be a time-reversal invariant, fully gapped, odd parity, topological SC [5,6]. A recent study of the Cooper pairing symmetry within a two-orbital model led to the proposal that such a state can be favored by strong-spin orbit coupling [19]. Indeed several

experiments have revealed properties in line with topological SC. The magnetization in the SC state has an unusual field variation and shows curious relaxation phenomena, pointing to a spin triplet vortex phase [20]. Point contact measurements reveal a zero-bias conductance peak in the spectra, which possibly provides evidence for Majorana zero modes [21]. These signatures of topological SC make the experimental determination of the basic SC behavior of $Cu_xBi_2Se_3$ highly relevant.

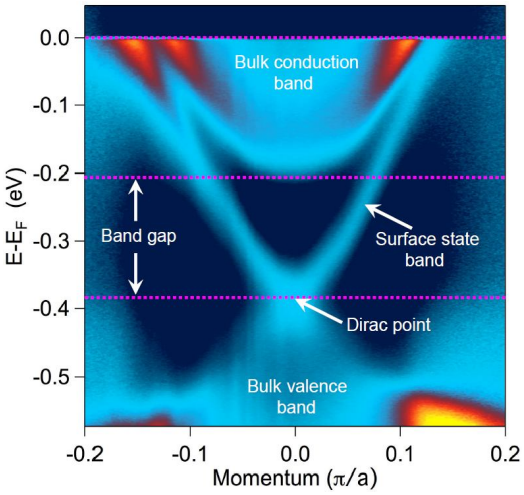

Figure 4.1 Topological surface state of $Cu_xBi_2Se_3$ from ARPES measurements at 4 K. The Dirac point is located at ~ -0.38 eV. The data are kindly provided by Dr. E. van Heumen (QEM group, private communication).

4.2 Sample preparation

A series of single crystalline samples $Cu_xBi_2Se_3$ was prepared at the WZI by Dr. Y.K. Huang with x ranging from 0.12 to 0.3. The high purity elements Cu, Bi, and Se were molten together at 850 °C in quartz tubes sealed under high vacuum. Subsequently, the tubes were slowly cooled till 500-600 °C in order to grow the crystals. After growth the crystals were annealed for 60-100 hours.

More than thirty samples were measured in a standard bath cryostat to check for SC. All samples showed metallic behavior. Many samples revealed some traces of SC below 2-3 K. However, only very few samples showed zero resistance below the superconducting transition temperature T_c = 3.8 K. It appears, therefore, that SC is very fragile and sensitively depends on the sample preparation process. It was also tried to synthesize the material with the electro-chemical method, by which ideally Cu^{1+} acts as a donor, but in contrast to Refs. [16,17] a full SC transition (R = 0) was never obtained by this route. In the remainder of

this chapter we focus on the best samples fabricated by the melting method with a nominal Cu content x ~ 0.3, a nominal Bi content ~ 2.1, and rapid quenched after annealing.

$Cu_xBi_2Se_3$ belongs to the space group $R\bar{3}m$ and possesses a layered crystal structure with lattice parameters a = 4.138 Å and c = 28.736 Å as shown in Fig. 4.2. The pristine compound Bi_2Se_3 is constructed from double layers of $BiSe_6$ octahedra resulting in a Se-Bi-Se-Bi-Se five layer sandwich. The dopant Cu atoms either substitute at Bi sites or intercalate at the octahedrally coordinated (0, 0, 1/2) sites (Wyckoff notation 3b site) in the Van der Waals gaps between the Bi_2Se_3 quintuple layers. SC is associated with intercalation rather than substitution [14].

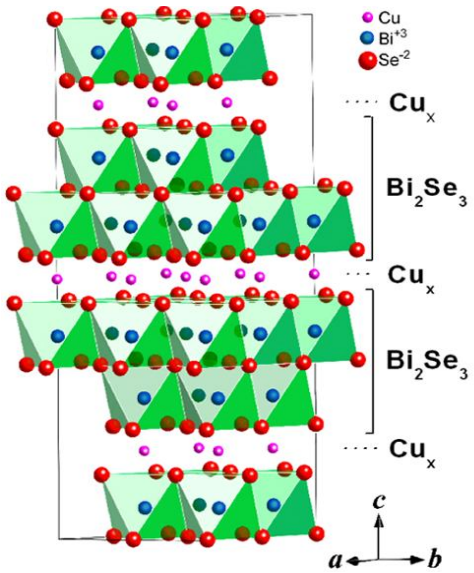

Figure 4.2 Layered structure of $Cu_xBi_2Se_3$. The small pinkish dots depict copper atoms intercalated in the Van der Waals gaps between the quintuple layers. Picture taken from Ref. [14].

4.3 Ac-susceptibility

In order to determine the superconducting shielding fraction of our samples, ac-susceptibility (χ_{ac}) measurements have been performed at the Institute Néel by Dr. C. Paulsen in a dedicated SQUID magnetometer. Fig. 4.3 shows the low-temperature susceptibility data of two $Cu_{0.3}Bi_{2.1}Se_3$ samples (sample S$\parallel$, m = 0.5 g, sample S$\perp$, m = 0.25 g). The SC shielding fractions amount to 13 % and 16 %, respectively. The data have been corrected for demagnetization effects. In both samples the SC transition sets in at $T_{c\text{-}onset}$ = 3.1 K. The signals are rather sluggish upon lowering temperature being indicative of sample inhomogeneities.

These SC volume fractions are lower than those (up to 60 %) reported in Ref. 18 for samples prepared by electro-chemical intercalation.

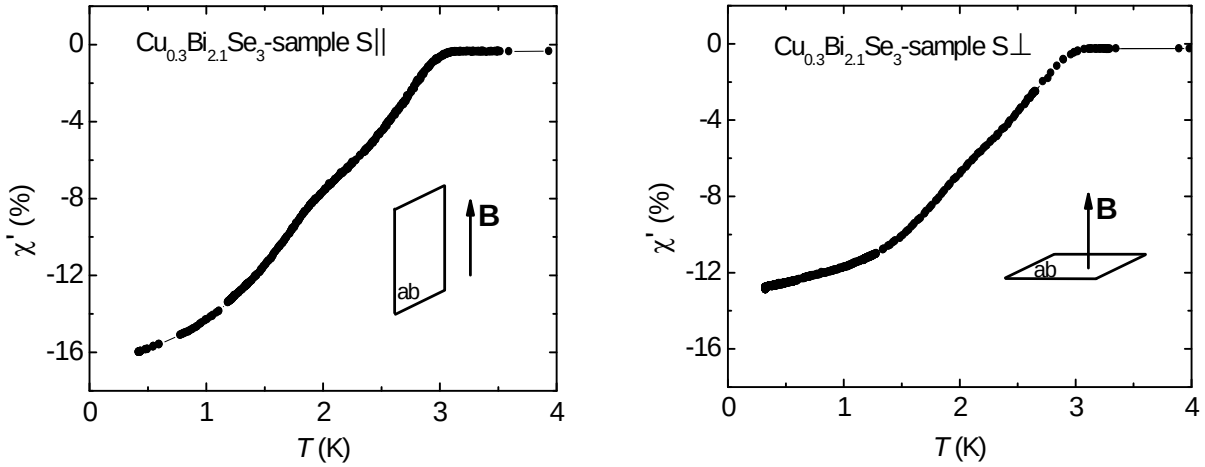

Figure 4.3 Temperature dependence of the real part of the ac-susceptibility of two plate-like $Cu_{0.3}Bi_{2.1}Se_3$ crystals. Left panel: sample S|| with the driving field in the *ab*-plane. Right panel: sample S⊥ with the driving field perpendicular to the *ab*-plane. The driving frequency is 2.1 Hz. The amplitude of the driving field is 0.25 Oe and 0.5 Oe, respectively. The driving fields are well below H_{c1} = 5 Oe, Ref. 22.

4.4 Electrical resistivity

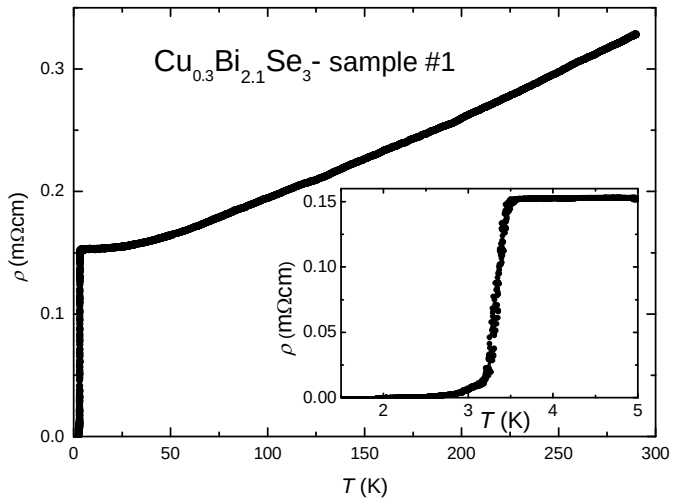

Figure 4.4 Temperature dependence of the resistivity of $Cu_{0.3}Bi_{2.1}Se_3$ (sample #1) at ambient pressure**.** Inset: superconducting transition.

Many batches of $Cu_xBi_2Se_3$ were initially tested after growth using a He bath cryostat in which the temperature can be lowered down to 1.5 K by directly decreasing the vapour pressure of liquid helium. Fig. 4.4 shows a representative resistivity curve in the temperature

range from room temperature till below T_c at ambient pressure. The sample is metallic in the whole temperature range. The inset presents the resistivity around the superconducting transition. SC sets in at T_c = 3.4 K with initially a rather sharp drop. There is a tail below 3.2 K and the resistance reaches zero for T < 2.8 K. Overall, the $T_{c\text{-}onset}$ measured by transport is in agreement with the transition in χ_{ac}. The tail is presumably related to sample inhomogeneities as inferred from the ac-susceptibility data as well, see Fig. 4.3. Nevertheless, the data are in good agreement with previous reports [14,16].

4.5 Upper critical field B_{c2} at ambient pressure

Fig 4.5 shows the superconducting transition of a $Cu_{0.3}Bi_2Se_3$ single crystal at ambient pressure in magnetic fields applied in the hexagonal plane ($B \parallel ab$) and out of plane ($B \parallel c$). In field some additional structures appear on the curves, and these become more pronounced with increasing field. However, in essence, SC is gradually suppressed. We have determined the upper critical field B_{c2}, $B \parallel ab$ (B_{c2}^{ab}) and $B \parallel c$ (B_{c2}^{c}), by means of the midpoints of the major steps in the superconducting transition and the results are plotted in Fig 4.6.

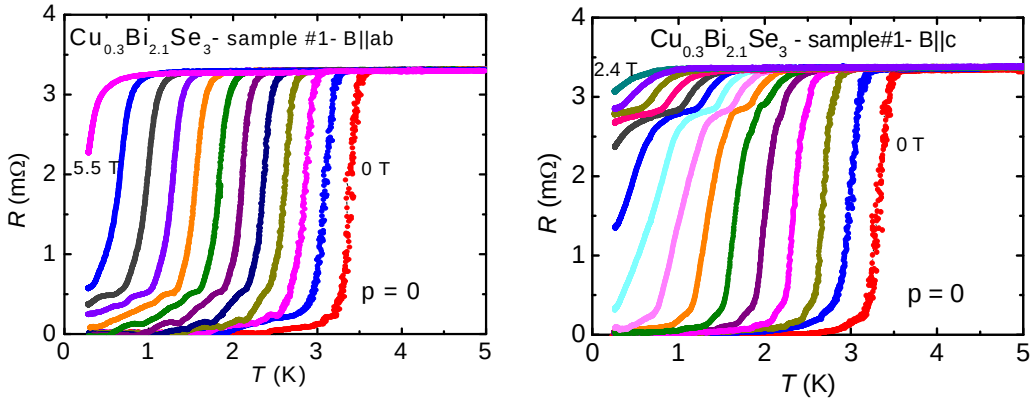

Figure 4.5 Temperature dependence of the resistance of a $Cu_{0.3}Bi_{2.1}Se_3$ single crystal in fixed magnetic fields. Left panel: applied field parallel to the *ab*-plane, from right to left: 0 to 5.5 T in steps of 0.5 T. Right panel: field parallel to the *c*-axis, from right to left: 0 to 2.4 T in steps of 0.2 T.

For a layered compound, the upper-critical field shows a moderate anisotropy with $B_{c2}^{ab}(T \to 0) = 5.6$ T and $B_{c2}^{c}(T \to 0) = 1.9$ T. The anisotropy parameter is $\gamma^{an} = \frac{B_{c2}^{ab}}{B_{c2}^{c}} = 2.9$.

Other microscopic parameters are calculated as follows. Using the relations

$$B_{c2}^{c} = \frac{\Phi_0}{2\pi\xi_{ab}^2} \text{ and } B_{c2}^{ab} = \frac{\Phi_0}{2\pi\xi_{ab}\xi_c}, \tag{4.1}$$

where Φ_0 is the flux quantum, we obtain the SC coherence lengths $\xi_{ab} = 13$ nm and $\xi_c = 4$ nm. These values are in good agreement with those reported previously [14,16].

Furthermore, it is important to distinguish whether our samples are in the clean or dirty limit, or in between. This is relevant because a sufficiently clean sample, i.e. with an electron mean free path ℓ larger than ξ, is a prerequisite for SC triplet pairing [22]. An estimate for ℓ can be obtained from the relation

$$l = \frac{\hbar k_F}{\rho_0 n e^2}, \tag{4.2}$$

which assumes a spherical Fermi surface $S_F = 4\pi k_F^2$ with Fermi wave vector

$$k_F = \left(3\pi^2 n\right)^{1/3} \tag{4.3}$$

Here n is the carrier density and ρ_0 is the residual resistivity. Using the experimental value for n derived from Hall measurements $n = 1.2 \text{ x } 10^{26}$ m^{-3} and $\rho_0 = 1.5 \text{ x } 10^{-6}$ Ωm we obtain $k_F = 1.5 \text{ x } 10^9 m^{-1}$ and $\ell = 34$ nm, which ensures $l > \xi$.

A more detailed analysis can be made by employing the slope of the upper-critical field dB_{c2}/dT at T_c [23]. In the dirty limit case the initial slope is given by

$$\left|\frac{dB_{c2}}{dT}\right|_{T_c} = 4480\gamma\rho_0, \tag{4.4}$$

where γ is the Sommerfeld coefficient of the electronic specific heat per unit volume. With γ = 22.9 J/m^{3}K^2 [16] we calculate $|dB_{c2}/dT|_{Tc}$ = 0.15 T/K. This value is much lower than the measured values 2.0 T/K (B // ab) and 0.6 T/K (B // c), which confirms our samples are not in the dirty limit. By adding the clean limit term

$$\left|\frac{dB_{c2}}{dT}\right|_{T_c} = 1.38\times10^{35}\gamma^2 T_c / S_F^2 \tag{4.5}$$

in the model [20], estimates for l and ξ can be calculated from the experimental values of $|dB_{c2}/dT|_{Tc}$. For B // ab(c) we obtain $l \sim$ 90(45) nm and $\xi \sim$ 9(19) nm. Note that in this analysis we used the normal-state γ value as an input parameter. If we take into account that not the whole bulk of the sample becomes superconducting (due to the incomplete shielding fraction), a reduced γ_s value [16] should be used. This will affect the absolute values of the deduced parameters, but not our conclusion that $l > \xi$. Consequently, we argue our samples are sufficiently pure to allow for odd-parity SC.

In Fig. 4.6, we compare the experimental data of $B_{c2}(T)$ with the model calculations for an *s*-wave spin singlet superconductor and a polar *p*-wave state. Obviously, the polar *p*-wave state model provides a better match. This will be further discussed in section 4.7.

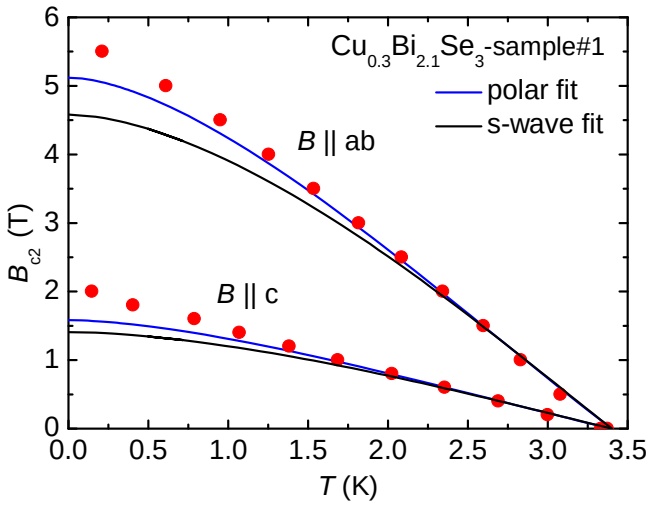

Figure 4.6 Temperature variation of the upper critical field, $B_{c2}(T)$, of $Cu_{0.3}Bi_{2.1}Se_3$ (sample #1) for $B \parallel ab$ and $B \parallel c$. The blue and black solid lines indicate the model functions for an *s*-wave and polar-state superconductor, respectively (see text).

4.6 Superconducting transition under pressure

For two samples the pressure variation of $\rho(T)$ was measured under pressure up to 2.3 GPa. The samples were mounted in the pressure cell such that the field could be applied parallel (sample #11) and perpendicular (sample #12) to the *ab*-plane. Here, we first describe the results at zero applied magnetic field.

In Fig. 4.7 we show the pressure dependence of $\rho(T)$ around T_c for sample #11. The superconducting transition becomes sharper under pressure. The overall good sample quality is attested to by the relatively small width of ΔT_c (as measured between 10% and 90% of ρ(4 K)), which ranges from 0.25 K at p = 0 to 0.06 K at p = 2.31 GPa. Nevertheless, a tail towards low temperatures associated with ~ 10% of the resistance path is present. For sample #12 the resistance does not reach R = 0, but remains finite at the level of 10% of ρ(4 K), a value comparable to that reported previously by the Princeton group [14].

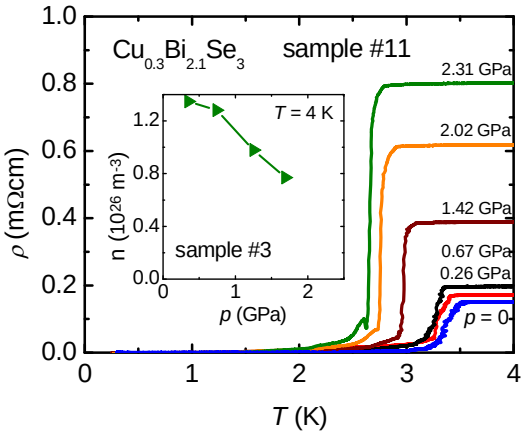

Figure 4.7 Resistivity of $Cu_{0.3}Bi_{2.1}Se_3$ (sample #11) as a function of pressure around T_c at pressures up to 2.31 GPa as indicated. Inset: Pressure dependence of the electron carrier density at T = 4 K for sample #3.

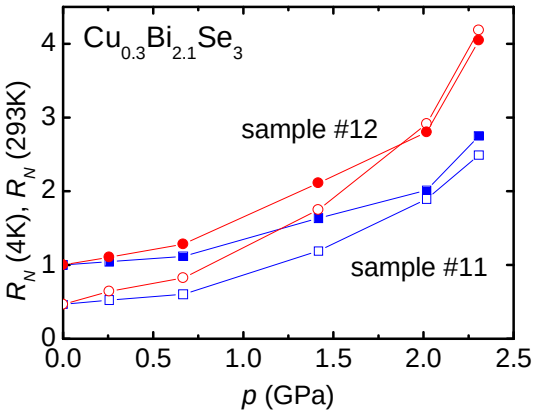

Figure 4.8 Resistance R_N normalized by the room temperature value R(239 K, p = 0) as a function of pressure of $Cu_{0.3}Bi_{2.1}Se_3$ sample #11 (squares) and sample #12 (circles). R_N(4K) and R_N(293K) are given by open and closed symbols, respectively.

Under pressure, the metallic behaviour is gradually lost as indicated by the large increase of the normal state resistivity at 4 K reported in Fig. 4.7. In Fig 4.8, we have traced the pressure variation of R(4 K) and R(293 K) for two samples after normalizing to the ambient pressure room temperature value R(239 K, p = 0). R_N(4 K) and R_N(293 K) both increase, approach each other and even cross for sample #12. This analysis also shows the metallic behaviour to be lost under pressure.

The variation of T_c with pressure determined by the midpoint of the transition is shown in Fig. 4.9 for sample #11 and #12. The results almost coicide for both samples. The solid line (see caption) suggests that T_c might be suppressed at a critical pressure p_c as high as ~ 6.3 GPa.

The depression of T_c can be understood qualitatively in a simple model for a low carrier density superconductor where

$$T_c \sim \Theta_D \exp\frac{-1}{N(0)V_0}, \qquad (4.6)$$

with Θ_D the Debye temperature, $N(0) \sim m^* n^{1/3}$ the density of state (with m^* the effective mass), and V_0 the effective interaction parameter [24]. The increase of R(4K) under pressure by a factor > 5 indicates a decrease of the carrier concentration n, which in turn leads to a reduction of N(0) and T_c. The reduction of n is also apparent in the temperature variation $R(T)$ which gradually loses its metallic behavior as mentioned previously (see Fig. 4.8).

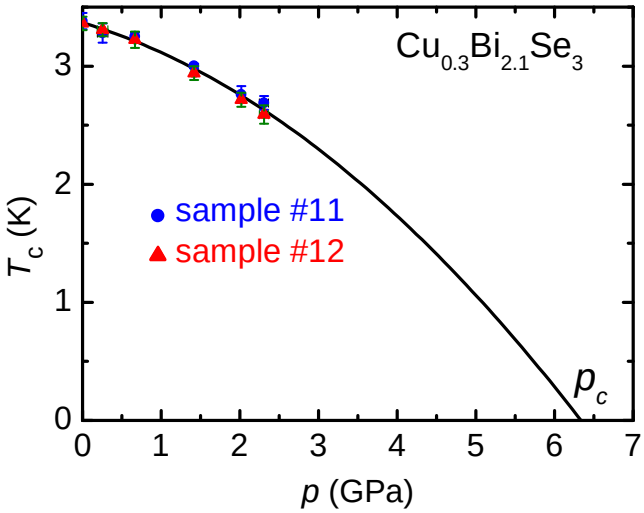

Figure 4.9 Superconducting transition temperature as a function of pressure for $Cu_{0.3}Bi_{2.1}Se_3$ sample #11 (circles) and sample #12 (triangles) as indicated. The solid line depicts a polynomial fit with linear and quadratic terms which serves to extrapolate the data. A critical pressure p_c = 6.3 GPa is estimated.

Hall effect experiments on a third sample (#3) confirm the gradual loss of metallic behaviour inferred from the resistivity data. The result presented in the inset of Fig 4.7 at 4 K shows that the electron carrier density $n \simeq 1.2 \times 10^{26}\,\mathrm{m}^{-3}$ at p = 0 (we referred earlier from the resistivity data) drops to $n \simeq 0.7 \times 10^{26}\,\mathrm{m}^{-3}$ at p = 1.7 GPa. In addition, the Hall measurements also indicate that the increase of n with pressure is temperature independent.

4.7 Upper critical field B_{c2} under pressure

To further elucidate the nature of superconductivity in the candidate topological superconductor $Cu_xBi_2Se_3$, we now focus on its magnetic field response under pressure. Figs. 4.10 and 4.11 show the temperature dependence of the resistance under pressure in two particular cases: the applied field parallel (sample #11) and perpendicular (sample #12) to the *ab*-plane.

For the pressure experiment a large sized sample (sample #1) that was first measured at ambient pressure was cut into several smaller pieces. Subsequently, two of these smaller samples were mounted in the pressure cell. As mentioned previously (section 4.2), sample homogeneity is one of the central issues for experimental work at the current stage of research. These inhomogeneities show up as structures and steps in both samples in the $R(T)$ curves around the SC transition. In the following, however, we argue they do not effect the physical picture.

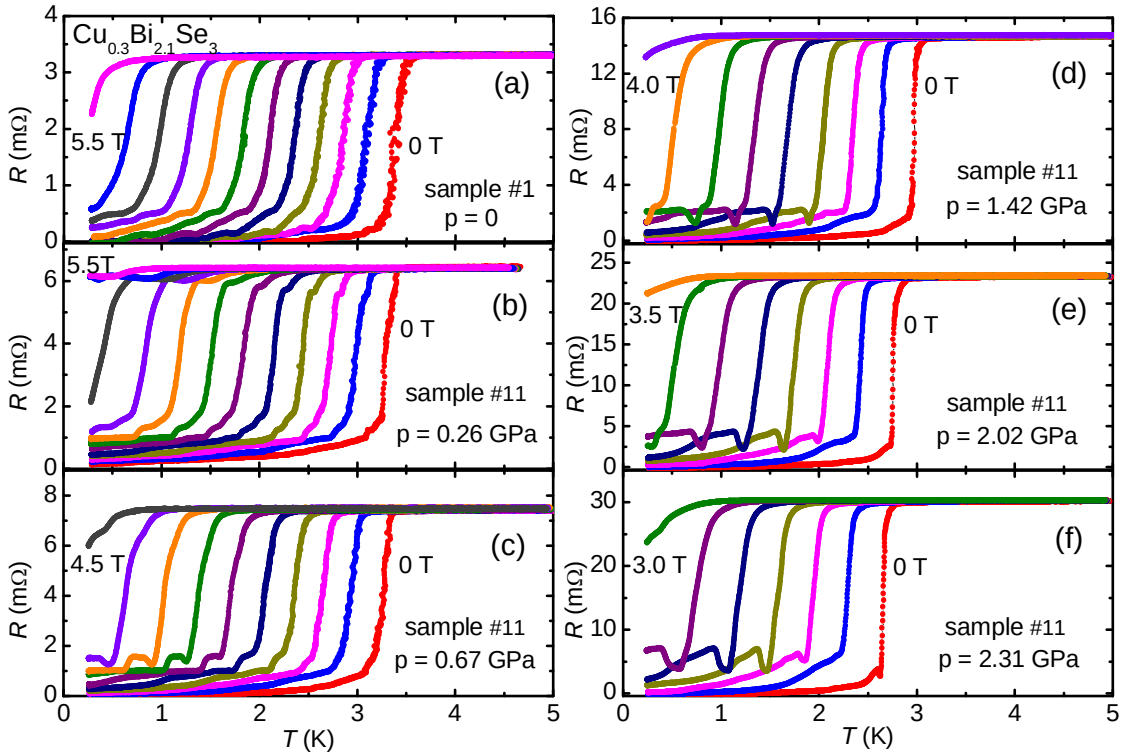

Figure 4.10 Temperature variation of the resistance of $Cu_{0.3}Bi_{2.1}Se_3$ measured in fixed magnetic fields, B || *ab*-plane, ranging from 0 T (right) to 5.5 T (left) in steps of 0.5 T. (a) Sample #1 at ambient pressure; (b)-(f) sample #11 at pressures of 0.26, 0.67, 1.42, 2.02 and 2.31 GPa.

In order to analyze the upper-critical field $B_{c2}(T)$, it is essential to determine accurately and systematically the superconducting transition temperature at a given magnetic field. However, there is in principle no standard routine to implement this, and the problem becomes more intricate when the transitions exhibit structure. To this purpose we use the first order derivative of the $R(T)$ curves, which allows us to locate the main $R(T)$ drops in the transitions as quantitatively illustrated in Fig. 4.12 for a particular case (see caption).

By applying this method, we obtain $B_{c2}(T)$ data for the whole pressure range for the two sample configurations, which are presented in Fig. 4.13. Under pressure $B_{c2}(T)$ gradually decreases and the anisotropy parameter reduces from $\gamma^{an} = 2.9$ at p = 0 to 2.1 at the highest pressure p = 2.31 GPa. The coherence lengths increase to $\xi_{ab} = 15\,\text{nm}$ and $\xi_c = 7\,\text{nm}$. As mentioned above, the increase of ρ_0 and the gradual loss of metallic behavior under pressure can for the major part be attributed mostly to a corresponding decrease of n, which tells us the ratio $l > \xi$ is satisfied in the entire pressure range.

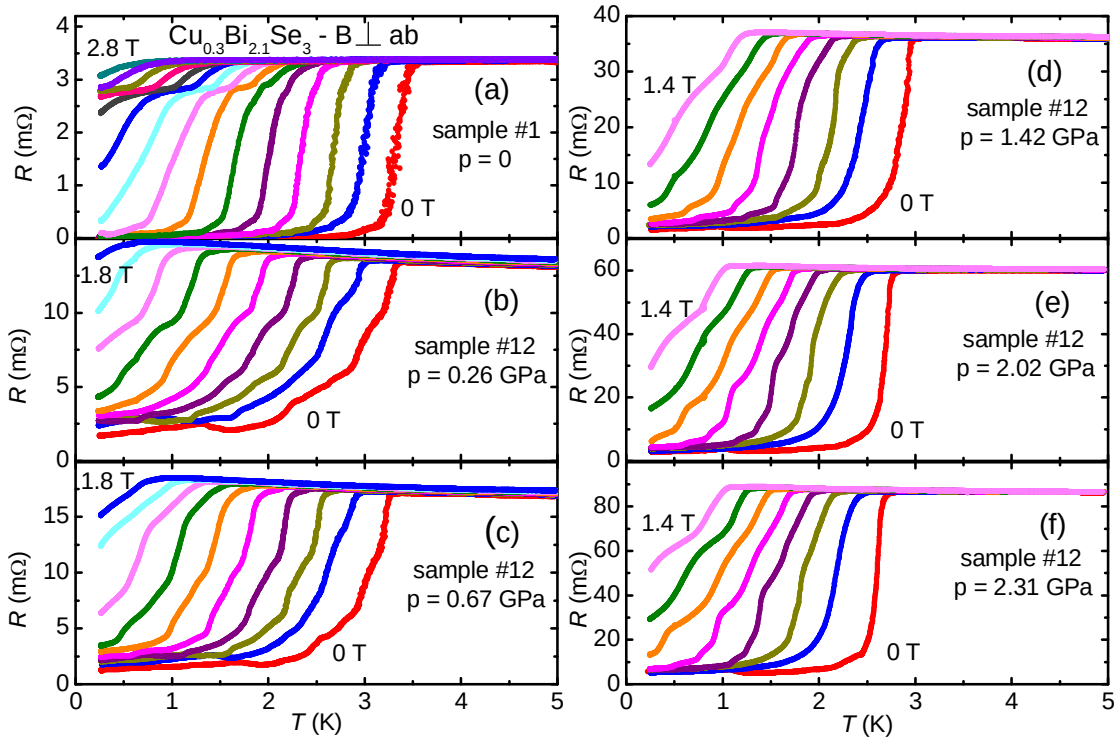

Figure 4.11 Temperature variation of the resistance of $Cu_{0.3}Bi_{2.1}Se_3$ measured in fixed magnetic fields, $B \perp ab$-plane, ranging from 0 T (right) to 2.8 T (left) in steps of 0.2 T. (a) Sample #1 at ambient pressure; (b)-(f) sample #12 at pressures of 0.26, 0.67, 1.42, 2.02 and 2.31GPa.

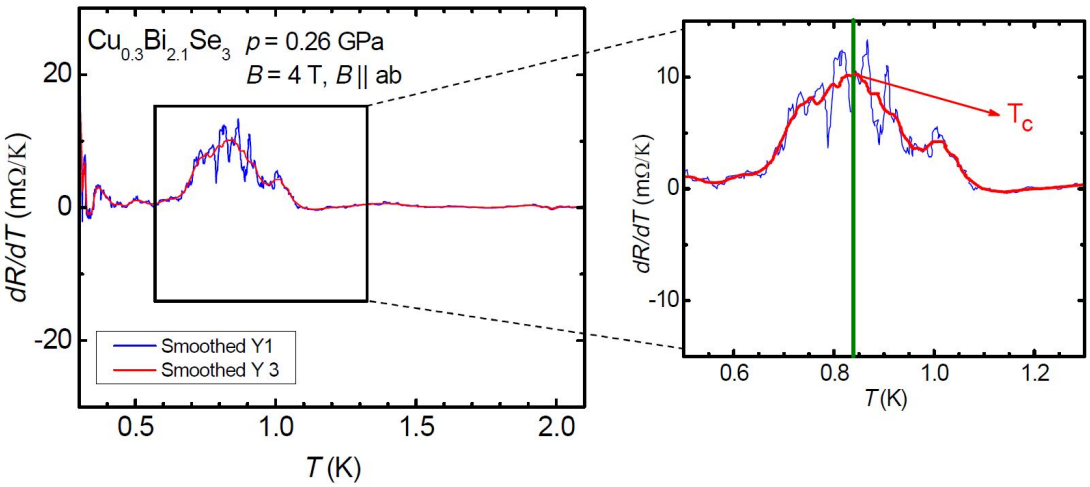

Figure 4.12 The first order derivative of the resistance versus temperature. For this case $B \parallel ab$, p = 0.26 GPa and B = 4 T. The dR/dT is then smoothed to locate T_c.

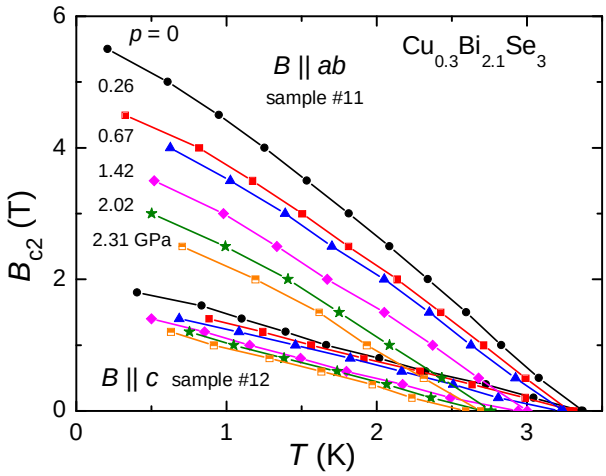

Figure 4.13 Temperature variation of the upper-critical field $B_{c2}(T)$ for $B \parallel ab$ and $B \parallel c$ at pressures of 0, 0.26, 0.67, 1.42, 2.02, and 2.31 GPa (from top to bottom).

The functional behavior of B_{c2} does not change with pressure, as demonstrated in Fig. 4.14. All the $B_{c2}(T)$ curves collapse on one single universal function $b^*(t)$, with

$$b^* = \left(B_{c2} / T_c\right) / \left|dB_{c2} / dT\right|_{Tc} \tag{4.7}$$

and $t = T/T_c$ the reduced temperature. This holds for $B \parallel ab$, as well as for $B \parallel c$. In order to analyze the data further we have traced in Fig. 4.14 also the universal curve for a clean spin-singlet SC with the orbital limited upper-critical field

$$B_{c2}^{orb}(0) = 0.72 \times T_c \left|dB_{c2} / dT\right|_{Tc} \tag{4.8}$$

[Werthamer-Helfand-Hohenberg (WHH) model [25]], noting that for a dirty limit system the prefactor would reduce to 0.69. Clearly, the data deviate from the standard spin-singlet behavior. Next, we consider the suppression of the spin-singlet state by paramagnetic limiting [26,27]. The Pauli limiting field in the case of weak coupling is given by $B^P(0) = 1.86 \times T_c$. For $Cu_{0.3}Bi_{2.1}Se_3$ $B^P(0) = 6.2$ T at ambient pressure. When both orbital and spin limiting fields are present, the resulting critical field is

$$B_{c2}(0) = \frac{B_{c2}^{orb}(0)}{\sqrt{1+\alpha^2}}, \tag{4.9}$$

with the Maki parameter [25,28]

$$\alpha = \frac{\sqrt{2} B_{c2}^{orb}(0)}{B^P(0)} \tag{4.10}$$

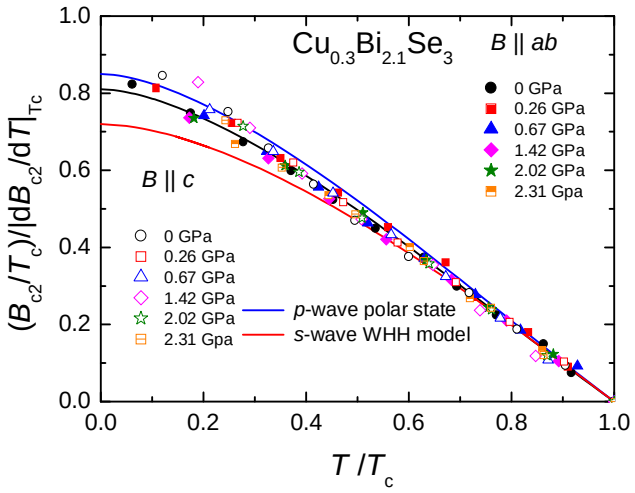

Figure 4.14 Upper-critical field $B_{c2}(T)$ divided by T_c and normalized by the initial slope $|dB_{c2}/dT|_{Tc}$ as a function of the reduced temperature T/T_c at pressures of 0, 0.26, 0.67, 1.42, 2.02 and 2.31 GPa for $B \parallel ab$ (closed symbols) and $B \parallel c$ (open symbols). The lower and upper lines present model calculations for an *s*- and *p*-wave superconductor. The middle curve matches the data closely and depicts the polar-state model function scaled by a factor 0.95, which would result from a 5% larger initial slope in the model.

For $B \parallel ab(c)$ we calculate α = 1.1(0.34) and $B_{c2}(0)$ = 3.3(1.4) T. These values of $B_{c2}(0)$ are much lower than the experimental values (see Fig. 4.13) and we conclude the effect of Pauli limiting is absent. In general, by including the effect of paramagnetic limiting the overall critical field is reduced to below the universal spin singlet values [23,25]. Thus, the fact that our B_{c2} data are well above even these universal values points to an absence of Pauli limiting, and is a strong argument in favor of spin triplet SC. The Pauli paramagnetic effect suppresses spin-singlet Cooper pairing, as well as the $L_z = 0$ triplet component $\left(|\uparrow\downarrow\rangle + |\downarrow\uparrow\rangle\right)/\sqrt{2}$, while the equal-spin pairing (ESP) states $|\uparrow\uparrow\rangle$ and $|\downarrow\downarrow\rangle$ with L_z = 1 and L_z = -1 respectively, are stabilized in a high magnetic field. Exemplary SCs where Pauli limiting is absent are the spin-triplet SC ferromagnets URhGe [29] and UCoGe [30].

Next we consider the role of anisotropy of the crystal structure. Calculations show that for layered SCs, for *B* parallel to the layers, B_{c2}^{orb} is reduced and the critical field can exceed the values of the WHH model [31]. $Cu_xBi_2Se_3$ is a layered compound [14] with a moderate anisotropy $\gamma^{an} = 2.9$. In this respect it is interesting to compare to other layered SCs, like alkali intercalates of the semiconductor MoS_2 [32], which have γ^{an} values in the range 3.2-6.7. A striking experimental property of these layered SCs is a pronounced upward curvature of $B_{c2}(T)$ for *B* parallel to the layers for $T < T_c$ due to dimensional crossover, which

is also a salient feature of model calculations [31]. However, an upward curvature is not observed in $Cu_xBi_2Se_3$. In more detailed theoretical work the anisotropy of both the Fermi surface and the superconducting pairing interaction has been incorporated [33]. Under certain conditions this can give rise to deviations above the WHH curve as seen in Fig. 4.14. The bulk conduction band Fermi surface of the parent material *n*-type Bi_2Se_3 is an ellipsoid of revolution along the k_c axis with trigonal warping [34]. $Cu_xBi_2Se_3$ has a similarly shaped Fermi surface observed by Shubnikov-de Haas oscillations and ARPES measurements [35], The Fermi surface anisotropy would result in a different functional dependence of $B_{c2}(T)$ for $B \parallel ab$ and $B \parallel c$. On the qualitative level this is at variance with the universal $b^*(t)$ reported in Fig. 4.14.

Finally, we compare the $B_{c2}(T)$ data with upper-critical field calculations for a *p*-wave SC [36]. For an isotropic *p*-wave interaction the polar state (which applies for a linear combination of both ESP components) has the highest critical field for all directions of the magnetic field. In Fig. 4.14 we compare the $B_{c2}(T)$ data with the polar-state model function. This time the data lie below the model curve, but most importantly, the temperature variation itself is in agreement with the model, as illustrated by the solid black curve in Fig. 4.14. We have also considered a scaled WHH curve, but it fits the data much less well: increasing $b^*(0)$ by, e.g. 10% to match the experimental value, results in an overall curvature of $b^*(t)$ for a scaled WHH trace in disaccord with the data.

4.8 Discussion

In general, topological SC has been theoretically predicted to involve all three components of the triplet state with a full gap in zero field [5,6]. Recently, scanning tunneling microscopy/spectroscopy (STM/S) [37] and Andreev reflection spectroscopy [38] measurements have been performed on $Cu_xBi_2Se_3$ samples with a low Cu content to determine the superconducting gap structure as well as the nature of the superconducting state. In this context, the simplest way to explain the observed zero field *U*-shaped scanning tunneling spectroscopy data would be based on standard BCS *s*-wave pairing for Cu intercalated Bi_2Se_3 [37]. In the reflection spectroscopy measurements, zero bias conduction peaks (ZBCPs) possibly indicative of Majorana modes can be obtained or not depending on the strength of the normal metal/superconductor barrier [38]. The Fermi surface shape evolution upon doping Bi_2Se_3 with Cu obtained from Shubnikov-de Haas oscillations and ARPES shows that upon increasing the carrier concentration the Fermi surface changes from a closed ellipsoid to an open cylinder-type; and most importantly, the Fermi surface encloses

two (or an even number) TRS points (Γ and Z), which is at variance with the theoretical prediction of the criteria for the realization of TSC in this material [19,35]. However, point contact experiments signify the existence of ZBCPs even at very low temperature (0.35 K) and in magnetic fields up to 0.45 T, which provides a strong evidence for the emergence of unconventional Andreev bound states associated with Majorana zero modes [21]. On the other hand, a fully gapped tunneling spectrum such as that seen in STS can also be understood by a more complex pairing at the surface [39]. Within this theoretical consideration, if the superconducting state is induced by a trivial *s*-wave pairing, the pair potential at the surface would result in an additional coherence peak within the induced energy gap in the spectroscopy. But such an extra peak was not observed in the STS spectra nor in the Andreev reflection spectroscopy [37,38]. Furthermore, model calculations indicate triplet pairing is possibly favorable for the $L_z = 0$ component [19]. In an applied magnetic field we expect a phase transition or crossover to a polar state to occur. It is at present not possible to explain all the experimental data in a single interpretative framework, as regards the superconducting pairing in $Cu_xBi_2Se_3$. Clearly, more theoretical work is desirable on topological superconductors in a magnetic field to settle the issue of B_{c2}, and thus helps unravel the pairing mechanism of the superconducting phase.

4.9 Conclusion

By means of transport measurements we have investigated the pressure variation of the superconducting phase induced by Cu intercalation of the topological insulator Bi_2Se_3. Superconductivity is a robust phenomenon in these samples and by extrapolating $T_c(p)$, superconductivity appears to vanish at the high critical pressure of $p_c = 6.3$ GPa. The metallic behavior of the system is gradually lost under pressure. The upper-critical field B_{c2} data under pressure collapse onto a single universal curve, which differs from the standard curve of a weak coupling, orbital-limited, spin-singlet superconductor. The absence of Pauli limiting, the sufficiently large mean free path, and the polar-state temperature variation of the B_{c2} data, point to $Cu_xBi_2Se_3$ as a *p*-wave superconductor. In spite of some doubt as regards the unconventional superconducting nature in this material from recent tunneling experiments, our observations are in line with theoretical proposals that $Cu_xBi_2Se_3$ is a promising candidate topological superconductor. More experimental work to unravel the superconducting state, by *e.g.* μSR or NMR experiments, is desired to further settle these issues.

References

[1] M. Z. Hasan and C. L. Kane, Rev. Mod. Phys. **82**, 3045 (2010).

[2] X.-L. Qi and S.-C. Zhang, Rev. Mod. Phys. **83**, 1057 (2011).

[3] A. Kitaev, AIP Conf. Proc. **1134**, 22 (2009).

[4] A. P. Schnyder, S. Ryu, A. Furusaki, and A. W. W. Ludwig, AIP Conf. Proc. **1134**, 10 (2009).

[5] M. Sato, Phys. Rev. B **79**, 214526 (2009).

[6] M. Sato, Phys. Rev. B **81**, 220504(R) (2010).

[7] V. Mourik, K. Zuo, S. M. Frolov, S. R. Plissard, E. P. A. M. Bakkers, and L. P. Kouwenhoven, Science **336**, 1003 (2012).

[8] X.-L. Qi, T. Hughes, S. Raghu, and S.-C. Zhang, Phys. Rev. Lett. **102**, 187001 (2009).

[9] G. Goll, M. Marz, A. Hamann, T. Tomanic, K. Grube, T. Yoshino, and T. Takabatake, Phys. B Condens. Matt. **403**, 1065 (2008).

[10] A. P. Schnyder, P. M. R. Brydon, and C. Timm, Phys. Rev. B **85**, 024522 (2012).

[11] T. V. Bay, T. Naka, Y. K. Huang, and A. de Visser, Phys. Rev. B **86**, 064515 (2012).

[12] F. F. Tafti, T. Fujii, A. Juneau-Fecteau, S. René de Cotret, N. Doiron-Leyraud, A. Asamitsu, and L. Taillefer, Phys. Rev. B **87**, 184504 (2013).

[13] S. Sasaki, Z. Ren, A. A. Taskin, K. Segawa, L. Fu, and Y. Ando, Phys. Rev. Lett. **109**, 217004 (2012).

[14] Y. S. Hor, A. J. Williams, J. G. Checkelsky, P. Roushan, J. Seo, Q. Xu, H. W. Zandbergen, A. Yazdani, N. P. Ong, and R. J. Cava, Phys. Rev. Lett. **104**, 057001 (2010).

[15] Y. S. Hor, J. G. Checkelsky, D. Qu, N. P. Ong, and R. J. Cava, J. Phys. Chem. Solids **72**, 572 (2011).

[16] M. Kriener, K. Segawa, Z. Ren, S. Sasaki, and Y. Ando, Phys. Rev. Lett. **106**, 127004 (2011).

[17] M. Kriener, K. Segawa, Z. Ren, S. Sasaki, S. Wada, S. Kuwabata, and Y. Ando, Phys. Rev. B **84**, 054513 (2011).

[18] L. A. Wray, S.-Y. Xu, Y. Xia, Y. S. Hor, D. Qian, A. V. Fedorov, H. Lin, A. Bansil, R. J. Cava, and M. Z. Hasan, Nat. Phys. **6**, 855 (2010).

[19] L. Fu and E. Berg, Phys. Rev. Lett. **105**, 097001 (2010).

[20] P. Das, Y. Suzuki, M. Tachiki, and K. Kadowaki, Phys. Rev. B **83**, 220513 (2011).

[21] S. Sasaki, M. Kriener, K. Segawa, K. Yada, Y. Tanaka, M. Sato, and Y. Ando, Phys. Rev. Lett. **107**, 217001 (2011).

[22] R. Balian and N. R. Werthamer, Phys. Rev. **131**, 1553 (1963).

[23] T. P. Orlando, E. J. J. McNiff, S. Foner, and M. R. Beasley, Phys. Rev. B **19**, 4545 (1979).

[24] M. L. Cohen, in *Superconductivity*, edited by R. D. Parks (Marcel Dekker, New York, 1969), Vol. 1, Chap. 12.

[25] N. R. Werthanmer, E. Helfand, and P. C. Hohenberg, Phys. Rev. **147**, 295 (1966).

[26] A. M. Clogston, Phys. Rev. Lett. **9**, 266 (1962).

[27] B. S. Chandrasekhar, Appl. Phys. Lett. **1**, 7 (1962).

[28] K. Maki, Phys. Rev. **148**, 362 (1966).

[29] F. Hardy and A. Huxley, Phys. Rev. Lett. **94**, 247006 (2005).

[30] N. T. Huy, D. E. de Nijs, Y. Huang, and A. de Visser, Phys. Rev. Lett. **100**, 077002 (2008).

[31] R. A. Klemm, A. Luther, and M. R. Beasley, Phys. Rev. B **12**, 877 (1975).

[32] J. Woollam and R. Somoano, Phys. Rev. B **13**, 3843 (1976).

[33] D. Youngner and R. Klemm, Phys. Rev. B **21**, 3890 (1980).

[34] H. Köhler, Solid State Commun. **13**, 1585 (1973).

[35] E. Lahoud, E. Maniv, M. S. Petrushevsky, M. Naamneh, A. Ribak, S. Wiedmann, L. Petaccia, Z. Salman, K. B. Chashka, Y. Dagan, and A. Kanigel, Phys. Rev. B **88**, 195107 (2013).

[36] R. A. Klemm and K. Scharnberg, Phys. Rev. B **22**, 5233 (1980).

[37] N. Levy, T. Zhang, J. Ha, F. Sharifi, A. Talin, Y. Kuk, and J. Stroscio, Phys. Rev. Lett. **110**, 117001 (2013).

[38] H. Peng, D. De, B. Lv, F. Wei, and C.-W. Chu, Phys. Rev. B **88**, 024515 (2013).

[39] T. Mizushima, A. Yamakage, M. Sato, and Y. Tanaka, arXiv:1311.2768v1 (2013).

Chapter 5 Unconventional superconductivity in the noncentrosymmetric Half Heusler YPtBi

In this chapter we first investigate the low-field magnetic response of the noncentrosymmetric superconductor YPtBi (T_c = 0.77 K). AC-susceptibility and DC-magnetization measurements provide solid evidence for bulk superconductivity with a volume fraction of ~ 70%. The lower critical field is surprisingly small: B_{c1} = 0.008 mT ($T \rightarrow 0$). Muon spin rotation experiments in a transverse magnetic field of 0.01 T show a weak increase of the Gaussian damping rate σ_{TF} below T_c, which yields a London penetration depth λ = 1.6 ± 0.2 μm. The zero-field Kubo–Toyabe relaxation rate Δ_{KT} equals 0.129 ± 0.004 μs^{-1} and does not show a significant change below T_c. This puts an upper bound of 0.04 mT on the spontaneous magnetic field associated with a possible odd-parity component in the superconducting order parameter.

Secondly, to shed further light on the nature of the superconducting phase of YPtBi we performed transport measurements under pressure up to 2.51 GPa. Under pressure superconductivity is enhanced and T_c increases at a linear rate of 0.044 K/GPa. The upper critical field $B_{c2}(T)$ curves taken at different pressures collapse onto a single curve, with values that exceed the model values for spin-singlet superconductivity. The B_{c2} data point to the presence of an odd-parity Cooper pairing component in the superconducting order parameter, in agreement with predictions for noncentrosymmetric and topological superconductors.

(Part of this chapter has been published as T. V. Bay *et al.*, Phys. Rev. B **86**, 064515 (2012) and T. V. Bay *et al.*, Solid State Comm. **183**, 13 (2014))

5.1 Introduction

Recently, the discovery of superconductivity in Half Heusler compounds that exhibit a topological type of electronic band order has offered a new route to search for topological superconductors. In the 111 transition bismuthide YPtBi superconductivity with the critical temperature T_c = 0.77 K [1], discovered in 2011, deserves a close examination owing to two unusual aspects. Firstly, YPtBi crystallizes in the Half Heusler MgAgAs structure [2] which lacks inversion symmetry, and, consequently, it is a noncentrosymmetric superconductor. The absence of an inversion center results in an electric field gradient which creates an antisymmetric Rashba type spin-orbit coupling, which in turn causes splitting of the energy bands and the Fermi surface. This may have crucial consequences for the superconducting condensate, as it can give rise to the mixture of even and odd parity Cooper pair states rather than to conventional spin-singlet states [3]. The field of noncentrosymmetric superconductors was initiated by the discovery of superconductivity in the heavy-fermion material $CePt_3Si$ (T_c = 0.75 K) [4]. Other well-documented examples of noncentrosymmetric superconductors are $CeRhSi_3$ (T_c = 1.1 K under pressure) [5], $CeIrSi_3$ (T_c = 1.6 K under pressure) [6], Li_2Pt_3B (T_c = 2.6 K) [7], and Mo_3Al_2C (T_c = 9.2 K) [8,9]. Non-centrosymmetric superconductors attract ample attention as test-case systems for research into unconventional superconducting phases [10]. The second reason of interest is the possibility that YPtBi is a topological superconductor. Electronic structure calculations for a series of non-magnetic ternary Half Heusler compounds predict a topologically non-trivial band structure, notably a substantial band inversion, due to strong spin-orbit coupling [11-13].

Among the 111 platinum bismuthides, especially YPtBi, LaPtBi and LuPtBi are predicted to have a strong band inversion, which makes them promising candidates for 3D topological insulating or topological semimetallic behaviour. A topological insulator has the intriguing property that its interior is an insulator, while the surface harbors metallic states that are protected by topology [14,15]. Indeed, YPtBi [1,2,16], LaPtBi [17] and LuPtBi [18,19] are low carrier density systems and their transport properties reveal semi-metallic behaviour. For LuPtBi, metallic surface states have been observed in ARPES experiments [20], but solid evidence for a topologically non-trivial surface state has not been provided to date. Interestingly, superconductivity has also been reported for LaPtBi (T_c = 0.9 K [17]) and LuPtBi (T_c = 1.0 K [19]). The non-trivial topology of the electronic bands makes these platinum bismuthides candidates for topological superconductivity, with mixed parity Cooper pair states in the bulk and protected Majorana surface states [14,15]. The field of topological superconductors attracts tremendous attention, but unfortunately, hitherto, only a few

candidate materials have been discovered. Other potential candidates are $Cu_xBi_2Se_3$ [21,22], $Sn_{1-x}In_xTe$ [23] and ErPdBi [24].

YPtBi has a cubic structure and crystallizes in the $F\bar{4}3m$ space group. It was first prepared as a non-*f* electron reference material in systematic investigations of magnetism and heavy-fermion behavior in the REPtBi series [25]. Magnetotransport measurements carried out on single crystals grown using Bi flux point to semimetallic-like behavior [1,25]. The resistivity $\rho(T)$ increases steadily upon cooling below 300 K and levels off below ~ 60 K [1]. The Hall coefficient R_H is positive and quasilinear in a magnetic field, allowing for an interpretation within a single-band model with hole carriers [1]. The carrier concentration n_h is low and shows a substantial decrease upon cooling from 2×10^{19} cm^{-3} at 300 K to 2×10^{18} cm^{-3} at 2 K. Concurrently, the Sommerfeld coefficient in the specific heat is very small, $\gamma \leq 0.1$ mJ/molK^2 [26]. YPtBi is diamagnetic and the magnetic susceptibility χ attains a temperature independent value of -10^{-4} emu/mol ($T \rightarrow 0$) [26]. The transition to the superconducting state takes place at T_c = 0.77 K [1], where the resistivity sharply drops to zero. At the same temperature a diamagnetic screening signal appears in the ac susceptibility χ_{ac}, but the magnetic response is sluggish upon lowering temperature. The upper critical field $B_{c2}(T)$ shows an unusual quasilinear behavior and attains a value of ~ 1.5 T for $T \rightarrow 0$ K [1]. Heat capacity, $C(T)$, measurements around the normal-to-superconducting phase transition [27], do not show the universal step $\Delta C / \gamma T_c \simeq 1.43$ expected for a weak coupling spin singlet superconductor, but rather a break in slope of C/T at T_c. Thus the specific heat data fail to provide evidence for bulk superconductivity. We note that the extremely small γ value makes this a difficult experiment. However, the subsequent confirmation of superconductivity with an identical critical temperature T_c = 0.77 K in our single crystals of YPtBi and the results of AC- and DC-magnetization measurements, which yield a superconducting volume fraction of ~ 70%, provide solid evidence for bulk superconductivity.

5.2 Sample preparation and characterization

The YPtBi samples investigated in this chapter have been supplied by two different sources. For the low field investigation (section 5.3), the samples were prepared out of Bi flux [28] by Dr. T. Orvis at the Department of Physics and Astronomy, Stony Brook University, USA. Several YPtBi batches contained rather tiny crystals which had predominantly a pyramid-shape (edge size ≤ 1 mm) with the base aligned along the [111] direction. X-ray powder diffraction was used to confirm the $F\bar{4}3m$ space group. For the pressure experiment (section 5.4), several batches of YPtBi were also fabricated out of Bi flux [28] from a starting

composition Y:Pt:Bi = 1:1:1.4 by Dr. Y.K. Huang at the WZI. First Pt and Bi were melted together and put with Y in an alumina crucible. The crucible was placed in a quartz tube, which was sealed in an argon atmosphere (p = 0.3 bar). The tube was heated slowly and kept at a temperature of 1250 °C for 24 h. The cooling rate was 1 °C/h down to 900 °C. The collected crystals have sizes up to 4 mm. Electron probe microanalysis confirmed the 1:1:1 ratio. X-ray powder diffraction was used to check the $F\bar{4}3m$ space group and the results are shown in Fig 5.1. Strong peaks in the pattern at diffraction angles 2θ, which correspond to diffraction from the sets of planes with the Miller indices indicated, are in good agreement with the simulated curve for the $F\bar{4}3m$ space group. The deduced lattice parameter a = 6.650 Å is in good agreement with the literature [1]. Single crystals taken from these batches reproducibly showed superconductivity with a resistive transition at T_c = 0.77 K.

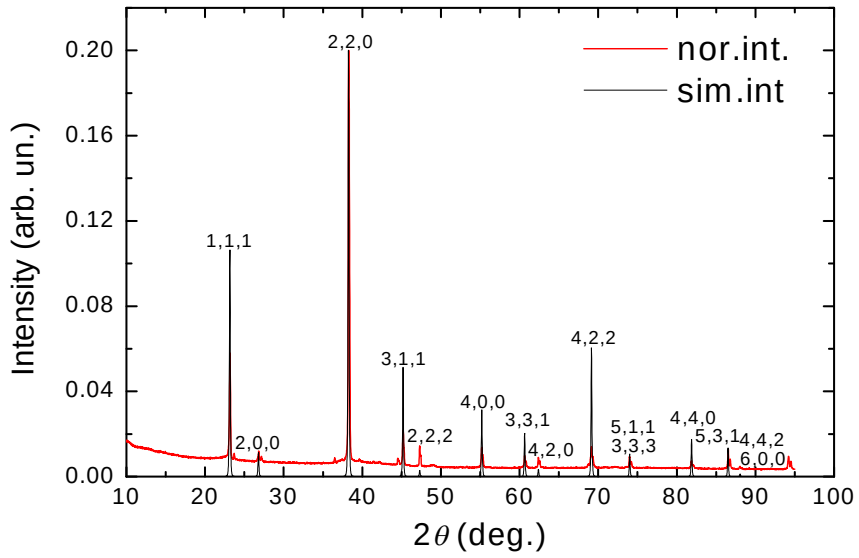

Figure 5.1 X-ray powder diffraction pattern of YPtBi where Miller indices are indicated labeling the diffraction peaks. The data (red solid line) are compared to the simulated curve for the $F\bar{4}3m$ space group (black solid line).

5.3 Low field experiments

5.3.1 Sample characterization

As mentioned above, various batches of YPtBi have been synthesized. This section on the low field investigation focuses on the batch which possesses pyramid-shaped tiny crystals (edge size ≤ 1 mm) grown in Stony Brook. The resistance, $R(T)$, reveals semi-metallic behaviour with a broad maximum around 80 K as shown in Fig. 5.2. The superconducting transition to

zero resistance for this crystal is shown in the inset of Fig. 5.2. T_c determined by the midpoint of the transition is 0.98 K, which is higher than in the literature. The width of the superconducting transition is relatively large $\Delta T_c = 0.36$ K with a weak tail towards low temperatures. The diamagnetic χ_{ac} signal, measured at a frequency of 16 Hz and a driving field $B_{ac} = 0.026$ mT, sets in at T = 0.80 K, *i.e.* when the transition in the resistance is complete. We note that the sluggish transition in χ_{ac} obtained in this way becomes much sharper when B_{ac} is reduced to below 0.001 mT (see the next section). The magnetoresistance traces taken at liquid helium-3 temperatures display Shubnikov-de Haas (SdH) oscillations (Fig. 5.3) which attest to the high quality of the sample. The hole carrier concentration, n_h, deduced from the SdH signal equals 1.3×10^{18} cm^{-3}. This number is in agreement with the value reported previously for a semimetallic sample [1].

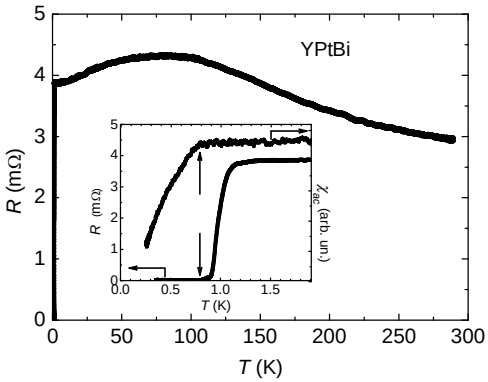

Figure 5.2 Resistance of YPtBi as as function of temperature showing semi-metallic behaviour. Inset: Superconducting transition in resistance (lower line, left axis) and in AC-susceptibility in a driving field B_{ac} = 0.026 mT (upper line, right axis); arrows indicate R = 0 and the onset of the diamagnetic signal, respectively.

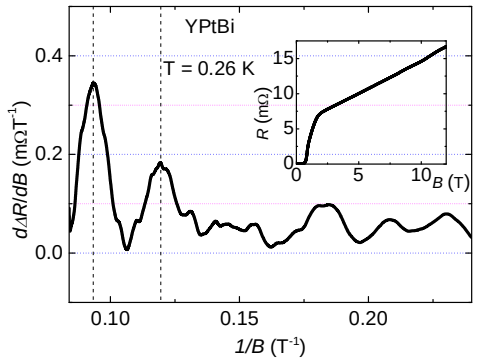

Figure 5.3 Derivative, $d\triangle R/dB$, as a function of inverse magnetic field $1/B$ of YPtBi. SdH oscillations are present with a single frequency F = 38 T at T = 0.26 K. Inset: resistance versus magnetic field (raw data).

5.3.2 Low-field magnetization and AC-susceptibility

For the magnetic measurements 10 small single crystals were arranged in a circular cluster with a total mass of 42 mg. DC-magnetization and AC-susceptibility measurements were made by Dr. C. Paulsen and Dr. M. Jackson using a SQUID magnetometer, equipped with a miniature dilution refrigerator, developed at the Néel Institute. As concerns χ_{ac}, the in-phase, χ', and out-of-phase, χ'', signals were measured in driving fields $B_{ac} \leq 0.1$ mT with a frequency of 2.1 Hz. The diamagnetic signal is corrected for demagnetization effects:

$$\chi_{diam} = -1/(1-N) \qquad (5.1)$$

Here we used N = 1/3, since the sample is effectively a 'powder'.

The temperature variation of the AC-susceptibility is reported in Fig. 5.4. For the collection of single crystals we find T_c = 0.77 K, as determined by the onset temperature of the diamagnetic signal. This value of T_c is in good agreement with the results reported in Ref. [1]. Note that χ'(T) and χ"(T) show a strong dependence on B_{ac}. For the smallest values of B_{ac} (≤ 0.001 mT) the standard behaviour for a superconductor is observed: χ'(T) shows a relatively sharp drop below T_c, and χ"(T) shows a peak due to dissipation. However, with increasing values of B_{ac} the transition broadens rapidly. This explains the sluggish temperature variation of χ' measured with B_{ac} = 0.026 mT reported in Fig. 5.2. The strong variation as a function of B_{ac} indicates a small value of the lower critical field B_{c1}. Another important result is the large value of the diamagnetic screening signal which is reached for B_{ac} = 0.0001 mT. This points to a superconducting volume fraction of 67 %.

The AC-susceptibility signal measured as a function of B_{ac} provides a very sensitive way to probe B_{c1} [29]. Notably, the imaginary part of the susceptibility, χ", which is related to losses and hysteresis, is an excellent indicator of the first flux penetration in the sample. If there is a perfect Meissner state up to B_{c1} then

$$\chi''(T) = 0 \text{ for } B_{ac} \le B_{c1}$$

and

$$\chi''(T) = \beta \frac{B_{ac} - B_{c1}}{B_{ac}} \text{ for } B_{ac} > B_{c1} \qquad (5.2)$$

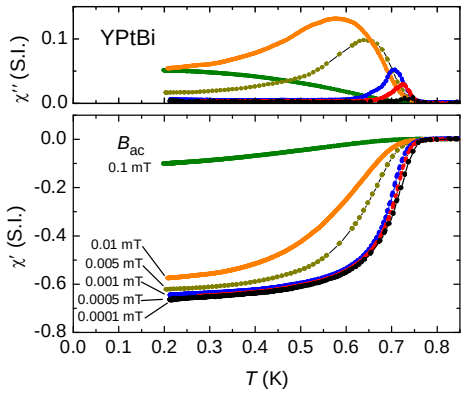

Figure 5.4 AC susceptibility as a function of temperature of YPtBi for different driving fields B_{ac} as indicated. Lower frame: χ'. Upper frame: χ".

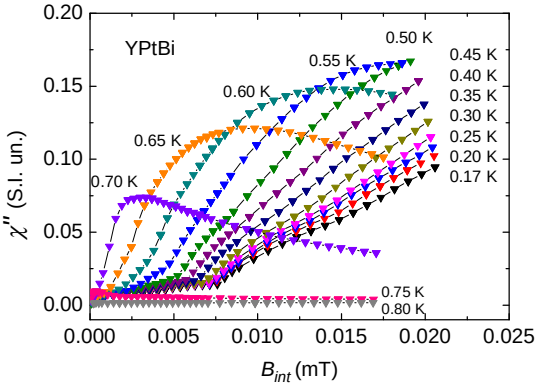

Figure 5.5 AC susceptibility as a function of the internal field B_{int} at temperatures as indicated. B_{int} is obtained by correcting for demagnetization effects (see the text).

Here β is a parameter that depends on the sample geometry and is related to screening currents according to the critical state model [30]. In Fig. 5.5 we report χ" as a function of the internal field B_{int} which is obtained by correcting for demagnetization effects: $B_{\text{int}} = B_{ac}(1 - N\chi')$. At the lowest temperature, T = 0.17 K, the clear kink observed near 0.0076 mT locates B_{c1}. Upon increasing the temperature the kink becomes more and more rounded. B_{c1}(T) determined in this way is traced in Fig. 5.6. In the normal state, *e.g.* at T = 0.80 K, χ"(T) is essentially flat. We remark that in the Meissner state χ"(B_{int}) is not equal to zero, but shows a weak quasi-linear increase. The origin of this behaviour is not clear. Possible explanations are sharp sample edges where flux could penetrate more easily, and the presence of an impurity phase with a very small critical field (< 0.001 mT). In the limit $T \to 0$, $B_{c1} = 0.0078$ mT. In Fig 5.6 we also compare the B_{c1}-data with the standard BCS quadratic temperature variation (see caption Fig. 5.6). A clear departure is found at the lowest temperatures. Alternatively, B_{c1} can be deduced from the DC-magnetization measured as a function of the applied field. M(B_{appl})-data taken at T = 0.17 K are shown in the inset of Fig. 5.6. B_{c1} determined in this way amounts to 0.0083 mT, in good agreement with the method described above.

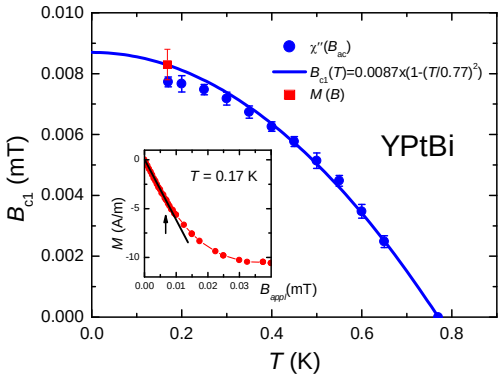

Figure 5.6 The lower critical field B_{c1} as a function of temperature. The solid line presents a quadratic dependence $B_{c1} = B_{c1}(0)\,(1 - (T/T_c)^2)$ with $B_{c1}(0)$ = 0.0087 mT and T_c = 0.77 K. Inset: DC-magnetization versus applied field B_{ac}(appl) at T = 0.17 K. The black arrow points to where M($B_{\text{appl.}}$) deviates from the linear behavior (black straight line) and flux penetrates the sample.

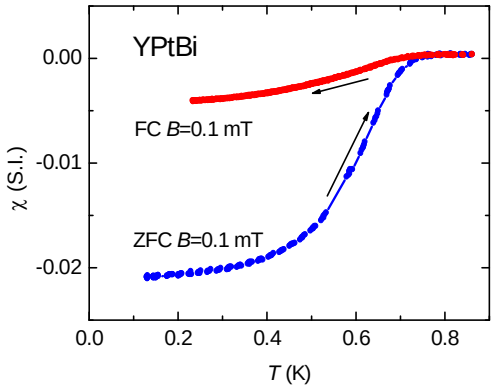

Figure 5.7 DC-susceptibility as a function of temperature in an applied field of 0.1 mT. After zero-field cooling (ZFC), a small magnetic field of 0.1 mT is applied. Next the sample is warmed up to above T_c and subsequently cooled in 0.1 mT (FC) to demonstrate flux expulsion.

Finally, we present DC-magnetization measurements in Fig. 5.7 that provide solid evidence for bulk superconductivity. After cooling in zero field, a field of 0.1 mT is applied in the superconducting state. This gives rise to a diamagnetic screening signal. Upon heating the sample to above T_c, the diamagnetic signal vanishes. On subsequent cooling, flux expulsion is clearly observed, which corresponds to a Meissner fraction of 0.4 volume%. Note that this fraction is very small because the applied field is much larger than B_{c1} and flux pinning is strong (see also Fig. 5.4).

5.3.3 Muon spin relaxation and rotation

Muon spin rotation and relaxation experiments (μSR) were carried out at the πM3 beamline at the Paul Scherrer Institute. The motivation for the experiments was two-fold: (*i*) to investigate the appearance of a spontaneous magnetic signal due to the breaking of time reversal symmetry associated with a possible odd parity component of the superconducting order parameter, and (*ii*) to determine the London penetration depth, λ, in the superconducting state. Measurements were made in the Low Temperature Facility (LTF) in the temperature range T = 0.02-1.8 K in zero field (ZF) and weak transverse fields (TF). The 'polycrystalline' sample consisted of a large ensemble of tiny crystals glued in a random crystal orientation on a silver backing plate with General Electric (GE) varnish. The sample area amounted to 10 x 14 mm^2. AC-susceptibility measurements confirmed T_c = 0.77 K.

In Fig. 5.8 we show ZF μSR spectra taken at 1.8 K and 0.019 K. The depolarization of the muon ensemble is weak and does not change significantly with temperature. The spectra are best fitted with the standard Kubo-Toyabe function [31]

$$G_{KT}(t) = \frac{1}{3} + \frac{2}{3}\left(1 - \Delta_{KT}^2 t^2\right)\exp\left(-\frac{1}{2}\Delta_{KT}^2 t^2\right) \qquad (5.3)$$

The Kubo-Toyabe function describes the muon depolarization due to an anisotropic Gaussian distribution of static internal fields centered at zero field. $\Delta_{KT} = \gamma_\mu \sqrt{\langle B \rangle^2}$ is the Kubo-Toyabe relaxation rate, with γ_μ the muon gyromagnetic ratio ($\gamma_\mu / 2\pi = 135.5$ MHz/T) and $\langle B \rangle^2$ the second moment of the field distribution. Note that the characteristic minimum at $t / \Delta_{KT} = 1.74$ and the recovery of the 1/3 term is not observed in this time window because of the small relaxation rate. In this temperature range the extracted values of Δ_{KT} are the same within the error bars. The average value is 0.129 ± 0.004 μs^{-1} (see Fig. 5.10, upper frame). The field distribution is most likely arising from the nuclear moments of the ^{89}Y, ^{195}Pt and

^{209}Bi isotopes which can be considered as static within the μSR time-window. The sizeable value of Δ_{KT} reflects a broad distribution of internal fields, which can be attributed to the polycrystalline nature of the sample. The uncertainty in Δ_{KT} allows the determination of an upper bound for a possible additional spontaneous magnetic field below T_c of 0.04 mT.

μSR spectra in a transverse field (TF) B_{TF} = 0.01 T taken at 1.8 K and 0.051 K are shown in Fig. 5.9. Note that the TF was applied after cooling in ZF. The spectra were fitted to the depolarization function

$$G_{KT}(t) = \exp\left(-\frac{1}{2}\sigma_{TF}^2 t^2\right)\cos\left(2\pi\nu t + \phi\right) \qquad (5.4)$$

Here σ_{TF} is the Gaussian damping factor, $\nu = \gamma_\mu B_{TF}/2\pi$ is the precession frequency where B_μ is the average field seen by the muon ensemble and ϕ is a phase factor. The temperature variation of σ_{TF} is shown in Fig. 5.10 (lower frame). In the normal phase σ_{TF} = 0.105 ± 0.005 μs^{-1} and represents here again a field distribution due to the nuclear moments. Upon lowering the temperature a weak increase is found below T_c that is attributed to the μ^+ depolarization σ_{FLL} due to the flux line lattice. The corresponding relaxation rate can be calculated from the relation

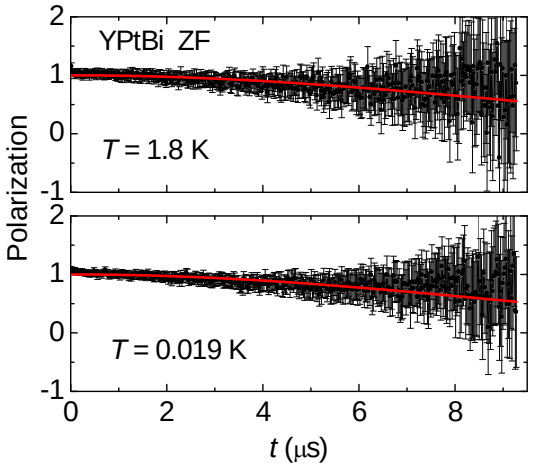

Figure 5.8 Time dependence of the normalized muon depolarization of YPtBi in zero external field (ZF) at 1.8 K (upper frame) and 0.019 K (lower frame). The solid red lines are fits to the Kubo-Toyable depolarization function, Eq. (5.3).

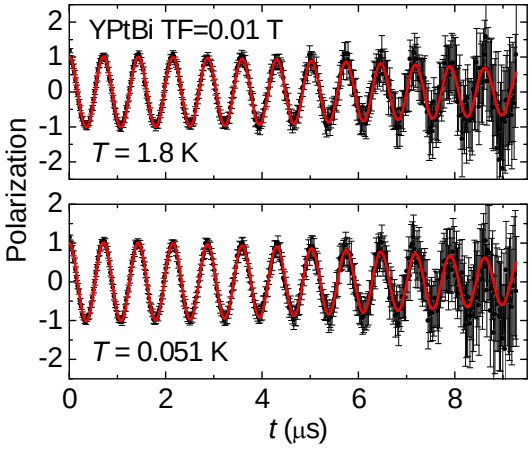

Figure 5.9 Time dependence of the normalized muon depolarization of YPtBi in a transverse field of 0.01 T (TF) at 1.8 K (upper frame) and 0.051 K (lower frame). The solid red lines are fits to a depolarization function with a precession frequency and Gaussian damping, Eq. (5.4).

$$\sigma_{FLL} = \sqrt{\left(\sigma_{TF,T<T_c}\right)^2 - \left(\sigma_{TF,T>T_c}\right)^2} \qquad (5.5)$$

and is estimated to be 0.04 ± 0.01 μs^{-1}. For a type II superconductor and $B \gg B_{c1}$ the London penetration depth can be estimated from the relation [32]

$$\left\langle B^2 \right\rangle = 0.003706 \times \Phi_0^2 / \lambda^4, \qquad (5.6)$$

where Φ_0 is the flux quantum. With σ_{FLL}= 0.04 ± 0.01 μs^{-1} we calculate λ=1.67 ± 0.2 μm for $T \to 0$. This value is about three times larger than the lattice parameter of the presumably trigonal flux line lattice induced by the 0.01 T field

$$a_{\Delta} = \left(4/3\right)^{1/4} \left(\Phi_0 / B\right)^{1/2} = 0.49 \ \mu\text{m}. \qquad (5.7)$$

Note that the relatively large error bar on σ_{FLL} does not allow for an accurate determination of the temperature variation of λ, thereby impeding the detection of possible power laws in the excitation spectrum of the superconducting state.

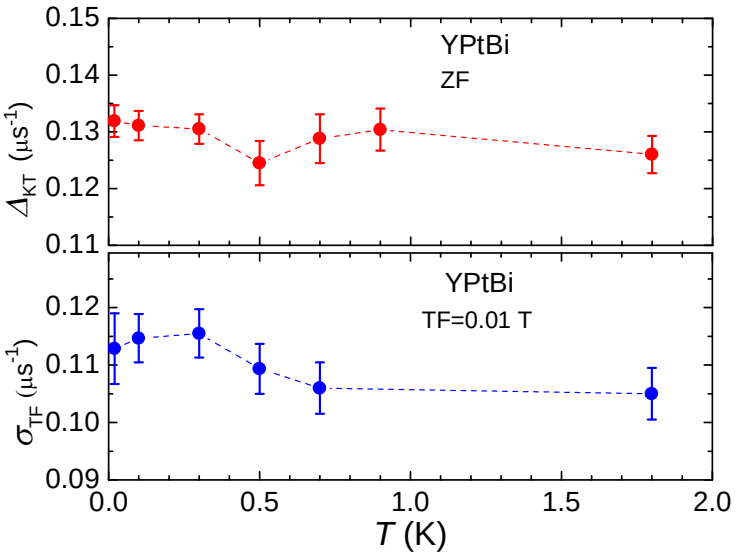

Figure 5.10 Temperature dependence of the Kubo-Toyabe relaxation rate in zero field (upper frame) and of the Gaussian damping rate for muon depolarization in YPtBi in a transverse field of 0.01 T (lower frame). The dashed lines connect the data points.

5.3.4 Discussion

Since YPtBi is a low-carrier density system, the London penetration depth is expected to be large. The London penetration depth is related to the superfluid density n_s via the Ginzburg-Landau relation $n_s = m_h^* / \mu_0 e^2 \lambda^2$, where m_h^* is the effective mass of the charge (hole) carriers, μ_0 is the permeability of the vacuum and e the elementary charge. With the experimental values $\lambda = 1.67 \pm 0.2$ μm and $m_h^* = 0.15\ m_e$ [1] we calculate $n_s = (1.7 \pm 0.4) \times 10^{18}$ cm^{-3}, which

is in agreement with the carrier concentration determined from the SdH effect, $n_h = 1.3\times10^{18}$ cm^{-3} (see Section 5.3.1). Thus the transport and the TF μSR data give a consistent picture.

With help of the characteristic length scales of the superconducting state, λ and ξ, the lower critical field can be deduced from the Ginzburg-Landau relation

$$B_{c1} = \Phi_0 \ln(\lambda/\xi)/(4\pi\lambda^2). \qquad (5.8)$$

Here ξ = 17 nm [16] is calculated from the upper critical field $B_{c2} = \Phi_0/2\pi\xi^2$ and the Ginzburg-Landau parameter $\kappa = \lambda/\xi$ = 94. Using the experimental value λ = 1.6 ± 0.2 μm we obtain B_{c1} = 0.29 ± 0.05 mT ($T \to 0$). Surprisingly this value is a factor 36 larger than the measured value of 0.008 mT (Section 5.3.2). Alternatively, to match the measured B_{c1}-value λ should be equal to ~ 11 μm rather than 1.6 μm. This in turn would entail σ_{FLL} ~ 0.001 μs^{-1}, a value not compatible with the analysis of the μSR and transport data. It is tempting to attribute this discrepancy to an intricate relation between B_{c1} and λ, going beyond the simple Ginzburg-Landau approach. In particular, a non-unitary Cooper pair state will have an intrinsic magnetic moment, which could result in a very small B_{c1}-value [29]. The spontaneous internal field at the muon localization site associated with the unitary state should however be smaller than 0.04 mT in the limit $T \to 0$. Further evidence for an odd-parity component in the superconducting order parameter is provided by the reduced B_{c2}-values (see Section 5.4.2) [22]. We note that $B_{c1}(T)$ deviates from the standard BCS behaviour (Fig. 5.6) in the same temperature range as $B_{c2}(T)$. Clearly, this calls for theoretical studies with regard to flux penetration in superconductors with a mixed order parameter component. From the experimental side, notably with regards to the μSR, it would be highly desirable to work with a large, homogeneous single crystal, which is expected to significantly reduce the background relaxation rates. Together with improved statistics, this will enable one to resolve the temperature variation of λ and to shed further light on the magnitude of the spontaneous internal magnetic moment in the YPtBi system.

5.4 High pressure experiments

5.4.1 Resistivity

In this study, we used an YPtBi batch prepared by dr. Y.K. Huang which contained rather big crystals with sizes up to 4 mm. In Fig. 5.11 we show a typical resistivity trace $\rho(T)$ at ambient pressure. Upon cooling below 300 K, $\rho(T)$ gradually drops and levels off below 30 K. This demonstrates these YPtBi crystals behave as a metal, rather than as a semimetal as reported in

the previous section and in Refs. 1 and 25. The carrier concentration $n_h(T)$ extracted from Hall measurements is low and displays a weak temperature variation (Fig. 5.11). Near room temperature the transport parameters of these samples are quite similar to those reported in Ref. 1: ρ(295 K) equals 230 $\mu\Omega$cm versus 300 $\mu\Omega$cm (in Ref. 1) and n_h(295 K) equals 2.2 × 10^{19} cm^{-3} versus 2.0 × 10^{19} cm^{-3} (in Ref. 1). A major difference is found in $n_h(T)$, which is close to temperature independent for this large single crystal, but was reported to drop by a factor 10 upon cooling to 2 K in Ref. 1. The origin of the dissimilar transport behavior is not clear. Possibly trapping of carriers at defects upon lowering the temperature causes the semimetallic-like behavior observed in the samples studied in the previous section and in Refs. 1 and 25. The metallic behavior of the larger single crystal grown in Amsterdam is robust under pressure (see the inset in Fig. 5.11). Under pressure R(295 K) increases linearly, resulting in a 20% increase at the maximum pressure applied of 2.51 GPa. The residual resistance R(4 K) increases at the same rate. The residual resistance ratio, *RRR* defined as R(295 K)/R(4 K), of our samples amounts to 1.4 at p = 0. A sharp superconducting transition is observed for all samples at T_c = 0.77 K. The width of the transition T_c, as determined between 10 and 90% of the normal state R value, is 0.06 K.

The superconducting transition under pressure in zero magnetic field is shown in Fig. 5.12 (sample #2). Note that the p = 0 data were taken on sample #1 in a separate experiment. T_c, as determined by the maximum in the slope $d\rho/dT$, increases linearly with pressure at a rate of 0.044 K/GPa (see inset in Fig. 5.12). The width of the transition does not change with pressure, which is indicative of homogeneously applied pressure. The $\rho(T)$ data taken on sample #2 (under pressure) show a tiny structure just above 1 K. This feature is insensitive to pressure and suppressed by a small magnetic field (B ~ 0.1 T, see Fig. 5.13). It has not been observed in other samples.

The relatively weak pressure dependence of $\rho(T)$ and the enhancement of T_c with pressure are unexpected for a low carrier density material. For instance in $Cu_xBi_2Se_3$, which has a comparable metallic behavior and low carrier concentration, the resistance is enhanced and T_c decreases under pressure as reported in chapter 4 of this thesis. In the case of $Cu_xBi_2Se_3$ the variation of $T_c(p)$ can be understood qualitatively in a simple model, where

$$T_c \sim \Theta_D \exp\left[\frac{-1}{N(0)V_0}\right], \qquad (5.9)$$

with Θ_D the Debye temperature, $N(0) \sim m^* n^{1/3}$ the density of states (with m^* the effective mass), and V_0 the effective interaction parameter [33]. For $Cu_xBi_2Se_3$, n decreases with pressure, and accordingly T_c decreases as mentioned in chapter 4. For YPtBi, the weak

variation of R with pressure (Fig. 5.11) suggests n is close to being pressure independent. Therefore, the increasing trend in $T_c(p)$ indicates that the product $N(0)V_0$ has a more involved dependence on pressure in YPtBi.

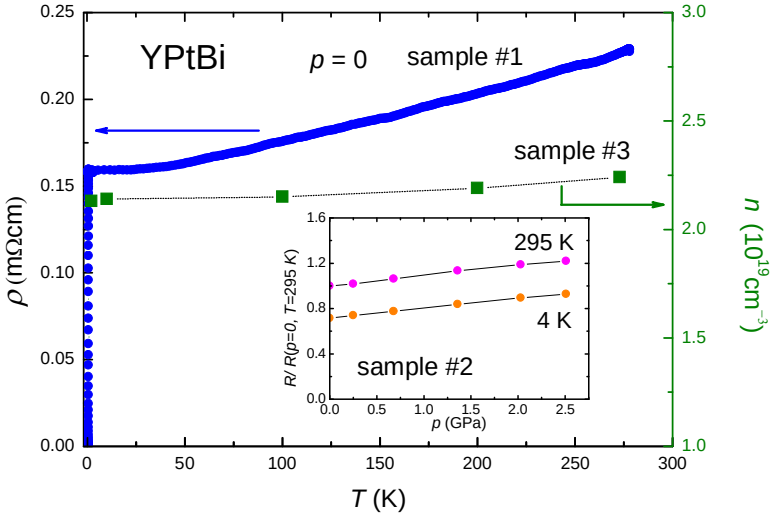

Figure 5.11. Resistivity (closed circles; left axis) and carrier concentration (closed squares; right axis) of YPtBi as a function of temperature at ambient pressure. Inset: Resistance at 295 and 4 K as a function of pressure. Resistance values are normalized to the room temperature value at ambient pressure, $R(p = 0, T = 295\ \mathrm{K})$.

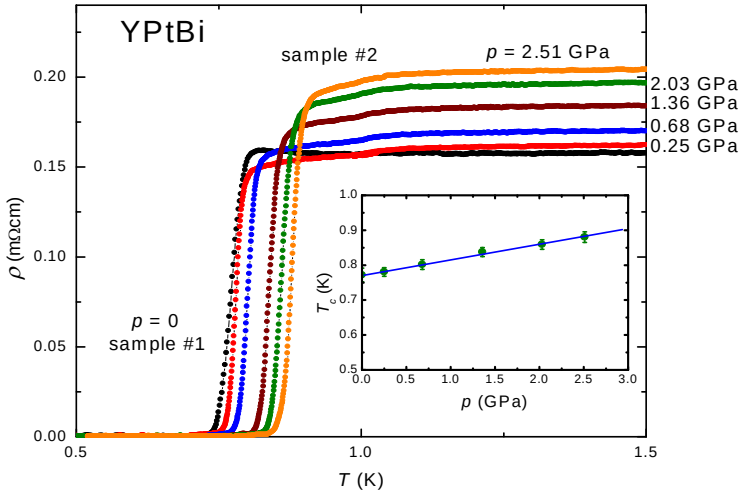

Figure 5.12. Superconducting transition of YPtBi at pressures of 0, 0.25, 0.68, 1.36, 2.03 and 2.51 GPa (at the steepest descent of the resistivity from left to right). Data at $p = 0$ are taken on sample #1; data under pressure on sample #2. Inset: Superconducting transition temperature as a function of pressure. The solid line is a linear fit to the data points with slope $dT_c/dp = 0.044$ K/GPa.

5.4.2 Upper critical field B_{c2}

A systematic study of the temperature dependence of the resistance around the superconducting transition in fixed fields under pressure up to 2.51 GPa is reported in Fig.

5.13. Overall, SC is observed as a sharp transition to $R = 0$ and is gradually suppressed by magnetic field. For sample #3 measured at $p = 0$, the width of the transition, $\triangle T_c$, increases almost by a factor 2 to 0.12 K in the highest field. For sample #2, measured under pressure, $\triangle T_c$ is virtually pressure and field independent, which attests to its high quality sample. $T_c(B)$ determined by the maximum in $d\rho/dT$ at fixed B is reported for each pressure in Fig. 5.14. $B_{c2}(T)$ is dominated by a quasilinear temperature dependence down to $T_c/3$. At lower temperatures, data taken in the dilution refrigerator show that $B_{c2}(T)$ curves upward, away from the linear behavior. For $p = 0$ we obtain $B_{c2}(T \rightarrow 0) \simeq 1.23$ T. Notice that close to T_c all data sets show a weak curvature or tail. The curvature is less pronounced for the better sample (#2) measured under pressure.

Next we extract parameters that characterize the superconducting state and investigate whether our samples are sufficiently pure to allow for odd-parity superconductivity [34]. From the relation

$$B_{c2} = \frac{\phi_0}{2\pi\xi^2}, \qquad (5.10)$$

where ϕ_0 is the flux quantum, we calculate a superconducting coherence length ξ = 17 nm.

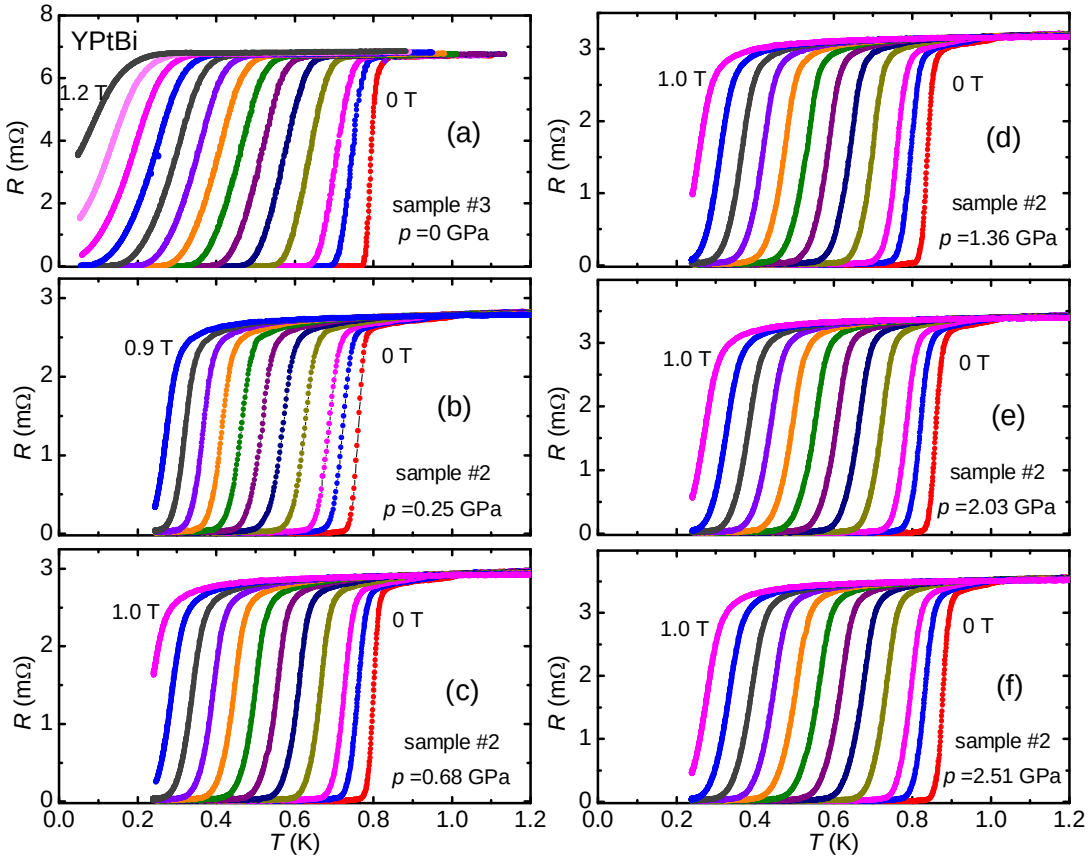

Figure 5.13. Evolution of temperature dependence of resistance in fixed fields: 0, 0.05, 0.1, 0.2, …, 1.2 T (from right to left as indicated) of YPtBi single crystals as a function of pressure: 0 (sample #3), and 0.25, 0.68, 1.36, 2.03, 2.51 GPa (sample #2).

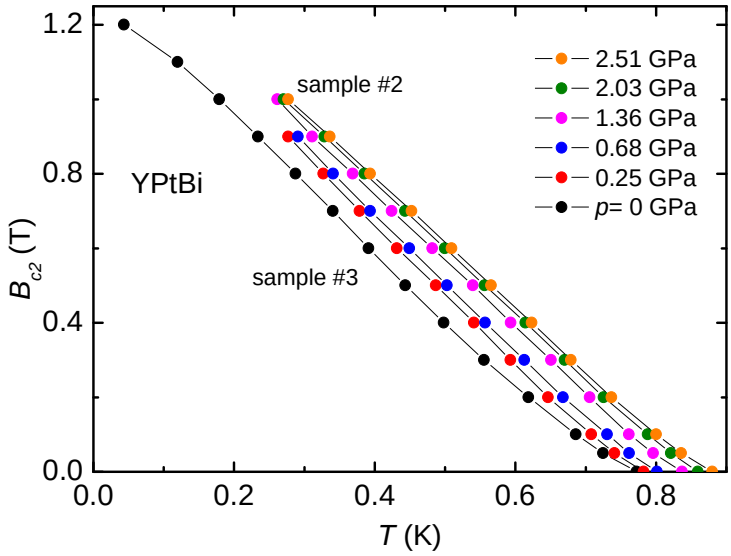

Figure 5.14. Temperature variation of the upper critical field $B_{c2}(T)$ at pressures of 0, 0.25, 0.68, 1.36, 2.03, and 2.51 GPa (from bottom to top). Data at p = 0 are taken on sample #3; data under pressure on sample #2.

An estimate for the electron mean free path ℓ can be obtained from the relation

$$\ell = \frac{\hbar k_F}{\rho_0 n e^2}, \qquad (5.11)$$

assuming a spherical Fermi surface $S_F = 4\pi k_F^2$ with Fermi wave vector $k_F = (3\pi^2 n)^{1/3}$. With $n = 2.2\times10^{25}$ m^{-3} and $\rho_0 = 1.6\times10^{-6}$ Ωm (see Fig. 5.11), we calculate k_F = 0.9 × 10^9 m^{-1} and $\ell = 105$ nm. Thus $\ell > \xi$, which tells us YPtBi is in the clean limit. Similar values for ℓ and ξ were obtained in Ref. 1. A more elaborate analysis can be made by employing the slope of the upper critical field dB_{c2}/dT at T_c [35]

$$\left|dB_{c2}/dT\right|_{T_c} = 4480\gamma\rho_0 + 1.38\times10^{35}\gamma^2 T_c / S_F^2 \qquad (5.12)$$

Assuming $\gamma \sim n^{1/2}$ we estimate for our sample γ = 7.3 J/m^3 K^2 based on the value of 2.3 J/m^{3}K^2 (Ref. 26) and by taking into account that for our sample n at low T is 10 × higher than reported in Ref. 1. With the experimental values ρ_0 = 1.6 × 10^{-6} Ωm, T_c = 0.77 K, and $|dB_{c2}/dT|_{Tc}$ = 1.9 T/K (see Fig. 5.14, we neglect the weak curvature close to T_c), we calculate k_F = 0.4 × 10^9 m^{-1}, ξ = 20 nm, and $\ell = 582$ nm. This confirms $\ell > \xi$. The weak pressure response of the transport parameters justifies the conclusion that the clean limit behavior is also obeyed under pressure.

In an analysis mirroring that presented in chapter 4 for $Cu_{0.3}Bi_2Se_3$ for a standard weak-coupling spin-singlet superconductor in the clean limit, the orbital critical field is given by

$$B_{c2}^{orb} = 0.72 T_c \left| dB_{c2} / dT \right| T_c \qquad (5.13)$$

within the Werthamer-Helfand-Hohenberg [WHH] model [36] (see chapter 3). If one considers in addition the suppression of the spin-singlet state by paramagnetic limiting [37,38], the resulting critical field is reduced to

$$B_{c2} = B_{c2}^{orb}(0) \frac{1}{\sqrt{1+\alpha^2}}, \qquad (5.14)$$

with the Maki parameter (Refs. 36 and 39)

$$\alpha = \sqrt{2} \frac{B_{c2}^{orb}(0)}{B^P(0)} \qquad (5.15)$$

and the Pauli limiting field $B^P(0) = 1.86 \times T_c$. For YPtBi we calculate B_{c2}^{orb} = 1.05 T, $B^P(0)$ = 1.43 T, α = 1.04, and $B_{c2}(0)$ = 0.73 T. The latter value is much lower than the experimental value $B_{c2}(0)$ = 1.24 T, and we therefore conclude that B_{c2} is dominated by the orbital limiting field.

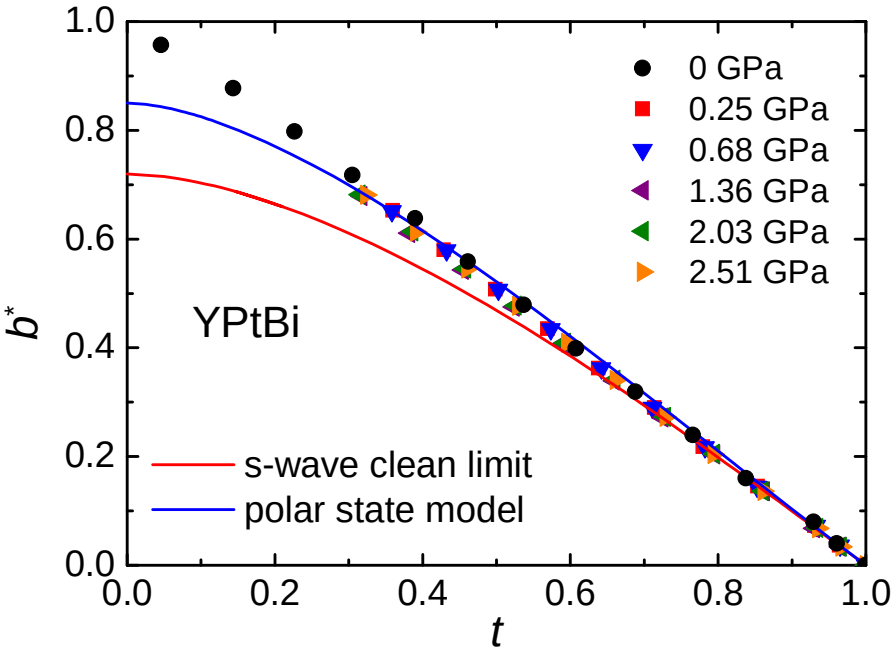

Figure 5.15. Reduced upper critical field *b*(t)* (see text) as a function of the reduced temperature $t = T/T_c$ at pressures of 0, 0.25, 0.68, 1.36, 2.03, and 2.51 GPa. Notice that we neglected the small tail close to T_c and obtained $|dB_{c2}/dT|_{Tc}$ from the field range B = 0.1 to 0.2 T. The lower and upper solid lines represent model calculations for *s*- and *p*-wave superconductors, respectively (see text).

In Fig. 5.15 we present the B_{c2} data at different pressures in a reduced plot $b^*(t)$, with

$$b^* = \left(B_{c2} / T_c\right) / \left|dB_{c2} / dT\right|_{T_c} \tag{5.16}$$

and $t = T/T_c$ the reduced temperature. All the $B_{c2}(T)$ curves collapse onto a single function $b^*(t)$. In Fig. 5.15 we have also traced the universal B_{c2} curve for a clean orbital limited spin-singlet superconductor within the WHH model [36]. Clearly, the data deviate from the predicted standard spin-singlet behavior. Notably, the fact that our experimental B_{c2} data are well above even these universal values is a strong argument in favor of odd-parity superconductivity. A similar conclusion based on B_{c2} data was drawn for the candidate topological superconductor $Cu_xBi_2Se_3$ as discussed in chapter 4. Finally, we compare the $B_{c2}(T)$ data with the polar-state model function of a spin-triplet superconductor [40]. Overall, the B_{c2} values match the model function better, but significant discrepancies still remain. Notably, the unusual quasilinear $b^*(t)$ down to $t/3$ is not accounted for, while below $t/3$ the data obviously exceed the model function values. Evidently, more theoretical work is needed to capture the intricate behavior of mixed spin-singlet and spin-triplet superconductors in an applied magnetic field.

5.5 Conclusion

The superconducting properties of YPtBi deserve attention because the structure lacks inversion symmetry, which may give rise to unconventional superconductivity. Moreover, YPtBi has an electronic band inversion and is predicted to host topological surface states. We have investigated the nature of the superconducting phase in this system by means of resistivity, magnetization and μSR experiments. Superconductivity is confirmed at T_c = 0.77 K. AC-susceptibility and DC-magnetization data provide unambiguous proof this is a bulk effect. The lower critical field B_{c1} = 0.008 mT ($T \rightarrow 0$) is surprisingly small. This is a robust property, which presumably finds an explanation in a non-unitary superconducting order parameter. Muon spin rotation experiments in a transverse field of 0.01 T show a weak increase of the Gaussian damping rate σ_{TF} below T_c, which yields a London penetration depth λ = 1.6 ± 0.2 μm. The zero-field Kubo-Toyable relaxation rate Δ_{KT} equals 0.129 ± 0.004 μs^{-1} and does not show a significant change below T_c. This puts an upper bound of 0.04 mT on the spontaneous magnetic field associated to a possible odd-parity superconducting order parameter component.

These observations give a consistent picture with the resistivity measurements under pressure. Superconductivity is enhanced under pressure. The upper-critical field data under

pressure collapse onto a single universal curve, which differs from the standard curve expected for a weak-coupling, orbital-limited, spin-singlet superconductor. The sufficiently large mean free path, the absence of Pauli limiting, and the unusual temperature variation of B_{c2} all point to a dominant odd-parity component in the superconducting order parameter of noncentrosymmetric YPtBi in accordance with theoretical predictions.

References

[1] N.P. Butch, P. Syers, K. Kirshenbaum, A. P. Hope, and J. Paglione, Phys. Rev. B **84**, 220504 (R) (2011).

[2] P. C. Canfield, J.D. Thompson, W.P. Beyermann, A. Lacerda, M.F. Hundley, E. Peterson, Z. Fisk, and H.R. Ott, J. Appl. Phys. **70**, 5800 (1991).

[3] P. A. Frigeri, D.F. Agterberg, A. Koga, and M. Sigrist, Phys. Rev. Lett. **92**, 097001 (2004).

[4] E. Bauer, G. Hilscher, H. Michor, C. Paul, E. W. Scheidt, A. Gribanov, Y. Seropegin, H. Nöel, M. Sigrist, and P. Rogl, Phys. Rev. Lett. **92**, 027003 (2004).

[5] N. Kimura, K. Ito, K. Saitoh, Y. Umeda, H. Aoki, and T. Terashima, Phys. Rev. Lett. **95**, 247004 (2005).

[6] I. Sugitani, Y. Okuda, H. Shishido, T. Yamada, A. Thamhavel, E. Yamamoto, T. Matsuda, Y. Haga, T. Takeuchi, R. Settai, and Y. Onuki, J. Phys. Soc. Jpn. **75**, 043703 (2006).

[7] K. Togano, P. Badica, Y. Nakamori, S. Orimo, H. Takeya, and K. Hirata, Phys. Rev. Lett. **93**, 247004 (2004).

[8] E. Bauer, G. Rogl, X.-Q. Chen, R. T. Khan, H. Michor, G. Hilscher, E. Royanian, K. Kumagai, D. Z. Li, Y. Y. Li, R. Podloucky, and P. Rogl, Phys. Rev. B **82**, 064511 (2010).

[9] A. B. Karki, Y. M. Xiong, I. Vekhter, D. Browne, P. W. Adams, D. P. Young, K. R. Thomas, J. Y. Chan, H. Kim, and R. Prozorov, Phys. Rev. B **82**, 064512 (2010).

[10] E. Bauer and M. Sigrist (Eds.), *Non Centrosymmetric Superconductors*, Lecture Notes in Physics, vol. **847**, Springer, Berlin, 2012.

[11] S. Chadov, X.-L. Qi, J. Kübler, G.H. Fecher, C. Felser, and S.-C. Zhang, Nat. Mater. **9**, 541(2010).

[12] H. Lin, L.A. Wray, Y. Xia, S. Xu, S. Jia, R.J. Cava, A. Bansil, and M.Z. Hasan, Nat. Mater. **9**, 546 (2010).

[13] W. Feng, D. Xiao, Y. Zhang, and Y. Yao, Phys. Rev. B **82**, 235121 (2010).

[14] M.Z. Hasan and C.L. Kane, Rev. Mod. Phys. **82**, 3045(2010).

[15] X.-L. Qi and S.-C. Zhang, Rev. Mod. Phys. **83**, 1057 (2011).

[16] T.V. Bay, T. Naka,Y.K. Huang, and A.de Visser, Phys. Rev. B **86**, 064515 (2012).

[17] G. Goll, M. Marz, A. Hamann, T. Tomanic, K. Grube, T. Yoshino, and T. Takabatake, Physica B **403**, 1065 (2008).

[18] E. Mun, *Yb-based heavy fermion compounds and field tuned quantum criticality* (Ph.D. thesis). Iowa State University, 2010.

[19] F.F.Tafti, T. Fujii, A. Juneau-Fecteau, S.R. de Cotret, N. Doiron-Leyraud, A. Asamitsu, and L. Taillefer, Phys. Rev. B **87**, 184504 (2013).

[20] C. Liu, Y.Lee, E.D. Mun, M. Caudle, B.N. Harmon, S.L. Bud'ko, P.C. Canfield, and A. Kaminski, Phys. Rev. B **83**, 205133 (2010).

[21] Y.S. Hor, A.J. Williams, J.G. Checkelsky, P. Roushan, J. Seo, Q. Xu, H. W. Zandbergen, A. Yazdani, N.P. Ong, and R.J. Cava, Phys. Rev. Lett. **104**, 057001 (2010).

[22] T.V. Bay, T. Naka, Y.K. Huang, H. Luigjes, M.S. Golden, and A. de Visser, Phys. Rev. Lett. **108**, 057001 (2012).

[23] S. Sasaki, Z. Ren, A.A. Taskin, K. Segawa, L. Fu, and Y. Ando, Phys. Rev. Lett. **109**, 217004 (2012).

[24] Y. Pan, A. M. Nikitin, T. V. Bay, Y. K. Huang, C. Paulsen, B. H. Yan and A. de Visser, Europhys. Lett. **104**, 27001 (2013).

[25] P. C. Canfield, J. D. Thompson, W. P. Beyermann, A. Lacerda, M. F. Hundley, E. Peterson, Z. Fisk, and H. R. Ott, J. Appl. Phys. **70**, 5800 (1991).

[26] P. G. Pagliuso, C. Rettori, M. E. Torelli, G. B. Martins, Z. Fisk, J. L. Sarrao, M. F. Hundley, and S. B. Oseroff, Phys. Rev. B **60**, 4176 (1999).

[27] P.G. Pagliuso, R. Baumbach, P. Rosa, C. Adriano, J. Thompson, and Z. Fisk, Abstract, in: APS March Meeting, Baltimore, 2013.

[28] P. C. Canfield and Z. Fisk, Philos. Mag. B **65**, 1117 (1992).

[29] C. Paulsen, D.J. Hykel, K. Hasselbach, and D. Aoki, Phys. Rev. Lett. **109**, 237001 (2012).

[30] C.P. Bean, Rev. Mod. Phys. **36**, 31 (1964).

[31] R. Kubo and T. Toyabe, *Magnetic Resonance and Relaxation*, ed. R. Blinc (North-Holland, Amsterdam, 1967) 810.

[32] E.H. Brandt, Phys. Rev. B **37**, 2349 (1988).

[33] M. L. Cohen, in *Superconductivity*, edited by R. D. Parks, Vol. 1 (Marcel Dekker, New York, 1969), Chap. 12.

[34] R. Balian and N. R. Werthamer, Phys. Rev. **131**, 1553 (1963).

[35] T. P. Orlando, E. J. McNiff, Jr., S. Foner, and M. R. Beasley, Phys. Rev. B **19**, 4545 (1979).

[36] N. R.Werthamer, E. Helfand, and P. C. Hohenberg, Phys. Rev. **147**, 295 (1966).

[37] A. M. Clogston, Phys. Rev. Lett. **9**, 266 (1962).

[38] B. S. Chandrasekhar, Appl. Phys. Lett. **1**, 7 (1962).

[39] K. Maki, Phys. Rev. **148**, 362 (1966).

[40] K. Scharnberg and R. A. Klemm, Phys. Rev. B **22**, 5233 (1980).

Chapter 6 Angular variation of the magnetoresistance of the superconducting ferromagnet UCoGe

We present an extensive magnetoresistance study conducted on single-crystalline samples of the ferromagnetic superconductor UCoGe. The data show a pronounced structure at $B^* = 8.5$ T for a field applied parallel to the ordered moments, m_0. Angle dependent measurements reveal this field-induced phenomenon has a uniaxial anisotropy. Magnetoresistance measurements under pressure show that B^* increases with pressure at the significant rate of 3.2 T/GPa. We discuss B^* in terms of a field-induced polarization change of the U and Co moments. Upper critical field measurements corroborate the extraordinary S-shaped $B_{c2}(T)$-curve reported for a field along the b-axis of the orthorhombic unit cell of UCoGe.

(Most of this chapter has been published as T. V. Bay *et al.*, Phys. Rev. B **89**, 214512 (2014))

6.1 Introduction

The intermetallic compound UCoGe belongs to the select group of superconducting ferromagnets [1]. In this intriguing group of materials, superconductivity develops in the ferromagnetic state at a temperature T_s well below the Curie temperature, T_C, for ferromagnetic ordering [2,3]. Moreover, below T_s superconductivity and ferromagnetic order coexist on the microscopic scale. The superconducting ferromagnets discovered so far are UGe_2 (under pressure [4]), URhGe [5], UIr (under pressure [6]) and UCoGe [1]. The co-occurrence of ferromagnetism and superconductivity is at odds with the standard BCS (Bardeen-Cooper-Schrieffer) scenario for phonon-mediated spin-singlet superconductivity, since the ferromagnetic exchange field impedes spin-singlet Cooper pairing [7]. Instead, alternative models have been proposed that exploit the itinerant nature of the ferromagnetic order where critical spin fluctuations, connected to a magnetic instability, mediate an unconventional, spin-triplet type of pairing [8,9]. Indeed, these uranium intermetallics, in which the 5*f*-electrons are delocalized, are all close to a magnetic instability that can be induced by mechanical pressure, chemical doping or an applied magnetic field [10]. Unraveling the properties of superconducting ferromagnets might help to understand how spin fluctuations can stimulate superconductivity, which is a central theme for materials families as diverse as heavy-fermion, high-T_s cuprate and iron pnictide superconductors.

UCoGe crystallizes, just like URhGe, in the orthorhombic TiNiSi structure with space group P_{nma} [11]. The coexistence of superconductivity and ferromagnetism was first reported by Huy *et al.* [1,12]. High-quality single crystals with a residual resistance ratio, $RRR = R(300\text{K})/R(1\text{K})$, of 30 have a Curie temperature T_C = 2.8 K and show superconductivity with T_s = 0.5 K. UCoGe is a uniaxial ferromagnet. The spontaneous magnetic moment, m_0, points along the *c*-axis and attains the small value of 0.07 μ_B per U-atom in the limit $T \rightarrow 0$. Proof for the microscopic coexistence of superconductivity and ferromagnetic order is provided by μSR (muon spin relaxation and rotation) [13] and ^{59}Co-NQR (nuclear quadrupole resonance) [14] experiments. Evidence for spin-triplet Cooper pairing has been extracted from the magnitude of the upper critical field $B_{c2}^{\perp}$ (measured for the field directed perpendicular to m_0), which greatly exceeds the Pauli limit for spin-singlet superconductivity [12,15]. The important role of spin fluctuations in promoting superconductivity is established by the large anisotropy of the upper critical field, $B_{c2}^{\perp} \gg B_{c2}^{\parallel}$ [12,15]. For $B \parallel m_0$ the magnetic transition becomes a cross-over, spin fluctuations are rapidly quenched and, accordingly, superconductivity is suppressed, while for

$B \perp m_0$ spin fluctuations become more pronounced and superconductivity is enhanced. At the microscopic level, the close link between anisotropic critical magnetic fluctuations and superconductivity was recently put on a firm footing by ^{59}Co-NMR (nuclear magnetic resonance) [16,17] and inelastic neutron scattering [18].

Yet another salient property of UCoGe is the unusual S-shaped curvature of the upper critical field for a field direction along the *b*-axis, B_{c2}^{b}, which yields the large value of ~ 18 T when $T \rightarrow 0$ [15]. This field-reinforced superconductivity seems to be closely connected to a field-induced quantum critical point as a result of the progressive depression of the Curie temperature [3,15,19]. The peculiar response of the magnetic and superconducting phases to a magnetic field calls for a detailed investigation of the anisotropy in the magnetic, thermal and transport properties. Here we present an extensive angle dependent magnetotransport study on high-quality single crystals of UCoGe for fields directed in the *bc*- and *ac*-planes of the orthorhombic unit cell. We identify a pronounced maximum in the magnetoresistance when the component of the field along the *c*-axis reaches a value $B^* = 8.5$ T. Measurements of B^* as a function of pressure show a roughly linear increase of B^* at a rate $dB^*/dp = 3.2$ T/GPa. The uniaxial nature of B^* and its large variation with pressure provide strong indications for a close connection to an unusual polarizability of the U and Co moments. Transport measurements around the superconducting transition in fixed magnetic fields $B \parallel b$ reveal that also our samples exhibit the S-shaped B_{c2}-curve when properly oriented in the magnetic field.

6.2 Sample preparation

A polycrystalline batch with nominal composition $U_{1.01}$CoGe was first fabricated by arc melting the constituents (natural U 3N, Co 3N, and Ge 5N) in a water-cooled copper crucible under a high-purity argon atmosphere. Then, with the help of a modified Czochralski technique, a single crystalline rod was pulled from the melt in a tri-arc furnace under a high-purity argon atmosphere. The crystal was shown to be comprised of a single-phase, by means of electron micro-probe analysis. Single-crystallinity was checked by x-ray Laue backscattering. Bar-shaped samples with typical dimensions $5 \times 1 \times 1$ mm^3 were cut from the crystals by means of spark erosion. Magnetotransport measurements were carried out on two samples with the current, *I*, along the *b*-axis and *c*-axis, with *RRR*-values of 30 (sample #1) and 8 (sample #2), respectively. The former had already been used in the past for a previous study of the upper-critical field of UCoGe [12].

6.3 Magnetoresistance

In Fig. 6.1 we show the resistivity of UCoGe (sample #1) as a function of the magnetic field applied along the *c*-axis. At the lowest temperature T = 0.27 K (< T_s) the initial steep rise signals the suppression of superconductivity at B_{c2} = 0.2 T. Next, $\rho(B)$ steadily increases and passes through a pronounced maximum at B^* = 8.5 T. Increasing temperature shows that the maximum at B^* is a robust property and it can be identified in the data up to at least 10 K. Although B^* can be observed to exist up to T = 10 K, its field value varies only weakly with temperature, as can be seen in the right inset of Fig. 6.1. We remark that the overall resistivity rapidly increases with temperature and in the paramagnetic phase the initial low-field magnetoresistance is negative. In the left inset of figure 6.1, we show data taken at T = 0.065 K in strong magnetic fields up to 33 T. The maximum at B^* is very pronounced indeed. For fields exceeding 12 T (*i.e.* above B^*) the magnetoresistance starts a steady increase that leads to the large value of 40 $\mu\Omega$cm at the maximum field used of 33 T.

In order to investigate the magnetocrystalline anisotropy of B^*, we have measured the angle dependence of the magnetoresistance. The data taken in a dilution refrigerator at T = 0.15 K are shown for a field rotation in the *bc*-plane and in the *ac*-plane in the upper and lower panels of Fig. 6.2, respectively. The major experimental observation is the steady upward shift of the maximum in $\rho(B)$ when the field is rotated away from the *c*-axis. The value $B^*(\theta)$ is proportional to $B^*(0)/\cos\theta$, where θ is the angle at which the field is tilted away from the *c*-axis. This functional behavior is illustrated in the inset in Fig. 6.2 and holds for the *bc*- as well as for the *ac*-plane. For $\theta > 58°$ the maximum in $\rho(B)$ falls outside the magnetic field range probed in the dilution refrigerator. We remark that the value of the maximum magnetoresistance ρ^* at B^* is essentially independent of the field-angle. This tells us the angle dependent magnetoresistance data could be collapsed onto a single reduced curve ρ/ρ^* *versus* B/B^*. We conclude the maximum in $\rho(B)$ occurs when the component of the magnetic field along the *c*-axis reaches B^* = 8.5 T. This behavior confirms its uniaxial nature, and it has this uniaxial character in common with the ferromagnetic order in UCoGe. The suppression of superconductivity in the field-angle interval probed in Fig. 6.2 takes place at a low value of the upper-critical field B_{c2} for $B \parallel c$-axis [15].

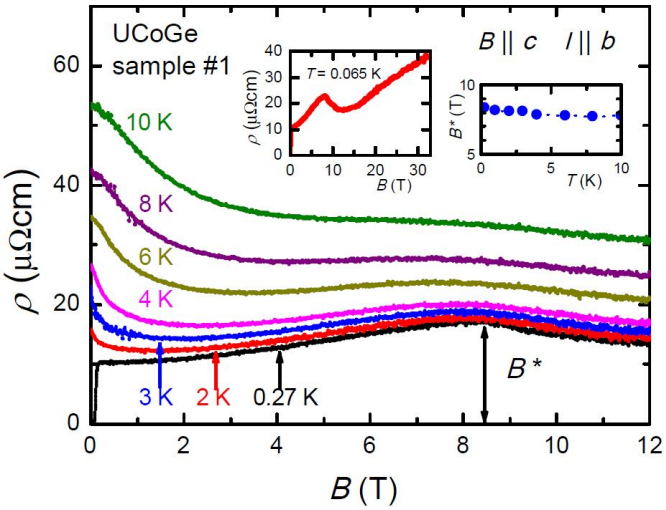

Figure 6.1 Resistivity of UCoGe (sample #1) as a function of the magnetic field $B \parallel c$ at temperatures of 0.27, 2, 3, 4, 6, 8 and 10 K, as indicated. The current was applied along the *b*-axis. Left inset: High-field magnetoresistance ($B \parallel c$; $I \parallel b$) up to B = 33 T at T = 0.065 K. Right inset: B^* as a function of temperature determined from the maximum in the magnetoresistance.

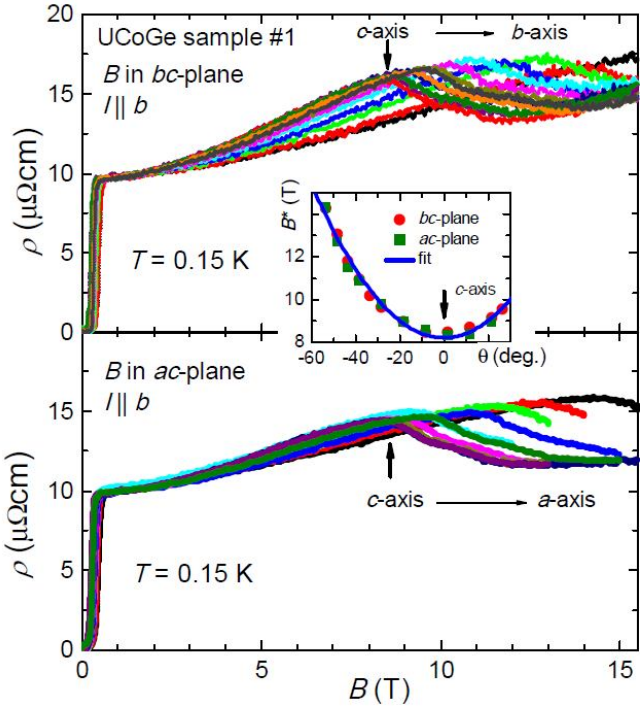

Figure 6.2 Angular variation of the magnetoresistance of UCoGe (sample #1) at T = 0.15 K. Upper panel: field rotation in the *bc*-plane; θ = -58, -53, -48, -43, -38, -33, -28, -18, -8, 2, 12, 22 and 27 degrees, where 0° corresponds to $B \parallel c$. Lower panel: field rotation in the *ac*-plane; θ = -53, -48, -43, -38, -28, -18, -8, 2, 12, 22 and 27 degrees. The current is always applied along the *b*-axis. Inset: B^* as a function of θ. The solid line represents $B^*(\theta) = B^*(0)/\cos\theta$.

The pressure variation of B^* was investigated for sample #2 for $B \parallel I \parallel c$ for pressures up to 1.29 GPa in the ^{3}He refrigerator. The lower residual resistance ratio (RRR = 8) for this sample results in a very different field variation $\rho(B)$, as shown in Fig. 6.3 for T = 0.25 K. Similar magnetoresistance data were recently reported in Ref. [20]. After the initial steep rise, due to the suppression of superconductivity, $\rho(B)$ steadily decreases and shows a kink rather than a maximum near 8.5 T. The field at which the kink appears identifies B^*. Under pressure B^* increases at an initial linear rate of 3.2 T/GPa (see inset to Fig. 6.3 for data at T = 0.25 K and 1.0 K). As the inset shows the temperature variation is weak. At our highest pressure, B^* falls outside the available magnetic field range in the ^{3}He refrigerator.

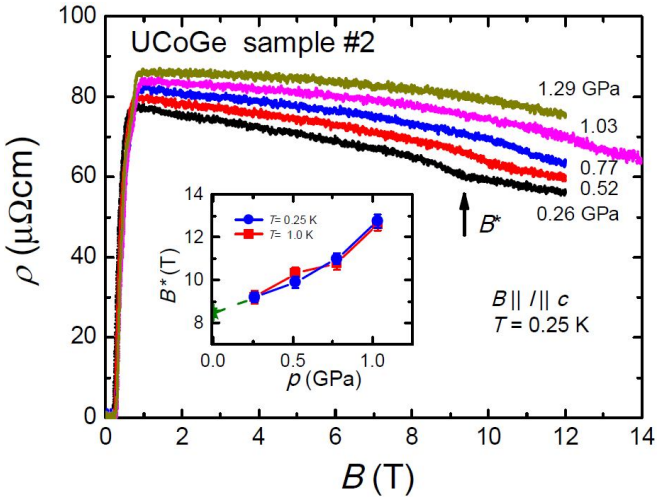

*Figure 6.*3 Magnetoresistance of UCoGe (sample #2) for $B \parallel I \parallel c$ at pressures of 0.26, 0.52, 0.77, 1.03 and 1.29 GPa as indicated. The temperature is T = 0.25 K. Inset: B^* as a function of pressure at T = 0.25 K (circles) and T = 1.0 K (squares). The value of B^* at ambient pressure (triangle) is taken from sample #1. The solid lines connect the data points. Data taken by A. Nikitin.

6.4 Upper critical field B_{c2}

The upper critical field $B_{c2}^{\perp}$ for a field direction ($B \parallel a$ or $B \parallel b$) perpendicular to the ordered moment ($m_0 \parallel c$) is extremely sensitive to the precise orientation of the magnetic field [15]. In order to substantiate this unusual B_{c2}^{b}-behavior of our single crystals we measured sample #1 as a function of field orientation in the dilution refrigerator. Special care was taken to enable field rotation in the *bc*-plane. After fine tuning to $B \parallel b$ we measured the resistivity in fixed magnetic fields. The results are shown in Fig. 6.4. For B = 0 the superconducting transition sets-in at 0.6 K and has a width ΔT_s = 0.1 K. On applying a magnetic field, the superconducting transition progressively shifts to lower temperatures, and is still visible up to the highest field (16 T). Striking features are (*i*) the change of the rate of the reduction of T_c in

the field range 5-9 T, and (*ii*) the narrowing of ΔT_s across the same field range. The upper critical field, determined by taking the midpoints of the transitions, is shown in Fig. 6.6. $B_{c2}^{b}(T)$ has an unusual curvature for $B > 4$ T and extrapolates to the large value of 17 T in the limit $T \to 0$, in good agreement with the results reported previously [15]. In the inset we show the strong angular variation of B_{c2} around $B \,||\, b$ measured at $T = 0.15$ K. For a tilt-angle of typically only 2° the upper critical field has already diminished by a factor of 3 [15]. For $B \,||\, a$, the upper critical field measurements displayed in Figs. 6.5 and 6.7 show there to be a remaining misorientation of the order ~ 2°, resulting in a rather small value of B_{c2}^{a} ($B_{c2}^{a} \sim 10$ T at $T = 0$), whereas in Ref. [15], $B_{c2}^{a} \sim 30$ T .

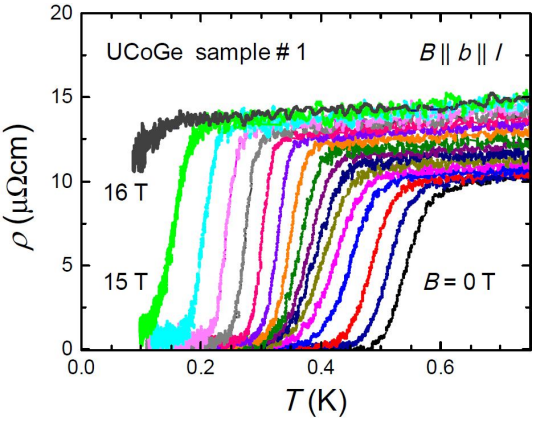

Figure 6.4 Superconducting transition of UCoGe (sample #1) measured by resistivity for $B \,||\, b \,||\, I$ in fixed magnetic fields from 0 to 16 T with steps of 1 T (from right to left).

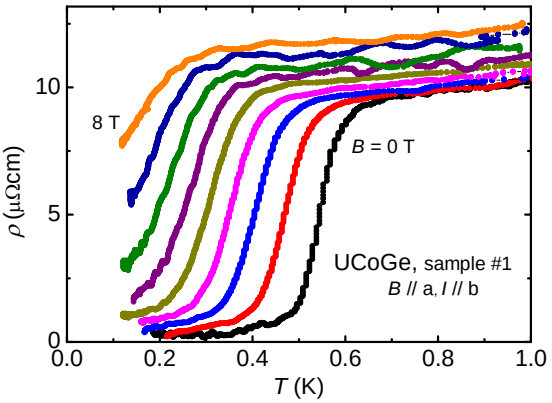

Figure 6.5 Superconducting transition of UCoGe (sample #1) measured by resistivity for $B \,||\, a$, $I \,||\, b$ in fixed magnetic fields from 0 to 8 T with steps of 1 T (from right to left).

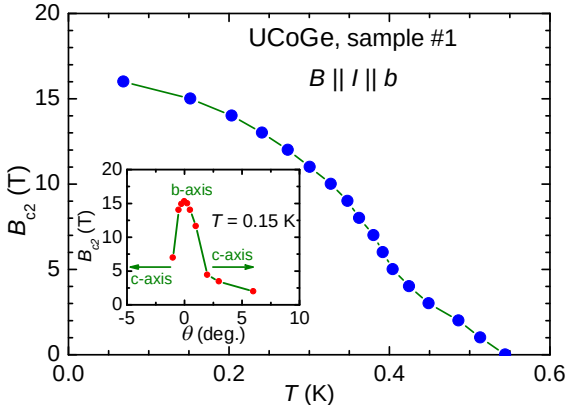

Figure 6.6 Temperature variation of the upper critical field $B_{c2}(T)$ of UCoGe (sample #1) measured for B // b. Inset: Angular variation of $B_{c2}(T)$ in the bc-plane at $T = 0.15$ K.

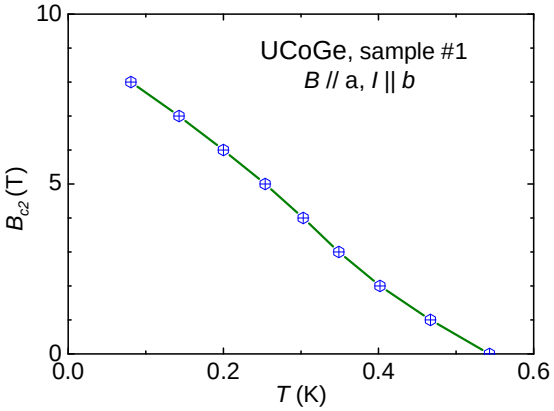

Figure 6.7 Temperature variation of the upper critical field $B_{c2}(T)$ of UCoGe (sample #1) measured for B // a.

6.5 Discussion

The major result from these angle dependent magnetoresistance measurements is the pronounced maximum at a field B^*, which occurs when the component of the magnetic field along the *c*-axis reaches a value of 8.5 T. This characteristic field B^* is a robust property of our samples, but the shape of the magnetoresistance $\Delta\rho \equiv \rho(B) - \rho(0)$ is different for sample #1 (with a maximum at B^*, Fig. 6.1) and sample #2 (with a kink at B^*, Fig. 6.3). We remark that there are two obvious differences between the experiments. Firstly, the sample quality is very different as quantified by the residual resistivity value ρ_0 of 10 and 75 $\mu\Omega$cm, respectively. Possibly, for sample #2 magnetic disorder makes a large contribution to ρ_0, which is then reduced by the magnetic field, resulting in a negative $\Delta\rho$. The second difference is the measurement geometry, *i.e.* transversal ($B \parallel c$, $I \parallel b$ for sample #1) *versus* longitudinal ($B \parallel c \parallel I$ for sample #2) magnetoresistance, since the Lorentz force on the current in general leads to more scattering and a positive $\Delta\rho$. Moreover, in the transverse configuration scattering is expected to be more effective since the current is perpendicular to m_0, compared to the longitudinal configuration where the current and m_0 are aligned. Measurements in the transverse geometry with $B \parallel c$ have not appeared in the literature so far, while longitudinal (*c*-axis) magnetoresistance data have been reported on two samples of different quality: (*i*) a magnetoresistance trace taken on a sample with $RRR = 30$ at $T = 0.04$ K shows a weak initially positive $\Delta\rho$ with a small structure near $B^* \approx 9$ T and three additional kink-like features in the field range 17-30 T [21], and (*ii*) the magnetoresistance of a sample with $RRR = 5$ has an overall negative $\Delta\rho$ with a kink at B_k or $B^* \approx 9$ T [20], as in our Fig. 6.3. In the latter study the angular variation of B^*, measured at $T = 0.04$ K by tilting the field from the *c*-axis towards an arbitrary direction in the *ab*-plane, was also found to follow the $B^*(\theta = 0)/\cos\theta$-law. The large variation of $\Delta\rho$ with the *RRR*-value and geometry is uncommon and its understanding is highly relevant in view of the strongly anisotropic magnetic properties of UCoGe.

An appealing scenario that has been put forward to explain the change in magnetoresistance at B^* is a ferro-to-ferrimagnetic transition [20]. This proposal is largely based on a recent polarized neutron diffraction experiment on UCoGe carried out for $B \parallel c$ [22]. In low magnetic field (3 T) the small ordered moment m_0 is predominantly located at the U atom, but in a large field of 12 T a substantial moment, antiparallel to the U moment, is induced on the Co site. This unusual polarizability of the Co 3*d* orbitals may give rise to a field-induced ferri-magnetic-like spin arrangement. Support for this scenario was obtained by

field-dependent ac-susceptibility data [20] which exhibit a maximum near B^*. However, hitherto we were unable to confirm this result in our AC-susceptibility measurement set-up. Recently, the DC-magnetization M(B) was measured at T = 1.5 K in pulsed magnetic fields up to 53 T [23]. The moment polarization is large. M(B) gradually increases from ~ 0.05 μ_B at B = 0 to 0.7 μ_B at the maximum field. For B ∥ c the data do not show a clear sign of a (meta)magnetic transition, however, a weak structure appears near B^* in the derivative dM/dB, and a second change of slope occurs near 23.5 T. Sensitive torque cantilever experiments might be helpful to resolve the possibly anomalous behavior of the magnetization around B^*. Further arguments in favor of a magnetic transition are: (*i*) the uniaxial (Ising-type) behavior of the ferromagnetic order is reflected in B^*, and (*ii*) the pressure variation of B^* (see Fig. 6.3) is large and has a magnitude comparable to the pressure dependence of T_C [24] assuming 1 K ≅ 1.5 T per μ_B (the critical pressure for the suppression of ferromagnetic order is 1.4 GPa). In this scenario the pressure increase of B^* may be related to the reduced polarizability of the Co moment under pressure.

Another possible origin of the structure in $\Delta\rho$ near B^* is a Lifshitz transition, *i.e.* a field-induced topological change of the Fermi surface. Notably it has been suggested that the multitude of small kink-like features observed in $\Delta\rho$ for B || c || I at T = 0.04 K could hint at a Fermi surface reconstruction [21]. Quantum oscillations have been reported for UCoGe for B ∥ b but could not be detected for a field direction along or close to the c-axis. A second indication for the possibility of a field-induced Fermi surface modification comes from thermoelectric power data [25], which show two pronounced peaks at 11.1 and 14.6 T for B || b. While the former peak is associated with field-reinforced superconductivity, the latter peak and the ensuing sign change of the thermopower provide evidence for a topological change of the Fermi surface. In the related material URhGe the field-induced disappearance of a small Fermi-surface pocket was recently demonstrated by quantum oscillations measurements [26].

Overall, the Ising-like nature of the ferromagnetic ground state results in a complex magnetotransport behavior. Moreover, the magnetization [12,23,27], thermal expansion [28], thermoelectric power [25] and thermal conductivity [29] all have a strong magnetocrystalline anisotropy, which makes it difficult to unravel the behavior of UCoGe. However, on the positive side, it is the strong anisotropy that results in longitudinal ferromagnetic fluctuations that are believed to play a major role in inducing spin-triplet superconductivity [17]. A greater understanding of the anisotropy is therefore likely to be important for our understanding of the superconductivity.

The unusual superconducting behavior is demonstrated by the $B_{c2}(T)$ curve reported in Fig. 6.6. We recall the upward curvature for $B > 4$ T and the large value of 17 T in the limit $T \rightarrow 0$. The sample (#1) used here comes from the same single-crystalline batch as used in our first measurements of the upper critical field [12], where $B_{c2}(0)$ was found to reach a value of 5 T for $B \parallel b$. This discrepancy can now be attributed to a small misorientation of 2° (see the inset in Fig. 6.6). Still, in the data reported in Ref. [15] the field-reinforced behavior and S-shaped B_{c2}(T) curve is more pronounced than in our data. Possibly, this is due to the somewhat larger ΔT_s of our sample and/or a remaining tiny misorientation towards the *ac*-plane [15]. The precise orientation of the sample with respect to the magnetic field direction remains absolutely crucial for pinning down the behaviour of this material. The field-reinforced superconductivity appears to be connected to critical spin fluctuations associated with a field-induced quantum critical point, where the latter is reached by the suppression of the Curie temperature in strong magnetic fields for $B \perp m_0$ [30]. A simple McMillan-type formula [19] can then be used to link T_s to the intensity of the critical spin fluctuations as probed by the effective mass, m^*, extracted from the coefficient A of the Fermi-liquid resistivity: $\Delta\rho(T) = \rho_0 + AT^2$. A second, more recently, proposed origin of the field-reinforced superconductivity is a Lifshitz transition [26,29]. Here a vanishing Fermi velocity $v_F = \hbar k_F / m^*$, where k_F is the Fermi wave vector, results in a small coherence length $\xi = \hbar v_F / \pi\Delta$, where Δ is the BCS excitation gap, which in turn leads to a high value of $B_{c2} = 2\pi\Phi_0/\xi^2$ (here Φ_0 is the flux quantum). Finally, we mention the progress made in modeling the intricate and anisotropic $B_{c2}(T)$ of UCoGe using a strong-coupling Eliashberg model, exploiting the Ising-type spin fluctuations [31]. There are also approaches being developed based on the completely broken symmetry scenario for parallel-spin *p*-wave superconductors [32].

6.6 Conclusion

In summary, we have presented an extensive angle dependent magnetoresistance study of single crystals of UCoGe for fields directed in the *bc*- and *ac*-planes of the orthorhombic unit cell. We pinpoint a pronounced structure in the magnetoresistance, which occurs when the component of the field along the *c*-axis reaches a value $B^* = 8.5$ T. This behaviour is very pronounced for transverse measurement geometry and rather weak for longitudinal geometry. Measurements of B^* as a function of pressure show a roughly linear increase at a rate $dB^*/dp = 3.2$ T/GPa. The uniaxial nature of B^* and its large pressure variation are consistent

with the interpretation that the change in the magnetoresistance regime at B^* is related to an unusual polarizability of the U and Co moments. Transport measurements in fixed magnetic fields confirm the extraordinary S-shaped $B_{c2}(T)$-behavior reported in the literature, after carefully aligning the sample along the field $B \parallel b$. In order to further unravel these intriguing properties of UCoGe, notably with respect to the close connection between field-induced phenomena, such as a quantum critical point or Lifshitz transition, and superconductivity, an unrelenting research effort is required to probe the strongly anisotropic thermal, magnetic and transport properties of this system with the help of high-quality single crystals.

References

[1] N. T. Huy, A. Gasparini, D. E. de Nijs, Y. Huang, J. C. P. Klaasse, T. Gortenmulder, A. de Visser, A. Hamann, T. Görlach, and H. v. Löhneysen, Phys. Rev. Lett. **99**, 067006 (2007).

[2] A. de Visser, in *Encyclopedia of Materials: Science and Technology (pp 1-6)*, edited by Eds. K. H. J. Buschow *et al*. (Elsevier, Oxford, 2010).

[3] D. Aoki, F. Hardy, A. Miyake, V. Taufour, T. D. Matsuda, and J. Flouquet, C. R. Phys. **12**, 573 (2011).

[4] S. S. Saxena, P. Agarwal, K. Ahilan, F. M. Grosche, R. K. W. Haselwimmer, M. J. Steiner, E. Pugh, I. R. Walker, S. R. Julian, P. Monthoux, G. G. Lonzarich, A. Huxley, I. Sheikin, D. Braithwaite, and J. Flouquet, Nature **406**, 587 (2000).

[5] D. Aoki, A. Huxley, E. Ressouche, D. Braithwaite, J. Flouquet, J. P. Brison, E. Lhotel, and C. Paulsen, Nature **413**, 613 (2001).

[6] T. Akazawa, H. Hidaka, T. Fujiwara, T. C. Kobayashi, E. Yamamoto, Y. Haga, R. Settai, and Y. Onuki, J. Phys. Condens. Matt. **16**, L29 (2004).

[7] N. F. Berk and J. R. Schrieffer, Phys. Rev. Lett. **17**, 433 (1966).

[8] D. Fay and J. Appel, Phys. Rev. B **22**, 3173 (1980).

[9] P. Monthoux, D. Pines, and G. G. Lonzarich, Nature **450**, 1177 (2007).

[10] C. Pfleiderer, Rev. Mod. Phys. **81**, 1551 (2009).

[11] F. Canepa, P. Manfrinetti, M. Pani, and A. Palenzona, J. Alloys Compd. **234**, 225 (1996).

[12] N. T. Huy, D. E. de Nijs, Y. Huang, and A. de Visser, Phys. Rev. Lett. **100**, 077002 (2008).

[13] A. de Visser, N. T. Huy, A. Gasparini, D. E. de Nijs, D. Andreica, C. Baines, and A. Amato, Phys. Rev. Lett. **102**, 167003 (2009).

[14] T. Ohta, T. Hattori, K. Ishida, Y. Nakai, E. Osaki, K. Deguchi, N. K. Sato, and I. Satoh, J. Phys. Soc. Jpn. **79**, 023707 (2010).

[15] D. Aoki, T. D. Matsuda, V. Taufour, E. Hassinger, G. Knebel, and J. Flouquet, J. Phys. Soc. Jpn. **78**, 113709 (2009).

[16] Y. Ihara, T. Hattori, K. Ishida, Y. Nakai, E. Osaki, K. Deguchi, N. K. Sato, and I. Satoh, Phys. Rev. Lett. **105**, 206403 (2010).

[17] T. Hattori, Y. Ihara, Y. Nakai, K. Ishida, Y. Tada, S. Fujimoto, N. Kawakami, E. Osaki, K. Deguchi, N. K. Sato, and I. Satoh, Phys. Rev. Lett. **108**, 066403 (2012).

[18] C. Stock, D. A. Sokolov, P. Bourges, P. H. Tobash, K. Gofryk, F. Ronning, E. D. Bauer, K. C. Rule, and A. D. Huxley, Phys. Rev. Lett. **107**, 187202 (2011).

[19] A. Miyake, D. Aoki, and J. Flouquet, J. Phys. Soc. Jpn. **77**, 094709 (2008).

[20] E. Steven, A. Kiswandhi, D. Krstovska, J. S. Brooks, M. Almeida, A. P. Gonçalves, M. S. Henriques, G. M. Luke, and T. J. Williams, Appl. Phys. Lett. **98**, 132507 (2011).

[21] D. Aoki, I. Sheikin, T. D. Matsuda, V. Taufour, G. Knebel, and J. Louquet, J. Phys. Soc. Jpn. **80**, 013705 (2011).

[22] K. Prokeš, A. de Visser, Y. K. Huang, B. Fåk, and E. Ressouche, Phys. Rev. B **81**, 180407(R) (2010).

[23] W. Knafo, T. D. Matsuda, D. Aoki, F. Hardy, G. W. Scheerer, G. Ballon, M. Nardone, A. Zitouni, C. Meingast, and J. Flouquet, Phys. Rev. B **86**, 184416 (2012).

[24] E. Slooten, T. Naka, A. Gasparini, Y. Huang, and A. de Visser, Phys. Rev. Lett. **103**, 097003 (2009).

[25] L. Malone, L. Howald, A. Pourret, D. Aoki, V. Taufour, G. Knebel, and J. Flouquet, Phys. Rev. B **85**, 024526 (2012).

[26] E. A. Yelland, J. M. Barraclough, W. Wang, K. V. Kamenev, and A. D. Huxley, Nat. Phys. **7**, 890 (2011).

[27] F. Hardy, D. Aoki, C. Meingast, P. Schweiss, P. Burger, H. v. Löhneysen, and J. Flouquet, Phys. Rev. B **83**, 195107 (2011).

[28] A. Gasparini, Y. K. Huang, J. Hartbaum, H. v. Löhneysen, and A. de Visser, Phys. Rev. B **82**, 052502 (2010).

[29] M. Taupin, L. Howald, D. Aoki, J. Flouquet, and J. P. Brison, Phys. Rev. B **89**, 041108 (2014).

[30] V. P. Mineev, Phys. Rev. B **83**, 064515 (2011).

[31] Y. Tada, N. Kawakami, and S. Fujimoto, J. Phys. Soc. Jpn. **80**, SA006 (2011).

[32] C. Lörscher, J. Zhang, Q. Gu, and R. A. Klemm, Phys. Rev. B **88**, 024504 (2013).

Summary

Superconductivity has played a prominent part in condensed matter physics for more than 100 years, but the understanding of this intriguing phenomenon still remains a theoretical challenge. Almost all current theoretical interpretations consider the key element making up the superconducting condensates to be the very formation of Cooper pairs derived from the microscopic Bardeen-Cooper-Schrieffer (BCS) theory in 1957. In this context, superconductors can be classified as conventional (BCS) or unconventional based on the symmetry of the Cooper pairs. Notably, the discovery of superconductivity in the ferromagnet UGe_2 in 2000 came as a big surprise because according to the BCS formalism, ferromagnetic order impedes the formation of Cooper pairs in spin-singlet states. Subsequently, only few other superconducting ferromagnets have been discovered: URhGe (2001), UIr (2004) and UCoGe (2007). To explain the coexistence of superconductivity and ferromagnetism on the microscopic scale, the most sophisticated theoretical treatment is to employ models of spin fluctuations near the quantum critical point. Here spin fluctuations mediate superconductivity, rather than phonons. However, what exactly the superconducting pairing mechanism is in the superconducting ferromagnets is still under debate.

Another highly interesting research field that has come to the fore in recent years is that of materials called topological superconductors, because these could host Majorana zero modes, which themselves offer a route to applications in topological quantum computation. Investigation and understanding of the intrinsic properties of topological superconductivity are therefore not only crucial for the realization of novel states of quantum matter but could also pave the way to potential device applications. This PhD work is an experimental study of unconventional superconductivity in the superconducting ferromagnet UCoGe and two candidate topological superconductors $Cu_xBi_2Se_3$ and YPtBi. The main techniques applied have been transport, magnetic and μSR measurements, and these have been carried out so as to shed further light on the intricate superconducting pairing mechanism in these novel materials.

In Chapter 2, a short description of the experimental techniques used throughout this dissertation is presented. The equipment for measuring at low temperatures and strong magnetic fields is introduced. We have also discussed the calibration of the RuO_2 thermometer in high magnetic field, as well as of the high-pressure cell. A brief discussion of the μSR technique employed at the Paul Scherrer Institute is also presented.

Chapter 3 is aimed at a concise theoretical overview of the related research themes presented throughout this project. We provide a general picture and link to the experimental work presented in later chapters. An overview of superconductivity, quantum criticality and quantum phase transitions is given in a close connection to the novel class of quantum matter: the superconducting ferromagnet. This is followed by a description of the intriguing properties of the latest member in the family, UCoGe. The chapter continues with a brief overview of the recent discovery and on the robust properties of topological insulators and topological superconductors. Next, we discuss superconductivity in a magnetic field. In particular, we consider the temperature variation of the upper critical field for both conventional BCS *s*-wave and unconventional superconductors. The analysis of the upper critical field is studied in much detail in Chapters 4 and 5 on $Cu_xBi_2Se_3$ and YPtBi, respectively.

By means of magnetic and transport measurements carried out on the candidate topological superconductor $Cu_xBi_2Se_3$, we have investigated in Chapter 4 the response of superconductivity in this system to a magnetic field and high pressures up to 2.3 GPa. Upon increasing the pressure, superconductivity is smoothly depressed and vanishes at $p_c \sim 6.3$ GPa. At the same time, the metallic behaviour is gradually lost. These features are explained by a simple model for a low electron carrier density superconductor. The analysis of the upper critical field shows that the $B_{c2}(T)$ data collapse onto a universal curve, which clearly differs from the standard curve of a weak coupling, orbital limited, spin-singlet superconductor. Although an anisotropic spin-singlet state cannot be ruled out completely, the absence of Pauli limiting and the similarity of $B_{c2}(T)$ to a polar-state function point to spin-triplet superconductor. Our observations are in line with theoretical proposals that $Cu_xBi_2Se_3$ is a promising candidate for the realization of a topological superconductor.

Transport, magnetic and μSR measurements on one of the few candidates for topological superconductivity in the Half Heusler family, YPtBi, are presented in Chapter 5. AC-susceptibility and DC-magnetization data provide unambiguous proof for bulk

superconductivity. An upper bound of the spontaneous field possibly associated with odd-parity superconductivity is obtained from the zero-field Kubo-Toyabe relaxation rate extracted from the μSR data. The temperature dependence of the upper critical field, $B_{c2}(T)$, deduced from electrical resistivity measurements at ambient pressure and pressure up to 2.3 GPa, signals a superconducting state at odds with the expectation of the standard BCS scenario. Most importantly, the $B_{c2}(T)$ data point to the presence of an odd-parity Cooper pairing component in the superconducting order parameter, in agreement with theoretical predictions for noncentrosymmetric and topological superconductors.

Finally, in Chapter 6, we present an extensive magnetoresistance study conducted on single-crystalline samples of the ferromagnetic superconductor UCoGe for a magnetic field directed in the *bc*- and *ac*-planes of the orthorhombic unit cell. We pinpoint a pronounced structure in the magnetoresistance, which takes place when the component of the magnetic field along the *c*-axis reaches a value $B^* = 8.5$ T. Angle dependent measurements reveal that this field-induced phenomenon has uniaxial anisotropy. Magnetoresistance measurements under pressure show a roughly linear and rapid increase of B^* with pressure, with a $\mathrm{d}B^*/\mathrm{d}p$ of 3.2 T/GPa. The uniaxial nature of B^* and its large pressure variation are consistent with the interpretation that the change in the magnetoresistance regime at B^* is related to an unusual polarizability of the U and Co moments. Upper critical field measurements corroborate the extraordinary S-shaped $B_{c2}(T)$-curve for a field along the *b*-axis of the orthorhombic unit cell. Although these and other studies have helped pin down the properties of UCoGe further, in order to finally unravel the intriguing properties of UCoGe, notably with respect to the close connection between field-induced phenomena such as a quantum critical point or Lifshitz transition and superconductivity, a continuous research effort is required to probe the strongly anisotropic thermal, magnetic and transport properties in this important superconductor.

Nederlandse samenvatting

Supergeleiding speelt al meer dan 100 jaar een vooraanstaande rol in gecondenseerde materie, maar nog steeds stelt dit intrigerende verschijnsel onderzoekers voor experimentele en theoretische uitdagingen. Bijna alle huidige theoretische interpretaties beschouwen Cooper paren, zoals afgeleid in demicroscopische theorie van Bardeen, Cooper en Schrieffer (BCS) in 1957, als het basisingredient van supergeleidende condensaten. In deze context kunnen supergeleiders als conventioneel (BCS) of onconventioneel geclassificeerd worden, gebaseerd op de symmetrie van de Cooperparen. Zeker opmerkelijk was dus in 2000 de ontdekking van supergeleiding in de UGe_2 omdat ferromagnetische orde (volgens het BCS formalisme) de vorming van Cooperparen in spin-singlet toestanden tegen werkt. Vervolgens zijn er nog enkele supergeleidende ferromagneten ontdekt: URhGe (2001), UIr (2004) en UCoGe (2007). Geavanceerde theoretische behandelingen die microscopisch het bestaan van supergeleidende ferromagneten proberen te verklaren, maken gebruik van modellen met spin fluctuaties dichtbij een quantum kritisch punt. Dit betekent dat het spin fluctuaties zijn in plaats van roostertrillingen, die supergeleiding mogelijk maken. Wat precies het mechanisme is achter de ferromagnetische supergeleiders is echter nog steeds een punt van discussie.

In de afgelopen jaren heeft een ander veld van onderzoek veel belangstelling gegenereerd, namelijk dat van topologische isolatoren en supergeleiders. Deze materialen kunnen, onder bepaalde omstandigheden, Majorana zero modes ondersteunen, die op hun beurt weer kandidaat zijn voor toepassing in topologische quantum berekeningen en computers. Onderzoek naar en het begrip van de intrinsieke eigenschappen van topologische supergeleiders zijn dus niet alleen cruciaal voor de realisatie van nieuwe toestanden van materie, maar kunnen ook leiden naar toepassing in nieuwe technologieën. Dit promotieonderzoek is een experimentele studie naar de onconventionele eigenschappen van de supergeleidende ferromagneet UCoGe en twee potentiële topologische supergeleiders: $Cu_xBi_2Se_3$ and YPtBi. De belangrijkste technieken gebruikte bij dit onderzoek zijn elektrische weerstand, magnetische metingen en μSR. De experimenten zijn er met name op

gericht om het gecompliceerde Cooper-paringsmechanisme in deze nieuwe supergeleiders te verhelderen.

In Hoofdstuk 2 worden de experimentele technieken beschreven die gebruikt zijn tijdens het onderzoek voor dit proefschrift. De apparatuur die gebruikt is voor de metingen bij lage temperatuur en in hoge magneetvelden wordt geïntroduceerd. Ook wordt de ijking van de RuO_2 thermometer in hoog magneetvled en de ijking van de hoge druk cel besproken. De SR techniek gebruikt bij het Paul Scherrer Institute wordt ook kort beschreven.

Hoofdstuk 3 geeft een beknopt overzicht van de theoretische thema's die van toepassing zijn op dit project. Een algemene achtergrond wordt geschetst, die in latere hoofdstukken aan het experimentele werk wordt gekoppeld. Een overzicht van supergeleiding, quantum criticaliteit en quantum faseovergangen wordt gegeven en gerelateerd aan een nieuwe klasse van quantum materie: de supergeleidende ferromagneet. Dit wordt vervolgd met een beschrijving van de intrigerende eigenschappen van het laatste ontdekte familielid: UCoGe. Het hoofdstuk wordt vervolgd met een kort overzicht van deze recent ontdekking en gaat in op de robuuste eigenschappen van topologische isolatoren en supergeleiders. Vervolgens wordt de onderdrukking van supergeleiding in magnetische velden besproken. Met name worden de variaties in temperatuur van het bovenste kritische veld voor conventionele BCS *s*-wave en onconventionele supergeleiders belicht. De analyse van het bovenste kritische veld wordt in detail beschreven in Hoofdstukken 4 en 5 voor $Cu_xBi_2Se_3$ en YPtBi, respectievelijk.

Door middel van transport en magnetische metingen aan de potentiële topologische supergeleider $Cu_xBi_2Se_3$, is (in Hoofdstuk 4) de response van supergeleiding in dit systeem op een magneetveld en hoge druk, tot 2.3 GPa, onderzocht. Een hogere druk leidt tot een geleidelijke onderdrukking van de supergeleiding, die verdwijnt bij $p_c \sim 6.3$ GPa. Tegelijkertijd verliest het materiaal geleidelijk zijn metallische gedrag. Deze observaties kunnen verklaard worden aan de hand van een simpel model dat supergeleiders met een lage elektrondichtheid beschrijft. De analyse van het bovenste kritische veld toont aan dat de $B_{c2}(T)$ data met een universele curve beschreven kunnen worden. Deze curve verschilt duidelijk van het standaard gedrag van een zwak gekoppelde, orbitaal gelimiteerde, spin-singlet supergeleider. Alhoewel een anisotrope spin-singlet toestand niet uitgesloten kan worden, duiden de afwezigheid van Pauli beperking en de gelijkenis van $B_{c2}(T)$ met een polaire-toestandsfunctie op spin-triplet supergeleiding. Deze observaties zijn in overeenkomst

met theoretische voorstellen die suggereren dat $Cu_xBi_2Se_3$ een veelbelovende kandidaat is voor de realisatie van een topologische supergeleider.

Transport, magnetische en μSR metingen aan YPtBi (één van de kandidaten voor topologische supergeleiding in de Half Heusler familie) worden gepresenteerd in Hoofdstuk 5. AC-susceptibiliteit en DC-magnetisatie data tonen aan dat er eenduidig sprake is van bulk supergeleiding. Een bovengrens voor het spontane inwendige veld, mogelijkerwijs geassocieerd met oneven-pariteit supergeleiding, is verkregen uit de nul-veld Kubo-Toyabe relaxatie snelheid bepaald uit de SR data. De afhankelijkheid van het bovenste kritische veld $B_{c2}(T)$ van de temperatuur, afgeleid van de elektrische weerstandsmetingen van kamerdruk tot en met 2.3 GPa, laat zien dat er sprake is van een supergeleidende toestand die afwijkt van het standaard BCS scenario. De $B_{c2}(T)$ data duiden op de aanwezigheid van een oneven-pariteit Cooperparingscomponent in de supergeleidende orde parameter, dit komt overeen met theoretische voorspellingen voor noncentrosymmetrische en topologische supergeleiders.

Al laatste wordt in Hoofdstuk 6 een uitgebreide studie van de magnetoweerstand aan eenkristallijne preparaten van de ferromagnetische supergeleider UCoGe gepresenteerd. Hierbij is het magneetveld in de *bc*- en *ac*-vlakken van de orthorhombische eenheidscel gericht. Er wordt een karakteristieke structuur in de magnetoweerstand waargenomen-wanneer de component van het magneetveld langs de *c*-as een waarde van $B^* = 8.5$ T bereikt. Hoekafhankelijke metingen tonen aan dat dit door het magneetveld geïnduceerde effect een uniaxiale anisotropie heeft. Magnetoweerstandsmetingen onder hydrostatische druk laten een ruwweg lineair en snel stijgend verband zien tussen B^* en de druk: $dB^*/dp = 3.2$ T/GPa. De uniaxiale aard van B^* en zijn grote variaties in druk zijn consistent met de interpretatie dat de verandering in magnetoweerstand gerelateerd is aan een ongebruikelijke polarizatie van de U en Co magnetische momenten. Metingen van het bovenste kritische veld bevestigen de bijzondere S-vorm van de $B_{c2}(T)$ curve voor een magneetveld langs de *b*-as. Alhoewel dit onderzoek, samen met vergelijkbare studies, helpt de eigenschappen van UCoGe nader te bepalen, is er, om uiteindelijk het fascinerende materiaal UCoGe in detail te begrijpen, met name wat betreft het nauwe verband tussen het veldgeïnduceerde verschijnselen zoals een quantum kritisch punt of Lifshitz transitie en supergeleiding, vervolg onderzoek nodig om de sterk anisotropische thermische, magnetische en transport eigenschappen in deze belangrijke supergeleider te doorgronden.

List of publications

1. **T. V. Bay**, A. M. Nikitin, T. Naka, A. McCollam, Y. K. Huang, and A. de Visser, *"Angular variation of the magnetoresistance of the superconducting ferromagnet UCoGe"*, ***Phys. Rev. B*** 89, 214512 (2014).

   (As a part of Chapter 6)

2. **T. V. Bay**, M. Jackson, C. Paulsen, C. Baines, A. Amato, T. Orvis, M.C. Aronson, Y.K. Huang, and A. de Visser, *"Low field magnetic response of the non - centrosymmetric superconductor YPtBi"*, ***Solid State Commun***. 183, 13 (2014).

   (As a part of Chapter 5)

3. **T. V. Bay**, T. Naka, Y.K. Huang, H. Luigjes, M.S. Golden and A. de Visser, *"Superconductivity in the doped topological insulator CuxBi2Se3 under high pressure"*, ***Phys. Rev. Lett.*** 108, 057001 (2012).

   (As a part of Chapter 5)

4. **T. V. Bay**, T. Naka, Y.K. Huang, and A. de Visser, *"Superconductivity in non-centrosymmetric YPtBi under pressure"*, ***Phys. Rev. B*** 86, 064515 (2012).

   (As a part of Chapter 4)

5. **Tran Van Bay**, Nguyen Khanh Thuy and Nguyen Toan Thang, *"On the Collective Excitations in Magnetic Systems with a Singlet Crystal-Field Ground State"*, ***Communications in Physics*** 19, 129 (2009).

6. Y. Pan, A.M. Nikitin, **T.V. Bay**, Y.K. Huang, C. Paulsen, B.H. Yan, and A. de Visser, *"Superconductivity and magnetic order in the non-centrosymmetric half-Heusler compound ErPdBi"*, ***Europhys. Lett.*** 104, 27001 (2013).

7. E. Frantzeskakis, N. de Jong, B. Zwartsenberg, Y. Huang, **T. V. Bay**, P. Pronk, E. van Heumen, D. Wu, Y. Pan, M. Radovic, N. C. Plumb, M. Shi, A. de Visser, and M. S. Golden, *"EUV electronic lithography of micrometric patterns in 2D topological surface states"*, submitted.

8. Y. Pan, D. Wu, J. R. Angevaare, H. Luigjes, E. Frantzeskakis, N. de Jong, E. van Heumen, **T. V. Bay**, B. Zwartsenberg, Y. K. Huang, M. Snelder, A. Brinkman, M. S.

Golden, and A. de Visser, "*Optimizing the topological insulator* $Bi_{2-x}Sb_xTe_{3-y}Se_y$*: a magnetotransport study*", submitted.

Acknowledgements

Without the support of many people, this dissertation could hardly have been written. I would like to express my immense gratitude to the people that have kindly and unconditionally supported for the completion of my thesis over the last four years.

First and foremost, I would like to express my deepest acknowledgements to my supervisor, Dr. Anne de Visser, for admitting me as a PhD student in the Electron Quantum Matter (QEM) group. Dear Anne, thank you very much for introducing me to the fascinating world of experimental low temperature physics, in particular, the research of strongly correlated electron systems. I am deeply grateful for your kind guidance, your patience in helping me to get familiar with experimental techniques and methods and in assisting me during this study. In this context, I have gained a lot of experiences from you the ways of doing science. I truly understand that you are patient and consistent in checking and correcting this thesis manuscript. Thank you very much for all, Anne. Likewise, I would like to thank my promotor Prof. Mark Golden. Thank you very much for your guidance, financial support, and your fruitful comments as well as feedback on both scientific and non-scientific issues. Thanks for offering me the opportunity to work with the fastidious 'lady' STM. This was possibly not a trivial task, but strengthened me a lot. I have also learned much from you about calmness, confidence and how to deal things in a scientific way. It is definitely great pleasure to be part of the group.

I am very grateful to Dr. Doan Minh Thuy and Dr. Nguyen Thi Minh Phuong of the Quy Nhon University for their kind support and encouragements. I would like to thank Cô Trúc for her great assistance and hospitality to Vietnamese students.

I am obliged to Dr. Yingkai Huang for supplying and characterizing samples, and for teaching me to operate the X-ray back-scattering Laue diffraction machine. I highly appreciate your unremitted effort in synthesizing high quality single-crystals for us. My sincere thanks are for Dr. Naka Takashi of the National Institute for Materials Science, Japan. It was certainly my great pleasure to work with you. I have learned a lot from you for being

patient, especially when we managed to mount the samples in the pressure cell, which required a huge amount of tiny work. To me, you are truly a Japanese amongst others I have ever met. Many thanks go to Dr. Erik van Heumen for instructing me at the first steps approaching the LT-STM, and analyzing the data. I really appreciated the crash course which was crucial for my further steps in manipulating the 'lady'. You are also an excellent opponent in the discussions. Especially, I would like to send my sincere gratefulness to Dr. Nguyen Thanh Huy for introducing me to Anne and for his kind support as a big 'brother'.

Apart from the work implemented at the Van der Waals-Zemaan Institute (WZI), measurements have been performed using facilities in other research groups. I would like to thanks Dr. Carley Paulsen and Dr. Michel Jackson at the Néel Institute for their intensive magnetic measurements presented in Chapter 5. Many thanks go to Dr. Alex Amato and Chris Baines at the Paul Scherrer Institute in Villigen; to Dr. Alix McCollam at the University of Nijmegen; to Prof. Meigan Aronson and Dr. Tom Orvis at the Stony Brook University for their kind help and collaboration. It was my great delight to work with you.

Furthermore, thanks to the consistent help form all staff members of the WZI, my work has been done much more smoothly. I would like to thank Hugo Schlatter, Huib Luigjes for their great support in sample characterization; Hans Agema and Johan Mozes for the help of resolving the complex noise issues of the LT-STM. Life is much more smooth if you are around; Hans Ellermeijer and many others from the mechanical and electronic workshops for their support; Luuk Lusink, Rita Vinig, Ineke Baas (good that you could finally make jokes when talking with me), Anne Marieke and Natalie Wells for their administration assistance; Dr. Jeroen Goedkoop for his encouragements and evaluable discussions in the group meetings.

Taking this opportunity, I also wish to express my deep thanks to all members of the thesis committee for their time and fruitful discussions as regard to the manuscript.

The majority of my PhD time has been spent together with all students in the Quantum Electron Matter (QEM) family. You guys all are so great. I enjoyed very much not only working with you, including helping each other, sharing difficulties and scientific opinions but also spending time together in various in- and out door activities such as BBQs, lunch club, fly boarding, paintball, soccer, beach volleyball, games,… Many thanks to Freek Massee (now postdoc at the Cornell University), who helped me unconditionally whenever I had trouble with the 'lady'. No matter how late we were, you always arranged to be available in either real life or skype conversations. It was also great to play soccer with you. Nick, in

short, thanks a lot for being a paranymph of my defense, for the kind help during the difficulties while working with the STM, for your Dutch translation and delicious dinners (Caution: Dutch students are often busy at weekends due to parties, but they could also arrange time for something really fun if informed months in advance). Artem and Yu Pan, thanks for being my labmates; I love working with you. Many thanks go to Artem (the other paranymph) for his unpredicted BBQ. It was definitely great to 'enjoy' the conferences with you. Emmanouil, thanks for your kind help in many aspects both academic and social life; I am always happy after the discussions with you. Bo, it is my pleasure to be your colleague; thanks for your delicious Chinese meals. I wish to thank many other people in the group: 'small' Erik, Jochem, Berend, Alonaska (always nice to see your smiles and your attempts to say '*anh khoẻ không?*' in Vietnamese accent in the early mornings), Dong Wu, Shyama (thanks for taking the intensive STM/S data), Shira, Vincent, Peter and Tapas. Many thanks to other people within the UvA: Ha (now at ITIMS, Hanoi), Tuan (Columbia University, New York), Thanh (the tea and miscellaneous chats with you after the hard-working days fully refilled my energy), Duc Nguyen, Chung (also many thanks for the help of making the cover page), Nguyen Duc (now at ASML), Triet, Truc Anh, Chinh, Ngoc A, Dung, Minh Duc, Canh, Ha Chan, Van Anh, Rens (also many thanks for checking the summary translation). My time in Amsterdam was much easier and more enjoyable with the presence of you all. I would keep in my heart these unforgettable moments with you and the lovely city Amsterdam.

Another group of people who have continuously supported me during my time here is the Vietnamese community. You all made me feel at home. Thanks to all members of the VNAmsterdam football club. We are not always the champions, but that is fine. I will remember all of our parties and trips. It is definitely a great community for those who live far from home. Many thanks to my colleagues at Quy Nhon University and others, *anh* Hào-*chị* Loan (thanks to *anh* Hào for picking me up at the airport and showing me around for the first days), *anh* Thuận-*chị* Tâm, Vinh, Thắng, Hiếu, Hiền, Ánh, Thương, Nhựt (Italy), Nghĩa, Trường, Vương, *chị* Huynh, Trang, Năm Trung, Trọng (Osaka), Diệu (Utah), Thiện, *anh* Trung-*chị* Ngân, *anh* Huân, *anh* Trác (Hue) and Trung (Paris). I enjoyed so much time with you all. You are always by my side no matter what happens. Thanks for being there for me.

Special thanks to my girlfriend MTT, who has appeared in my life a bit later than expected. Thanks for your boundless love, consistent care and support, and for bringing me laughs through all the obstacles present on my path despite of the huge distance. MTT, life sometimes does not go on our way, but we can always make it.

Deep in my heart, I would like to express my special thanks and to devote this dissertation to my beloved family: my parents, my sisters and brothers, my nieces and nephews, who may never understand the work that has been completed in this dissertation, but always show love, care, support and constant encouragements over the years.

Ba Má kính yêu!

Con xin gửi tặng từng dòng chữ trong quyển Luận án này đến Ba Má. Con xin cảm ơn Ba Má đã yêu thương vô điều kiện và động viên con suốt thời gian qua. Từ lúc sinh ra cho đến thời điểm này, gần nửa thời gian con không ở bên Ba Má và gia đình. Có thể Ba Má sẽ không hiểu được việc con làm trong quyển luận án này, nhưng chỉ có một điều con muốn kính gửi đến Ba Má là tất cả những gì con làm là vì Ba Má và vì gia đình mình. Con kính chúc Ba Má luôn luôn khoẻ mạnh để luôn luôn dõi theo bước chân con trên quãng đời này.

I would like to thank all of my friends who I might have forgotten to mention in this dissertation.

Words are never enough to express my acknowledgements to those who have helped and supported me over the years. All these things I have done, just for you.

Amsterdam, September 2014

Tran Van Bay